NASA Technical Memorandum 100135

Liquid Sprays and Flow Studies in the Direct-Injection Diesel Engine Under Motored Conditions

Hung Lee Nguyen
Lewis Research Center
Cleveland, Ohio

Mark H. Carpenter
Langley Research Center
Hampton, Virginia

Juan I. Ramos
Carnegie-Mellon University
Pittsburgh, Pennsylvania

Harold J. Schock and James D. Stegeman
Lewis Research Center
Cleveland, Ohio

March 1988

(NASA-TM-100135) LIQUID SPRAYS AND FLOW N88-18594
STUDIES IN THE DIRECT-INJECTION DIESEL
ENGINE UNDER MOTORED CONDITIONS (NASA)
80 p CSCL 21E Unclas
G3/07 0128904

LIQUID SPRAYS AND FLOW STUDIES IN THE DIRECT-INJECTION DIESEL ENGINE UNDER MOTORED CONDITIONS

Hung Lee Nguyen
National Aeronautics and Space Administration
Lewis Research Center
Cleveland, Ohio 44135

Mark H. Carpenter
National Aeronautics and Space Administration
Langley Research Center
Hampton, Virginia 23665-5225

Juan I. Ramos
Carnegie-Mellon University
Pittsburgh, Pennsylvania 15213

Harold J. Schock and James D. Stegeman
National Aeronautics and Space Administration
Cleveland, Ohio 44135

SUMMARY

A two-dimensional, implicit finite-difference method of the control-volume variety, a two-equation model of turbulence, and a discrete droplet model have been used to study the flow field, turbulence levels, ~~fuel penetration~~, vaporization, and mixing in diesel engine environments. Good agreement with the droplet penetration data of Hiroyasu and Kadota was obtained for a range of ambient pressures by neglecting the effects of void fraction, droplet coalescence, and droplet collisions in the simulation. The model has also been used to study the effects of engine speed, injection angle, spray cone angle, droplet distribution, and intake swirl angle on the flow field, spray penetration and vaporization, and turbulence in motored two-stroke diesel engines. It is shown that spray penetration and vaporization increase with the intake swirl and produce large gas-phase velocities and turbulence levels. The spray penetration also increases with the diameter of the droplets injected into the cylinder. Large droplets may traverse the cylinder and strike on the piston or the cylinder wall, where they vaporize. Small droplets are trapped in the injection-generated eddies, where they vaporize. Small cone angles result in little radial spray penetration and droplets vaporized in the injection-generated eddies. As the spray cone angle is increased, the spray penetration and vaporization increase up to some limit. Beyond a critical spray cone angle, some droplets vaporize near the cylinder centerline in the injection-generated eddies, and others vaporize slowly along the cold cylinder wall. Early injection results in larger spray penetrations because of the low cylinder temperatures and relatively small vaporization cooling. Late injection results in fast vaporization near the injector, where the droplets are trapped by the injection-generated eddies. As the engine speed increases, the turbulence kinetic energy and gas-phase velocities increase. This results in large deceleration of the injected droplets and fuel vaporization near the injector and cylinder centerline. It is shown that there are optimum conditions for injection, which depend on droplet distribution, swirl, spray cone angle, and injection angle. The optimum conditions result in good spray penetration and vaporization and in good fuel mixing. The

E-3685

calculation presented in this report clearly indicates that internal combustion engine models can be used to assess, at least qualitatively, the effects of injection characteristics and engine operating conditions on the flow field and on the spray penetration and vaporization in diesel engines.

INTRODUCTION

The objective of this report is twofold. First, a two-dimensional, implicit finite-difference method of the control-volume variety, a two-equation model of turbulence, and a discrete droplet model have been developed to study the flow field and spray penetration in stagnant ambients at different pressures. The model predictions have been compared with the experimental data of Hiroyasu and Kadota (ref. 1), and good agreement was obtained by neglecting volumetric displacement effects on the gas phase (ref. 2), droplet collisions and coalescence (refs. 3 to 10), and droplet breakup (ref. 11). Second, the effects of intake swirl angle, engine speed, and injection characteristics on the flow field in a turbocharged, two-stroke diesel engine operating under motored conditions have been analyzed. Multidimensional models of two-stroke diesel engines have been developed by several investigators (refs. 12 to 20). Awn and Spalding (ref. 12) determined the flow field during the intake and exhaust strokes and assessed the scavenging efficiency in a two-stroke diesel engine. However, they did not study the influence of swirl and fuel injection on the flow field. Sher (refs. 13 to 15) modeled and performed experiments in a loop-scavenged engine and compared the boundary between the fresh charge and the residual gases with experimental data obtained in a transparent model engine.

Adachi et al. (ref. 16) calculated the scavenging efficiency as a function of the delivery ratio and compared their predictions with experimental data. They assumed that the details of the exhaust valve do not affect the scavenging processes. Diwakar (ref. 17) also modeled gas exchange processes in a uniflow-scavenged, two-stroke diesel engine and simulated the exhaust valves as a single annular slot on the cylinder head. He showed that the location of the exhaust annulus did not affect the conclusions reached in his work and that during the gas exchange process, the flow field is characterized by two recirculation zones: one near the cylinder head and the other near the cylinder wall. Carpenter and Ramos (refs. 18 and 19) have studied the effects of swirl on the flow field in a uniflow-scavenged, two-stroke diesel engine under motored conditions. They showed that during the gas exchange process, two recirculation zones are created: one near the cylinder wall and the other near the cylinder centerline. The flow fields obtained by Carpenter and Ramos (refs. 18 and 19) are in qualitative agreement with those obtained by Diwakar (ref. 17) and Uzkan and Hazelton (ref. 20). These investigators showed that the size of the recirculation zone located near the cylinder centerline increases as the swirl angle is increased. The size of this recirculation zone decreases in the compression stroke. Uzkan and Hazelton (ref. 20) also studied the effects of swirl level on the mixing of the fresh charge with the residual gases and showed that to enhance the mixing of the fuel spray with the fresh air, a medium swirl level is better than high or low swirl levels. Kuo and Yu (ref. 21) investigated the effect of nozzle hole number and nozzle hole size and injection duration of a transient spray. They demonstrated that the mixing rate increases with the injection velocity.

None of the aforementioned investigators analyzed the effects of swirl, engine speed, injection angle, droplet distribution function, and spray cone angle on the spray penetration, vaporization, and mixing in uniflow-scavenged, two-stroke diesel engines. These effects are discussed in this report, with detailed analyses in appendixes A to E.

PROBLEM FORMULATION

The mean flow field in the axisymmetric configurations studied in this report is governed by mixed hyperbolic-parabolic conservation equations for mass, momentum, and energy. These equations can be derived from the instantaneous, three-dimensional Navier-Stokes equations by taking a long-time average, by assuming no density fluctuations, by neglecting the pressure-velocity and triple correlations, by using a Boussinesq model for the double correlations, and by assuming that the mean flow is axisymmetric. These assumptions result in long-time-averaged conservation equations of mass; axial, radial, and azimuthal velocity components; and energy and species mass fraction equations; and contain source/sink terms which account for the exchanges of mass, momentum, and energy between the gas and liquid phases.

A two-equation model of turbulence which includes the effects of compressibility in the equations for the turbulence kinetic energy and its dissipation rate has been used. The model does not consider the effects of the liquid phase on turbulence; for example, it does not consider the effects of several droplets in a turbulent eddy. The turbulence model consists of two transport equations for the turbulence kinetic energy and its rate of dissipation and yields a characteristic turbulent length and a characteristic turbulent time scale.

A discrete droplet model has been used to calculate the droplet positions, velocities, and temperatures in the following manner. The mass of fuel injected in a time interval has been assigned to a Rosin-Rammler droplet distribution function. This distribution was discretized by assigning to certain typical droplet diameters a characteristic number of droplets, the initial velocities and initial injection locations of which are randomly perturbed about a mean position and vector. The droplet injection velocities were specified from experimentally determined values. The initial radial and axial droplet locations were not specified at the cylinder head. These locations were chosen several nozzle diameters downstream from the injector, since the liquid jet breakup and the ligament regions were not simulated. The initial droplet locations were chosen randomly in order to account for the unsteady characteristics of the liquid fuel jet breakup.

The liquid fuel was injected as a conical sheet with some broadening to account for the liquid droplet dispersion. Forced convection correlations were used to calculate the mass and heat exchanges between the gas phase and the liquid droplets, and the Clausius-Clapeyron equation was used to determine the liquid fuel vaporization rate.

Volumetric displacement effects on the gas-phase equations were neglected (ref. 2); that is, a thin spray approximation was used, and droplet collisions and coalescence were neglected (ref. 3). Comparisons with experimental data (ref. 11) have shown that good agreement can be obtained if the experimental injection velocities are used in the calculations. Thin spray models have been used by Gosman and Johns (ref. 22) and Gosman and Harvey (ref. 23). Dukowicz (ref. 2) accounted for volumetric displacement effects but did not consider droplet collisions, coalescence, and breakup, and obtained good agreement with the experimental data of Hiroyasu and Kadota (ref. 1) for a variety of ambient conditions. This agreement seems to have been obtained by employing very small droplets (private communication from P.J. O'Rourke, Los Alamos Laboratory, New Mexico). O'Rourke and Bracco (ref. 3) developed a probability density function formulation for thick sprays that accounts for kinetic energy of the droplets, volumetric displacement effects, and droplet collisions and coalescence. O'Rourke and Bracco (ref. 3) obtained very good agreement with the experimental data of Hiroyasu and Kadota (ref. 1). Kuo and Bracco (ref. 6) used a thick spray approximation and also obtained good agreement with experimental data.

The interaction between the gas-phase turbulence and the droplets was modeled by adding to the mean droplet velocity a fluctuating velocity which was assumed to be isotropic; this velocity was determined from the gas-phase turbulence kinetic energy and was assumed to act on the droplets in a continuous manner for the duration of the computational time step. This approach can be justified because of the small time steps used in the calculations; time steps are on the order of the droplet residence times in a typical eddy and on the order of a characteristic eddy turnover time. Calculations have been performed to show that for sufficiently small time steps, the effects of turbulence on the droplets are of secondary importance. The effects of the droplets on eddy were neglected.

The droplet packets were tracked in Lagrangian coordinates, and ordinary differential equations were solved to determine the droplet positions, velocities, radii, and temperatures. An implicit, second-order-accurate scheme was used to solve the Lagrangian equations.

The gas-phase equations were solved in Eulerian coordinates on a grid which expands and contracts with the piston motion. A transformation of coordinates was used to transform the moving-boundary value problem associated with the piston motion into a fixed-boundary value problem (ref. 24). A staggered grid was used to calculate the finite-difference form of the advection terms, depending on the cell Reynolds number. This treatment resulted in a conservative finite-difference scheme of the control-volume variety. The gas-phase velocity components, temperature, and species concentrations were calculated from the momentum, energy, and species equations.

A global perturbation technique (ref. 25) was introduced to calculate the global pressure variations associated with the piston compression and expansion strokes, and the droplet evaporation. This technique assures global mass conservation and accounts for the mixture thermodynamics in a global manner. The global pressure perturbation can be obtained from the finite-difference form of the continuity equation (refs. 25 and 26).

The two-way coupling between the liquid and gas phases was used to account for the mass, momentum, and energy exchanges between the two phases. The locations of the droplet packets with respect to each of the three Eulerian grids (u- and v-momentum components and scalars) were determined at each time step. The source terms in the gas-phase equations were determined by allocating the cumulative changes experienced by all the packets into the cells where the changes occurred. For packets traversing more than one cell during a time step, the exchanges were divided into the appropriate cells in proportion to the percentage of the time spent in each cell. Stiffness and numerical convergence problems were avoided with this technique, since the droplet history was used to allocate the changes among the appropriate cells, rather than concentrating them into the cell where the packets reside at the end of each time step. Linear interpolation based on the distances between the droplet and the cell nodal points was used to calculate the gas-phase properties at the droplet locations.

PRESENTATION AND DISCUSSION OF RESULTS

Comparison With Experimental Data of Hiroyasu and Kadota

The thin spray model described in the preceding section has been used to study fuel penetration in diesel engine environments and has been compared with the experimental data of Hiroyasu and Kadota (ref. 1) for different ambient conditions.

In Hiroyasu and Kadota's experiments, the temperature is uniform, and fuel vaporization is negligible. The initial velocity of the spray was determined by extrapolating the experimentally determined spray penetration rate at time $t = 0$. Also, the experimentally determined spray angle was used in the calculations.

The number of packets injected per time step was determined in parametric studies by analyzing the dependence of the solution on increasing number of droplet packets. It was found that little change was observed in the converged solution for a fivefold increase in the number of packets spanning the size of the droplet distribution. A minimum number that still resolved the droplet distribution was chosen for the computation. The parameters of the Rosin-Rammler distribution were determined by calculating approximate Weber number criteria for the injected droplets. A Weber number of 20 gives an approximate upper bound for stable droplets (ref. 2). In evaluating the Weber number, the velocity of the liquid surface relative to the gas should be used. However, in the vicinity of the nozzle, such a velocity is some fraction of the injection velocity because of the boundary layer of the liquid on the wall of the nozzle, and its exact value is not known (ref. 27). The relative velocity between the gas and liquid phases has a small effect on the initial spray droplet size because, for a given Weber number and liquid, the initial droplet size is inversely proportional to the square of the relative velocity (ref. 27). Parametric studies were performed to assess the influence of the relative velocity between the gas and liquid phases on the spray penetration. Small relative velocities yielded big droplets and overpredicted the spray penetration. Small relative velocities yielded big droplets and overpredicted the spray penetration (ref. 26).

Bracco (ref. 27) and Kuo and Bracco (ref. 6) estimated the initial Sauter mean diameter from the theory developed by Taylor (refs. 28 and 29), who studied the rate of growth of the perturbations of planar liquid surfaces induced by coflowing gases. This theory predicts that the initial droplet diameter is directly proportional to the liquid surface tension and the wavelength of the fastest growing surface wave, and inversely proportional to the gas density and the square of the relative velocity between the gas and the liquid phases. In view of the limitations of Taylor's theory (ref. 27), much more research needs to be done to accurately determine the initial droplet size for multidimensional models. The calculations performed by Carpenter (ref. 26) indicate that as long as "reasonable" droplet sizes are chosen, the spray penetration is mainly controlled by the exchanges of mass, momentum, and energy between the gas and liquid phases. This is not to say that the droplet size is of secondary nature; in fact, the initial droplet size and the relative velocity have a strong effect on the spray penetration. Calculations for the four ambient pressures investigated by Hiroyasu and Kadota (ref. 1) showed that stable droplets are of the order of 10 to 20 μm, depending on the relative velocity between the two phases. For injection velocities larger than 100 m/sec, droplets larger than 20 μm in diameter will break up into smaller droplets.

The fuel flow rate was calculated by using a discharge coefficient of 0.7 and by assuming that the nozzle pressure is equal to the needle opening pressure of 9.9 MPa. Needle opening was assumed to be instantaneous.

The time step used in the calculations was optimized to account for the implicit nature of the numerical scheme and for the penetration of the droplets. It was also determined so that the spray penetration was time-step independent. If the time step is very large, the droplets may cross several computational cells, and oscillations develop near the injector because of errors related to the gas-phase properties used in the evaluation of the source terms.

The time step was selected so that the droplets do not cross more than four cells per time step. This criterion was found to result in nonoscillatory solutions.

Several grids were employed in the calculations. It was ultimately decided that a 32 by 32 grid resulted in accurate and almost grid-independent results; in the radial direction, the solutions showed radial grid independence between 27 and 32 points. However, in the axial direction, changes in the second and third decimal places were found with 27 and 32 axial points. Since the axial direction required a high grid density, a relatively short axial domain of 10 cm was used in the calculations. Neumann's conditions were used as boundary conditions.

Figure 1 shows the spray penetration as a function of time for ambient pressures of 1, 11, 30, and 50 atm. In this figure, the solid lines denote computational results, whereas the dotted lines correspond to the experimental data of Hiroyasu and Kadota (ref. 1). Figure 1 clearly indicates that the thin spray approximation yields good agreement with experimental data.

Our model yields good agreement with Dukowicz's results (ref. 2), which account for volumetric displacement effects; these effects are important near the injector. However, it should be pointed out that Dukowicz had to use very small droplets near the injector (private communication from P.J. O'Rourke).

The comparisons presented in figure 1 are in remarkable agreement with those of O'Rourke and Bracco (ref. 3), who accounted for volumetric displacement effects and droplet coalescence and collisions. The "bumps" observed in the penetrations shown in figure 1 are due to turbulent fluctuations on the droplets.

Figure 1 also shows the spray penetration (note the change in scale) for an ambient pressure of 50 atm computed with three time steps. This figure indicates that the spray penetration is time-step independent for $\Delta t \leq 100$ msec. A time step of 150 msec yields farther penetration than a time step of 50 msec. (A time step of 50 msec was used in the calculations presented in this report.)

The results presented in figure 1 indicate that although the interaction between the droplets and turbulence is a function of the droplet residence time in an eddy and of the eddy lifetime, turbulence has a secondary effect if sufficiently small time steps are employed in the calculations. This justifies the addition of a new fluctuating velocity to the droplet mean velocity every time step, even though both the droplet residence time in an eddy and the eddy lifetime are functions of space and time. However, if the time step is not sufficiently small, the results shown in figure 1 indicate that large errors may result if a new fluctuating velocity is added to the droplet mean velocity every time step.

Numerical calculations showed that the penetration rate is a function of the imposed velocity at the injector and a weak function of the discharge coefficient. By imposing the gas-phase velocity and the droplet velocity at the injector as the experimentally extrapolated velocities, very good agreement was found. However, if no velocity is imposed in the gas phase at the injector, overpenetration is observed.

It was also found that once the proper velocity is imposed at the injector, the penetration rate is only a weak function of the assumed droplet distribution. This is expected for droplet distributions composed predominantly of 10-μm droplets, since they easily exchange their momentum with the gas phase. Larger penetrations were observed when using larger droplets because they exchange their momentum less effectively with the gas phase.

Figure 1 shows that the computed penetration rates decrease faster than the experimental ones near the latter parts of the penetration rate curves. This could be explained by absence of collisions in the present model. If collisions occurred, larger droplets would gradually form, and increased penetration rates would result. However, in the initial stages of penetration the most important parameters are (1) the spread rate in the ligament regime and the imposed velocity in the gas phase, and (2) the total momentum a injected into the computational domain. Only later do other effects become significant.

In figure 2 the gas-phase velocity and droplet locations are shown for an ambient pressure of 50 atm. Figure 2 clearly indicates that gas is drawn down along the wall and into the spray. At the head of the spray, a rollup vortex can be seen.

Figure 2 shows that the radial (r) direction is sufficiently large for the no-gradient boundary conditions at $r = 3$ cm to be accurate. The calculations were interrupted before the axial boundary condition at $x = 10$ cm became invalid. Larger droplets penetrate farther than small droplets, and gradually the spray head is enriched with large droplets. The tip droplet (i.e., the one with the farthest axial penetration) is always slightly behind the tip of the gas-phase head vortex. This is consistent with the assumption of incompressibility and with the fact that information in the gas phase travels at an infinite speed and makes the gas aware of the droplets' presence before their actual arrival.

Two-Stroke Diesel Engine Modeling

The engine geometry used in the calculations reported here resembles a standard side-ported, two-stroke engine provided with a flat piston, an inlet port, and an exhaust valve. The inlet port consists of a circumferential orifice located a the cylinder wall; this orifice is covered and uncovered by the piston. The exhaust valve is simulated as an infinitesimally thin disk which penetrates into the engine cylinder in the expansion stroke. The valve stem is infinitesimally thin and coincides with the cylinder axis (ref. 30). The intake port is connected to a turbocharger, which provides airflow at 1.35 atm. The intake flow has three velocity components: axial, azimuthal, and radial. An effective compression ratio of 15 to 1 at 1000 rpm was assumed. The geometrical characteristics of the two-stroke diesel engine considered in this study are presented in table I.

Table II summarizes the cases presented in this report. Swirl was induced during the flowthrough period at the intake port. The angle between the azimuthal and radial velocity components at the intake port was varied from 0° to 45°. A constant mass flow rate at the inlet port was used.

The effects of engine speed (1000, 1500, and 2000 rpm) were studied for a spray cone angle of 156° with and without swirl, and for a Rosin-Rammler droplet distribution function with a maximum number density at a droplet diameter of 30.8 μm and a maximum droplet diameter of 50 μm. Fuel was injected from 15° before top-dead-center (BTDC) to 5° after top-dead-center (ATDC).

The effects of spray cone angle (156°, 120°, 60°, and 20°) were studied at 1000 rpm with and without swirl for the same droplet distribution function and injection interval as described in the preceding paragraph.

The effects of injection angle (15°, 30°, and 45° BTDC to 5° ATDC) were studied for Rosin-Rammler droplet distribution functions corresponding to $d_{peak} = 30.8$ μm and $d_{max} = 50$ μm, and $d_{peak} = 60$ μm and $d_{max} = 100$ μm, where d_{max} and d_{peak} correspond to the maximum droplet diameter and to the location of the peak of the Rosin-Rammler distribution function, respectively.

For a spray cone angle of 156°, the no-slip condition between the gas and liquid phases was imposed at the injector; the droplets were injected at 293 K, at a pressure equal to that of the cylinder, and at random axial and radial locations near the cylinder head and the cylinder centerline to simulate the unsteady breakup of the liquid jet and ligaments into droplets. A Rosin-Rammler droplet distribution function was used, and droplets were injected so that stoichiometry of 0.689 was obtained. The droplet distribution function was spanned by 10 droplet packets. Fifteen packets were injected per time step for a distribution with $d_{max} = 100$ μm; 10 droplet packets per time step were injected for a distribution with $d_{max} = 50$ μm. The computations were performed with a time step corresponding to 0.5 crankshaft angle degrees at 1000 rpm, and injection lasted from 15° BTDC to 5° ATDC. Thus, 40 time steps were used to simulate injection; they correspond to 400 injected droplet packets. The number of droplets in each packet depended on the packet number used to discretize the droplet distribution function. At most 10 000 droplets were used in the calculations. Numerical studies (ref. 26) have shown that this number is more than adequate to predict the flow field. Comparisons with experimental data (ref. 26) have also shown that good agreement can be obtained with fewer droplets.

Effects of Swirl

Swirl is defined here as the angle between the azimuthal and radial velocities at the inlet port, which is circumferential and located at the cylinder wall. The swirl angle was varied from 0° to 45°.

Liquid fuel was injected between 15° BTDC and 5° ATDC in an amount that corresponded to an equivalence ratio of 0.689 and an injection velocity of 21.50 m/sec. The injection angle was 78° with respect to the cylinder centerline. This angle was selected so that the spray did not strike the piston. The fuel was injected at a temperature of 293 K, with a peak point in the Rosin-Rammler distribution at 30.8 μm. A constant wall temperature of 500 K was prescribed throughout the engine cycle.

For the hollow spray employed in the two-stroke engine calculations, droplet coalescence and collisions are less important than for a solid spray because of the expanding surface area of the spray. Droplet breakup, however, may be important in determining the spray penetration, vaporization, and mixing in high-pressure hollow sprays (ref. 11).

Some of the numerical results obtained under motored conditions are presented in the following figures. The different levels of swirl are identified by the angle between the azimuthal and radial velocity components at the inlet port. These figures illustrate the velocity field, fuel penetration, vaporization, and mixing throughout the two-stroke engine cycle.

In figure 3, the velocity profiles in the r-x plane during the intake stroke is shown at 200° ATDC when the intake port and the exhaust valve are open for the swirl angles 0° and 22.5°. In this figure, as well as in those to be presented later in this report, the arrows represent the direction and relative magnitude of the velocity component stored at each grid point throughout the domain. The domain is bounded on the left, right, and top by the cylinder head, piston face, and cylinder wall, respectively. The bottom of each plot is the line of symmetry of the two-dimensional axisymmetric configuration. The axial direction ranges from zero to the piston face (note that this dimension varies with crankshaft angle), and the radial position ranges from the centerline to the cylinder wall. For convenience, the piston always appears at the same location. Note that this is equivalent to presenting the results in the fixed domain used in the calculations.

Figure 3(c) shows a hollow circular cylinder of radius R that is closed at one end by a flat piston which moves up and down in the cylinder. The other end of the cylinder is closed by a flat cylinder head. The piston is connected to the crankshaft (crankshaft throw of radius r_c through a connecting rod (length l_c). The piston moves in a cyclic manner as the crankshaft rotates at a prescribed angular velocity Ω. The clearance C defines the minimum distance between the piston and the cylinder head. Bottom-dead-center (BDC) coincides with the piston's farthest distance from the cylinder head. Crankshaft angle $S = \Omega t$ is arbitrarily assigned such that zero crankshaft degrees (0°) corresponds to top-dead-center (TDC), and 180 crankshaft degrees (180°) corresponds to BDC. The distance between the piston and the cylinder head is denoted by δ. The valve arrangement corresponds approximately to those found in periphery intake port, two-stroke diesel engines. The exhaust port of radius r_v is centrally located in the cylinder head, and is covered and uncovered by the exhaust valve, simulated by an infinitesimally thin disk. The plate penetrates into the cylinder at prescribed crankshaft angles, modeling the opening and closing process in a real engine. The exhaust valve opens at 108° ATDC and closes at 210° ATDC. From 138° to 180° ATDC the valve is stationary in the fully open position v_1. From 108° to 138° ATDC the valve uniformly opens, and from 180° to 210° ATDC it uniformly closes.

Figure 3 shows that a clockwise-rotating eddy is formed near the cylinder wall because of the incoming air flow. In the flowthrough period, when both the intake port and the exhaust valve are open, a counterclockwise-rotating eddy is formed above the valve seat. (Similar flow patterns have been previously observed (refs. 17 to 20).) The flow between the exhaust valve and the exhaust port leaves the cylinder, whereas the flow between the exhaust valve and the piston is directed toward the piston.

For a swirl angle of 22.5°, the global flow field is similar to that for the no-swirl conditions. However, differences exist in the magnitude and location of the eddies. The cylinder wall eddy is smaller and closer to the piston than for the no-swirl conditions. The counterclockwise-rotating eddy is smaller and closer to the cylinder wall than for the no-swirl conditions.

Turbulence energy profiles are shown in figure 4 at 210° ATDC for swirl angles 0° and 22.5°. In this figure, the vertical axis corresponds to the natural logarithm of the turbulent kinetic energy (in cm^2/sec^2). For a swirl angle of 0°, figure 4 shows that the largest level of swirl occurs near the exhaust valve port, where the flow is accelerated during the exhaust stroke. The turbulence levels near the intake port are smaller than those near the exhaust port because of the reduced velocities in that region. For the swirl angle of 22.5°, figure 4 indicates that swirl generates additional turbulence near the exhaust valve. As the gas moves out of the exhaust valve, the flow is nearly axially oriented. Conservation of angular momentum dictates that large azimuthal velocity must occur as the gas is swept along the cylinder head and out of the exhaust valve. This results in large velocity gradients and large levels of turbulent kinetic energy near the exhaust valve. Also, as swirl is increased, turbulence is confined closer to the cylinder head at 210° ATDC.

The effects of swirl levels on droplet trajectories, droplet locations, and fuel vaporization are shown in figures 5 and 6. These figures show the gas-phase velocity profiles and the droplet locations, and the fuel mass fraction isocontours at 350° ATDC. Note that liquid fuel is injected at 345° ATDC from a conical spray located near the cylinder head centerline.

Figure 5 indicates that momentum exchange between the liquid and gas phases drives the flow near the injector and is fundamental in establishing large-scale motions in the cylinder. Piston-driven flow accounts for the only other motion near TDC and is of negligible importance compared with the injection vortex. The spray injection creates a clockwise-rotating toroidal vortex, which grows in the radial and axial directions as more fuel mass is injected. Most of the droplets are entrained by the injection vortex and are swept toward the piston. Dispersion according to size occurs near the spray tip and near the injector, where cross-flow in the vortex sweeps smaller droplets towards the end. Small droplets follow the large-scale motion almost exactly. Vaporization is rapid because of the elevated temperatures in the cylinder; most of the smaller droplets vaporize before they reach the piston.

For a swirl angle of 22.5°, figure 5(b) shows much more complex gas-phase velocity profiles than were present in the no-swirl case, although similar trends are seen near the injector. The injection vortex develops in the clearance space between the head and piston near the injector. Momentum exchange drives the gas-phase velocity in that region, and droplets tend to follow the developing large-scale motions. Away from the injector, the swirl-induced large-scale motions are drastically different from those in the no-swirl case. A strong radial velocity component flow occupies the midcylinder region, and two vortexes return mass along the cylinder head and piston face. The effects of piston motion and the swirl-induced profiles are clearly evident and are not of secondary importance compared to the injection vortex. Significant coupling occurs between the injection-generated vortex and the swirl-created vortexes and tends to draw the droplets deeper into the cylinder, thus increasing the liquid fuel penetration.

Fuel mass fraction isocontours are shown in figure 6 in order to illustrate the fuel vaporization and mixing as a function of the swirl angle. The results presented in figure 6 correspond to pure n-dodecane. For a swirl angle of 0°, figure 6 shows the penetration of the vaporized fuel at 350° ATDC. The fuel mass fraction isocontours are related to the location and size of the droplets shown in figure 7. The vaporized fuel displaces the oxygen (no combustion is present in the calculations reported here) and is diffused in the radial and axial directions.

Figure 6 also shows the effects of swirl on the fuel mass fraction profiles, for a swirl angle of 22.5°. As in figure 5, the fuel mass fraction contours are moderately insensitive to the amount of swirl present in the cylinder. (The main mechanisms responsible for vaporization, temperature and fuel mass fraction, are largely unaffected by increased levels of swirl, because the spray completely drives the flow near the injector.) A moderate change in profiles can be observed between the no-swirl and the 22.5° swirl cases, but almost no change occurs with increasing levels of swirl. Although swirl increases the dispersion of the remaining droplets early in the expansion stroke, these droplets do not have appreciable mass to vaporize. Most of the vaporization that occurs does so early after injection in the regions where injection-induced flows dominate. Hence fuel penetration and vaporization are fairly insensitive to increased levels of swirl. It should be pointed out that this insensitivity may be due to the initial droplet diameters employed in the calculations reported here. For initial larger droplet diameters, it is expected that swirl will have a profound effect on determining the fuel penetration and vaporization.

Figure 7 indicates this trend more dramatically. The figure shows the theoretically injected mass and the gaseous fuel mass plotted as a function of crankshaft angle for the five swirl cases studied in this report. Injection ends at 5° ATDC, and vaporization is nearly completed by 15° ADTC in the no-swirl case and in the 11.25° swirl case. For the other swirl cases, similar degrees of vaporization occur around 10° ATDC. Very few differences are detectable among these remaining swirl cases. Although medium and high swirl resulted in perhaps a 15- to 25-percent increase in vaporization rate, the global effect is a secondary one since the vaporization is so rapid.

In order to achieve better fuel-air mixing, larger spray penetrations are needed; these can be achieved by injecting with higher velocities or by injecting larger droplets. In the calculations presented in this report, the peak of the Rosin-Rammler distribution corresponds to 30.8 μm, and the maximum droplet diameter is 50 μm. Better fuel-air mixing may also be achieved by injecting earlier in the compression stroke, where the gas-phase temperature is lower and the fuel vaporization rate is smaller. Increasing the maximum droplet diameter requires the use of more droplet packets. In the calculations reported here, a maximum of 15 droplet packets were injected every time step at 5 different spatial locations. A maximum number of 200 injection time steps was used. This corresponds to about 15 000 total injected droplet packets. Detailed analyses of the effects of swirl on the flow field and fuel spray penetration, vaporization, and mixing as a function of crankshaft angle and swirl angle are presented in appendix A.

These swirl studies indicate that for the same amount of injected fuel, spray cone angle, injection velocity, and droplet size distribution, large swirl angles result in faster vaporization rates, larger fuel penetration, and better fuel-air mixing. In order to obtain a better fuel-air mixing, calculations need to be performed with different injection velocities, droplet size distribution, spray cone angles, injection rates, and injection times in order to assess the effects of these parameters on the spray penetration and vaporization and on the fuel-air mixing. The ultimate goal of these studies is to determine the optimum injection conditions to achieve good mixing between the fuel and the oxidizer.

Injection optimization studies generally include the effects of engine speed, injection angle, injection duration, injection rate, squish, and swirl. The effects of engine speed, injection angle, spray cone angle, and droplet distribution friction are presented next.

Effects of Engine Speed

The effects of engine speed on the flow field and droplet locations are shown in figure 8. The speeds chosen where 1500 and 2000 rpm; the case of 1000 rpm has been investigated for different swirl levels, and the results can be found in appendixes B and E. Figure 8 shows the u-v gas-phase velocity field and the droplet locations at 360° ATDC for 0° swirl angle and engine speeds of 1500 and 2000 rpm. Figure 8 clearly illustrates the presence of a clockwise-rotating eddy located near the cylinder wall. This eddy was created during the intake process and persists during a large fraction of the compression stroke. For convenience, this eddy is named the "intake" eddy. The fuel injection creates two eddies: the first one rotates clockwise and is located between the fuel spray and the cylinder centerline; the other vortex rotates counterclockwise and is located between the cylinder head and the fuel spray. For convenience, these eddies are named the "clockwise" and "counterclockwise" injection eddies.

The clockwise injection eddy entrains liquid droplets. The amount of entrainment decreases with the engine speed, as shown at 360° ATDC (or TDC). The results presented in figure 8 defy physical intuition in some respects. One could expect that as the engine speed is increased, the turbulence kinetic energy and gas-phase velocity increase. Therefore, turbulent dispersion and droplet vaporization rate should increase. The results shown in figure 8 show that the opposite is true, namely, that droplet dispersion decreases with the engine speed. One can conjecture that high levels of turbulence are normally associated with high levels of turbulence dissipation and that at high engine speed, the dissipation terms in the turbulence kinetic energy equation are larger than those at lower engine speed.

The results presented in figure 8 correspond to the same injection velocity. Also, the no-slip condition between the liquid and gas phases was used near the injector. As the engine speed is increased, the piston velocity and the axial velocity increase. Since the droplets are injected against the moving gas flow, they experience larger decelerations as the engine speed increases. This causes a decrease in the droplet vaporization rate at high engine speed as compared to what is observed at lower speed, where the gas-phase velocity is smaller. Furthermore, since the droplets are more decelerated at higher engine speeds, they should come closer to each other, as the results presented in figure 8 indicate. If the droplet packing becomes very large, the thin spray approximation employed in this study may not be applicable, and droplet collisions and coalescence may become very important. In addition, several droplets may be present in a turbulent eddy and should, in principle, damp the turbulent fluctutations if the loading in an eddy becomes large. The effects of several droplets in a turbulent eddy need further investigation. Detailed analyses of the effects of engine speed on the flow field and fuel spray penetration, vaporization, and mixing are presented in appendix B.

The engine speed has a profound effect on the fuel vaporization. Figure 9, which plots the mass of fuel vapor as a function of the engine speed, indicates that the fuel vaporization decreases with the engine speed. At 1000 rpm, most of the fuel has vaporized by about 20° ATDC, whereas fuel remains unvaporized at 35° ATDC at 1500 and 2000 rpm. The results shown in figure 9 may be a consequence of the combustion chamber geometry employed in the calculations presented in this report. Note that the turbulence levels in the cylinder increase with the engine speed, as discussed in appendix B. Large velocities exist in the cylinder at high engine speed. These higher velocities and turbulence should, in principle, increase the droplet drag and heat and mass transfer from the droplets. However, since some of the injection velocity and droplet distributions were used in figure 9 and the no-slip condition was used at the injector, the droplets move to higher (and opposite) velocity regions, which decelerate them and decrease the mass and heat transfer rates.

Effects of Injection Angle

Figure 10 shows the effects of the injection angle at 1000 rpm for a spray cone angle of 156°. Fuel was injected into the cylinder at 45° and 30° BTDC. In these two cases, injection was stopped at 5° ATDC. Figure 10 shows the velocity vectors and droplet locations at selected crankshaft angles in order to illustrate the effects of the injection angle on the flow field and spray penetration.

For an injection angle of 45° BTDC (fig. 10(a)), the spray penetrates along a 78° line with the cylinder centerline and then is entrained by the clockwise injection eddy as the droplets vaporize. Droplet dispersion is clearly visible at 360° ATDC. After the end of injection, many droplets are entrained by the clockwise injection vortex but are unable to completely recirculate. The droplets move radially toward the cylinder wall and axially toward the piston.

For an injection angle of 30° BTDC (fig. 10(b)), the droplets are initially entrained by the clockwise injection eddy and are at a farther distance from the cylinder wall than for an injection angle of 45° BTDC at 360° ATDC. However, the larger droplets penetrate radially farther into the cylinder. Furthermore, the vaporization rate seems to be larger for an injection angle of 45° BTDC.

This can be easily understood, since most of the compression occurs near TDC. Early injection initially results in a farther fuel penetration and little vaporization. Thus, for an injection angle of 45° BTDC, the droplets are not vaporized very much and initially penetrate farther into the cylinder until they are decelerated. Of course, the amount of vaporization increases with time as the piston compresses the flow and the temperature rises because of compression. For an injection angle of 30° BTDC, droplet vaporization is initially larger because of the higher temperature in the cylinder, and the small droplets follow the clockwise-rotating eddy.

The effects of injection angle on the fuel vaporization are shown in figure 11, which indicates that early injection results in larger vaporization rates. Note that for early injections, the cylinder temperatures are low and that the droplets penetrate farther into the cylinder, cooling the gas phase. Early injection results in faster vaporization, whereas for late injection the droplets do not penetrate as much and the temperature decrease during expansion inhibits their vaporization. Detailed analyses of the effects of the injection angle on the flow field, fuel spray penetration, vaporization, and mixing are presented in appendix C.

Effects of Spray Cone Angle

The effects of the spray cone angle on the flow field and fuel vaporization are analyzed in this section. Spray cone angles of 20° and 60° were studied without swirl at 1000 rpm. Figure 12 shows that for the spray characteristics employed in this study, a spray cone angle of 20° strikes the piston at TDC. When the droplets hit the piston, they are reflected specularly (i.e., the angle of reflection is equal to the angle of incidence). A counterclockwise-rotating eddy is formed near the cylinder centerline and piston by the spray and gas entrainment. This eddy entrains droplets which are displaced radially along the piston toward the cylinder wall.

For a spray cone angle of 60°, similar results to those of a cone angle of 20° are obtained until the spray strikes the piston. Afterward, the reflected droplets are entrained by the injection vortex. In contrast with the results presented for a spray cone angle of 20°, the results for a spray cone angle of 60° indicate that the injection-generated vortex entrains more droplets; some of those droplets are displaced toward the cylinder head, others recirculate and vaporize. Detailed analyses of the effects of the spray cone angle on the flow field and fuel spray penetration, vaporization, and mixing are presented in appendix D.

The effects of the spray cone angle on the vaporization rate are shown in figure 13. This figure indicates that fuel vaporization increases with the spray cone angle. More fuel is vaporized for a spray cone angle of 60° than for an angle of 20°. In the latter case, many droplets strike the cold piston and move along it, where they remain unvaporized. The slope of the fuel vapor mass shown in figure 13 decreases with the spray cone angle. Therefore, it may be concluded that the counterclockwise-rotating injection eddy created for a cone angle of 20° is more effective in vaporizing the fuel droplets than that created by larger spray cone angles. The results shown in figure 13 clearly indicate that for spray cone angles larger or smaller than 120°, larger vaporization rates are obtained than for a spray angle of 120°. This seems to be due to the injection-generated vortex. Of course, spray cone angles larger than 156° may be subjected to the influence of the cold cylinder head and may result in smaller vaporization rates. The results presented in figure 13 indicate that there may be a critical spray angle such as 120° for which the effects of the injection-generated eddies are not so important. Note that for small swirl angles, most vaporization occurs in the counterclockwise-rotating injection-induced vortex, which is located between the spray and the cylinder wall, whereas for larger cone angles (for example, 120°) most vaporization occurs in the clockwise-rotating injection-generated eddy, which is located between the spray and the cylinder centerline. Therefore, the eddies formed during the injection process play an important role in determining the spray vaporization rate.

Effects of Droplet Distribution Function

In figure 14 the flow field and droplet locations are shown for the two droplet distribution functions presented in table II. The results presented in figure 14 correspond to 1000 rpm and a spray cone angle of 156°. The droplet distribution functions are of the Rosin-Rammler type with maximum located at 30.8 and 50 μm, and maximum droplet diameters are 50 and 100 μm, respectively. The objective of using two droplet distribution functions is to determine the spray penetration and vaporization as a function of the droplet diameter for an injection angle of 15° BTDC.

The results presented in figure 14 complement those presented earlier in this section in that for a distribution function characterized by d_{peak} = 30.8 μm and d_{max} = 50 μm, the effects of engine speed (here 1000 rpm), injection angle (here 15° BTDC), and spray cone angle (here 156°) can be compared. It should be pointed out that the calculations at 1000 rpm, cone angle of 156°, injection angle of 15° BTDC, d_{peak} = 30.8 μm, and d_{max} = 50 μm are presented in the subsection Effect of Swirl, in which the effects of the intake swirl angle on the flow field and spray penetration and vaporization are investigated. The results of these calculations at 1000 rpm are repeated here in order to clearly indicate the effects of the droplet distribution function on spray penetration and vaporization.

Figure 14 clearly indicates that for the bigger droplet distribution, the droplets essentially move along a trajectory which forms 78° with the cylinder centerline, except for some amount of lateral dispersion. Figure 14 also shows that very few droplets are entrained by the injection-generated eddies.

Figure 15 shows the effects of the droplet distribution function on the fuel vaporization rate. Note that for a distribution function with d_{peak} = 30.8 μm most droplets have vaporized by about 15° ATDC, whereas for a distribution with d_{peak} = 60 μm most droplets are vaporized by 60° ATDC. Thus, the larger the droplets, the greater the time required for their vaporization. Note that under motored conditions, large swirl levels may throw the larger droplets against the cold cylinder wall, where some may remain unvaporized. Thus, although large droplets and large swirl angles result in large penetration, they may result in large amounts of unvaporized liquid fuel. There is, of course, a problem in analyzing the interaction between the liquid droplets and the boundary layers along solid walls. Depending on the angle of incidence, turbulence levels, temperature, and other factors, the droplets may bounce off, attach, or shatter at the solid walls. This complex phenomenon has been neglected in the calculations presented here since a specular reflection was used for the droplets colliding against the solid walls. Detailed analyses of the effects of the droplets distribution function are present in appendix E.

CONCLUDING REMARKS

A two-dimensional model for axisymmetric piston-cylinder configurations has been developed to study the flow field in two-stroke, direct-injection diesel engines under motored conditions. The model accounts for turbulence by means of a two-equation model for the turbulence kinetic energy and its rate of dissipation. A discrete droplet model has been used to simulate the fuel spray. The effects of the gas-phase turbulence on the droplets have been considered by imposing on the mean droplet velocity, a velocity fluctutation which depends on the turbulence kinetic energy of the gas phase. Random axial and radial locations used to simulate the fuel injection account for the intermittency of the liquid fuel jet breakup into ligaments and droplets. It has been shown that a fluctuating velocity can be added to the mean droplet velocity every time step, if the time step is small enough. Large time steps overpredict the spray penetration.

Good agreement with experimental data of Hiroyasu and Kadota (ref. 1) for a range of ambient pressures in diesel-engine environments was obtained by using the thin spray approximation employed in this report. However, the spray penetration was underpredicted at large time steps because droplet collisions and coalescence were ignored. There is ample evidence (ref. 29) that droplet collisions are important, particularly near the injector. Droplet breakup may also be important in determining the droplet size away from the injector (ref. 11).

Current aerodynamic theories of surface breakdown (ref. 29) are linear and do not provide enough information to accurately determine the initial droplet size. Furthermore, these theories cannot accurately predict the nonlinear phenomena associated with droplet formation (refs. 31 and 32) and have several limitations (ref. 27). Therefore, in the absence of accurate experimental data and analytical models of droplet breakup, one must be cautious in assessing the prediction capabilities of multidimensional spray models. These models contain many parameters which can be adjusted to accurately predict the spray penetration in stagnant ambients, even if Taylor's aerodynamic theory is used to estimate the initial droplet size (refs. 6, 27, and 28) and if droplet collisions and coalescence are considered (ref. 3).

The spray thickness depends on the liquid jet instabilities and breakup into ligaments and droplets, which in turn depend on the nozzle geometry, boundary-layer instabilities, flow relaxation, turbulence, and other factors (refs. 27 and 28). These phenomena are not understood, and discrete droplet models are applicable to the ligament regime. It is believed that future experiments should be designed to provide accurate initial conditions for the droplets at the end of the ligament regime. Without this information, multidimensional models for direct-injection diesel engines cannot be used as truly predictive tools. Perhaps high-speed photography, light scattering, and holographic (ref. 33) and x-ray techniques can be used to determine the intact core and the ligament regime lengths. Electrical techniques have some limitations (refs. 34 and 35) in accurately determining these lengths.

Calculations of the motored two-stroke diesel engine were reported under different operating conditions in order to assess the influence of intake flow swirl angle, engine speed, injection angle, spray cone angle, and initial droplet distribution of the flow field and spray penetration and vaporization.

The results of the calculations reported here indicate that spray penetration and vaporization, velocity, and turbulence kinetic energy increase with the intake swirl angle. As the swirl angle is increased, the droplets are thrown against the cold cylinder wall, and the effects of injection-generated eddies on the fuel vaporization are small. Most droplets vaporize before crossing midcylinder. The fuel vaporization rate decreases with the engine speed. As the engine speed is increased, the gas-phase velocity and turbulence kinetic energy increase. This results in larger axial velocities toward the cylinder wall which decelerate the droplets injected into the cylinder. This deceleration and larger turbulent fluctuations at high engine speed initially result in larger drag and mass and heat transfer. However, once the droplets are decelerated and their velocities are close to those of the gas phase, the heat, mass, and momentum exchanges decrease.

Fuel injection along the cylinder centerline results in a spray which strikes the piston and creates a counterclockwise-rotating eddy which displaces the droplets radially toward the cylinder wall and axially toward the cylinder head. As the spray angle is increased, two injection-generated eddies may result. One of the eddies rotates clockwise and is located between the cylinder centerline and the spray; the other is located between the cylinder head and the spray and rotates counterclockwise. The clockwise-rotating eddy contributes more toward the spray vaporization, and fuel vapor is located near the centerline and carried toward the cylinder wall. However, for large spray cone angles (larger than about 120°) the air entrainment decreases, the droplet velocities decrease because of the momentum exchange with the gas phase and large surface of the spray, and the fuel vaporization decreases. Therefore, for fixed operating conditions, the spray cone angle has a strong effect on the fuel penetration and vaporization.

For the same amount of liquid fuel injected into the cylinder, the spray penetration increases as the droplet size increases. Broad droplet distribution functions result in almost conical (rectilinear) spray trajectories. In some cases, the droplets strike and bounce off the piston and cylinder wall. These droplets are later entrained by the piston-driven flow in the expansion stroke and vaporize near the cylinder wall. For distribution functions where droplets of diameters smaller than 50 μm are used, the droplets vaporize before they reach the cylinder wall and piston. These droplets vaporize in the region occupied by the injection-generated eddies.

The effects of the injection angle on the spray penetration and vaporization indicate that early injection results in larger spray penetration because of the lower temperatures in the cylinder and because of vaporization cooling. Some vaporization occurs as the droplets move through the cylinder; however, most vaporization occurs near TDC, where the cylinder temperatures are the highest. Late injection results in fast vaporization and small spray penetration because the droplets are subjected to high temperatures from the beginning of injection.

The results presented in this report indicate that good spray penetration, vaporization, and mixing can be achieved by injecting droplets of maximum diameters between 50 and 100 μm along a 120° cone at about 315° BTDC for an intake swirl angle of 30°. However, even under these optimum conditions the fuel vapor does not reach the corner between the cylinder wall and the cylinder head.

The results presented in this report also indicate that spray penetration and vaporization are insensitive to turbulence levels within the cylinder. The increase of the intake swirl number, although beneficial to the spray penetration, has the following disadvantages: (1) the droplets are thrown toward a localized region at the cylinder wall, and (2) poor fuel mixing is obtained.

In order to increase the fuel vaporization rate and mixing, the results presented here indicate that squish is necessary. Squish can be obtained by a bowled piston, which creates in the compression stoke a radial motion directed toward the cylinder centerline, and recirculation zones within the bowl. These zones contribute to a better mixing of the fuel and oxygen. Note that the results presented in this report (particularly those which show that little fuel vapor reaches the corner between the cylinder head and the cylinder wall) clearly indicate the need for a bowled piston to achieve better fuel mixing.

APPENDIX A. - DETAILED EFFECTS OF SWIRL

The effects of swirl on the flow field and fuel vaporization are analyzed in detail in this appendix. The swirl angles chosen were 0°, 11.25°, 22.5°, 30°, and 45°. Figure 16 shows the u-v gas-phase velocity field at 200°, 240°, 270°, 300°, and 345° ATDC.

For a swirl angle of 0° (i.e., no swirl), figure 16 shows that, as the piston covers the intake port and the exhaust valve closes, the cylinder wall eddy is displaced toward the cylinder centerline and piston. The counterclockwise-rotating eddy is displaced towards the cylinder head, and a new clockwise-rotating eddy is located between the piston and the valve. The clockwise-rotating eddy and the cylinder wall eddy both move toward the cylinder head (240° ATDC) during the compression stroke. At 270° ATDC, only the counterclockwise-rotating eddy is present in the cylinder. This eddy is elongated in the radial direction and is compressed and damped away in the compression stroke. At 300° ATDC, the grid employed in the calculation is not able to resolve the eddy structure, although a complex flow pattern can be seen near the cylinder head. By this angle, the piston drives the flow which has become unidirectional except near the cylinder head, where the counterclockwise-rotating eddy was once located. Similar flow patterns are observed in the rest of the compression stroke until injection starts at 345° ATDC. The velocity vector plots for a swirl angle of 11.25° are similar to those shown for the no-swirl case.

For a swirl angle of 22.5°, the global flow field is similar to that for the no-swirl conditions. However, differences exist in the magnitude and location of the eddies. The cylinder wall eddy is smaller and closer to the piston than for the no-swirl conditions. The counterclockwise-rotating eddy is smaller and closer to the cylinder wall and approaches the cylinder head as the piston compresses the flow. This eddy breaks down into two new eddies as a result of the complex interaction between the flow and swirl. Eddy breakdown is almost periodic during the compression stroke, with a period of approximately 20°. This makes plots of velocity vectors at larger intervals misleading. For example, at 210° ATDC, five eddies can be observed in the velocity plots: two eddies are located at the cylinder wall (these eddies are the result of the breakdown of the eddy located at the cylinder wall earlier in the intake stroke), two eddies are located in midcylinder, and the fifth eddy is located above the exhaust valve seat and between the piston and the exhaust valve. These five eddies move toward the cylinder wall because of the azimuthal velocity (swirl) and interact with each other in a complex manner. These interactions result in eddy damping and merging. By 235° ATDC, the five eddies are still present but have been displaced to new locations within the engine cylinder. At 240° ATDC only two eddies can be observed: a counterclockwise-rotating eddy located in midcylinder and a counterclockwise-rotating eddy located near the cylinder head. The midcylinder eddy is displaced toward the cylinder head and cylinder wall and yields an elongated eddy at 255° ATDC. This eddy is displaced toward the cylinder wall and breaks down into two new eddies at about 260° ATDC. The eddy located near the cylinder wall and piston is damped away during the compression stroke. At 270° ATDC, only one eddy is shown in the velocity plots. This eddy is damped away and disappears during the compression stroke. After 300° ATDC the character of the large-scale motion changes. Piston motion and viscous dissipation in the cylinder combine to prohibit swirl-induced vortex merging. Swirl and piston motion create a single counterclockwise-rotating eddy near the cylinder head. At about 300° ATDC, this eddy is displaced toward the cylinder wall and damped away, and it disappears in the compression stroke.

For a swirl angle of 30°, figure 16 shows some typical velocity vector plots. A comparison between the velocity plots with swirl angles of 22.5° and 30° indicates that as the swirl is increased, the eddies move away from the cylinder centerline toward the cylinder wall, and the flow seems more complex. For example, at 210° ATDC, three eddies are seen in the engine cylinder: the intake port-generated eddy, the intake-generated eddy which was originally located between the piston and the exhaust valve, and an eddy located at the corner between the cylinder head and the cylinder wall. From about 215° to 225° ATDC, the intake port-generated eddy moves toward the piston and is elongated in the radial direction. During that crankshaft cycle interval, the intake-generated eddy, originally located between the piston and the exhaust valve, breaks down into two new eddies, which are displaced toward the piston. By 240° ATDC, only one of these eddies can be seen in the engine cylinder. The remaining eddy, located in midcylinder, is displaced toward the cylinder head by the piston motion, and toward the cylinder wall because of swirl. This eddy, in turn, breaks down into new eddies, which merge together later in the compression stroke. The resulting eddy is located near the cylinder head but moves toward midcylinder (270° ATDC). A new eddy is created near the cylinder head because of swirl at about 280° ATDC. This eddy is damped away later in the compression stroke and yields a radial motion along the cylinder head.

Similar results are found with swirl angles of 36° (not shown here) and 45°. Figure 16 indicates that swirl generates extensive coupling between the radial and axial velocity components. Even low levels of swirl induce vortex merging and breakdown shortly after the flowthrough period. The increased levels of large-scale motion could be beneficial in thoroughly mixing unscavenged exhaust products prior to injection on the next cycle (refs. 17 and 20).

Turbulence kinetic energy profiles are shown in figure 17 during the intake stroke for the five swirl angles presented in this report. In this figure, the vertical axis corresponds to the natural logarithm of the turbulent kinetic energy (in cm^2/sec^2). The results shown in figure 17 correspond to 210°, 240°, 300°, and 345° ATDC. These turbulence kinetic energy profiles were selected to illustrate the main features of the flow during the compression stroke. For a swirl angle of 0°, figure 17 shows that the largest levels of turbulence occur near the exhaust valve port, where the flow is accelerated during the exhaust stroke.

The turbulence levels near the intake port are smaller than those near the exhaust port because of the reduced velocities in that region. Turbulence is diffused and dissipated in the compression stroke, as shown at 240° and 300° ATDC, but shows steep gradients near the solid walls. Turbulence decays as the piston approaches top-dead-center, as shown at 345° ATDC. For the swirl angle of 11.25°, the distribution of turbulence within the chamber is fairly similar to the case of no swirl, except that there are higher turbulence levels near the exhaust valve.

A comparison between the turbulence levels with no swirl and with a swirl angle of 22.5° indicates that swirl generates additional turbulence near the exhaust valve. As the gas moves out of the exhaust valve, the flow is nearly axially oriented. Conservation of angular momentum dictates that large azimuthal velocity must occur as the gas is swept along the cylinder head and out of the exhaust valve. This results in large velocity gradients and large levels of turbulence kinetic energy near the exhaust valve. Note that as swirl is increased, turbulence is confined closer to the cylinder head at 210° ATDC. After compression the increased levels of swirl contribute to faster turbulent diffusion and dissipation. Turbulence kinetic energy becomes uniform throughout the engine cylinder by 270° ATDC, as was the case with no swirl.

Figure 18 shows the dissipation rate of turbulence kinetic energy for the five swirl angles studied in this report. These figures correspond to 210°, 240°, 300°, and 345° ATDC and illustrate that dissipation rate nonuniformities are present in the early part of the compression stroke. These nonuniformities are diffused in the compression stroke in such a manner that at top-dead-center, the dissipation rate is almost uniform throughout the engine cylinder except for steep gradients at the solid walls. The dissipation rate mimics the turbulent kinetic energy trends: large levels are observed in regions of high turbulence. Figure 18 clearly illustrates that swirl has a profound effect on determining the magnitude and nonuniformity of the dissipation rate. The nonuniformities are due to the eddy topology within the engine cylinder, as the results shown in figure 16 indicate.

Azimuthal velocity profiles shown in figure 19 (plots at crankshaft angles of 200°, 240°, and 345° ATDC) indicate that large swirl levels exist at the intake port and near the exhaust port while the exhaust valve is open. Conservation of angular momentum dictates that high swirl velocities are present at the exhaust port because of the smaller area available to the flow. The swirl velocity diffuses and decreases in the compression stroke mainly because of viscous dissipation. Some of the diffusion is due to the artificial viscosity introduced by the upwind finite-difference scheme employed in the calculations.

As the magnitude of swirl is increased, the results shown in figure 19 indicate that the flow becomes less uniform. This is a direct consequence of the flow topology and larger turbulence levels induced by swirl, as the results presented in figures 16 and 17 indicate. In figure 19, the azimuthal velocity profiles are presented at selected crankshaft angles (360°, 30°, and 108° ATDC) in the expansion stroke. The interaction between the injected fuel and the gas-phase velocity field increases with the swirl levels near the injector. These levels diffuse throughout the combustion chamber. Some gas-phase turbulence is also generated by the interaction between the fuel droplets and gas phase near the cylinder wall; however, this generation is small. Note that the calculations reported here are two dimensional. Therefore, the swirl is axisymmetric. Although the fuel droplets follow helical trajections in the presence of swirl, the flow was assumed to be axisymmetric.

The effects of the different swirl levels on the droplet trajectories, droplet locations, and fuel evaporation are shown in figures 20 and 21. These figures show the gas-phase velocity profiles, the droplet locations, and the fuel mass fraction isocontours at selected crankshaft angles during the injection period and expansion stroke. Note that liquid fuel is injected at 345° ATDC from a conical spray located near the cylinder head centerline.

Under no-swirl conditions, figure 20 indicates that the momentum exchange between the liquid and gas phases drives the flow near the injector and is fundamental in establishing large-scale motions in the cylinder. Piston-driven flow accounts for the only other motion near TDC and is of negligible importance compared with the injection vortex. The spray injection creates a clockwise-rotating toroidal vortex, which grows in the radial and axial directions as more fuel mass is injected. Most of the droplets are entrained by the injection vortex and are swept toward the piston. Dispersion according to size occurs near the spray tip and near the injector, where cross-flow in the vortex sweeps smaller droplets towards the head. Small droplets follow the large-scale motion almost exactly. Vaporization is rapid because of the elevated temperatures in the cylinder; most of the smaller droplets vaporize before they reach the piston. At the end of injection (5° ATDC), the injection-generated vortex persists, and droplets are dispersed across the clearance volume. Only relatively large droplets remain unvaporized; however, they represent a negligible fraction of the total fuel mass. (By 20° ATDC only trace amounts of fuel remain as droplets.) During the expansion stroke, piston-drawn flow develops, and the injection-generated flow decays. The flow is nearly unidirectional by 60° ATDC, and the remaining droplets are located on the piston side of what once was the injection vortex. (The vaporization rate decreases drastically by several orders of magnitude as the gas-phase temperature decreases in the expansion stroke.)

For a swirl angle of 11.25°, figure 20 indicates that swirl induces large-scale vortexes in the region between the cylinder head and cylinder wall. The gas-phase velocity profile near the injector is similar to the no-swirl case, and similar fuel penetration and vaporization patterns are shown in the low-swirl and no-swirl cases.

For a swirl angle of 22.5°, figure 20 shows much more complex gas-phase velocity profiles than were present in the no-swirl case, although similar trends are shown near the injector. The injection vortex develops in the clearance space between the head and the piston near the injector. Momentum exchange drives the gas-phase velocity in that region, and droplets tend to follow the developing large-scale motions. Away from the injector, the swirl-induced large-scale motions are drastically different from those in the no-swirl case. A strong radial velocity component flow occupies the midcylinder region, and two vortexes return mass along the cylinder head and piston face. The effects of piston motion and the swirl-induced profiles are clearly evident and are not of secondary importance to the injection vortex. Significant coupling occurs between the injection-generated vortex and the swirl-created vortexes and tends to draw the droplets deeper into the cylinder, thus increasing the liquid fuel penetration. Some of the droplets appear to strike the piston face. As in the no-swirl case, most of the fuel is vaporized before it can escape from the injection vortex. Thus, although coupling exists, the global effect of swirl on the injected spray vaporization is secondary in nature. During expansion, the remaining droplets are drawn farther toward the cylinder wall and are more completely vaporized.

Figure 20 also shows the velocity vectors and droplet locations for intake swirl angles of 30° and 45°. The graphs show that the injection-dominated region, in which momentum transfer dictates the flow, is relatively insensitive to the swirl levels in the cylinder. The droplets are confined to a relatively compact region near the centerline and around the injection vortex. Increasing the swirl velocity results in secondary coupling between the injection vortex and the two swirl-generated vortexes, and tends to draw the spray deeper into the cylinder. Again, the spray predominantly follows the large-scale motion, and rapid vaporization occurs before the droplets can traverse large distances. The velocity profiles away from the injection vortex are qualitatively similar in form but different in magnitude: higher swirl velocities result in stronger toroidal vortexes. With increasing levels of swirl, more of the remaining droplets are swept towards the cylinder wall, and more complete vaporization occurs.

In figure 20, some velocity vector plots corresponding to the expansion stroke are presented at selected crankshaft angles (60° and 108° ATDC) as a function of the intake port swirl angle.

For a swirl angle of 0°, figure 20 indicates that the piston drives the flow in the expansion stroke; the flow is almost unidirectional except near the cylinder head, where the effects of injection are still felt. As soon as the exhaust port is open, the high-pressure fluid in the cylinder is directed toward the exhaust port; the fluid near the piston still moves with the piston.

For a swirl angle of 22.5°, the droplets located near the cylinder wall follow the unidirectional piston motion. However, a counterclockwise-rotating eddy located at the corner between the cylinder head and the cylinder wall can be seen at 80° ATDC (not shown in figure 20). This eddy is stretched in the expansion stroke and displaced along the cylinder wall. The presence of a counterclockwise-rotating eddy in the expansion stroke can also be observed at 70° ATDC (not shown in figure 20) for swirl angles of 30°, 36°, and 45°. For a swirl angle of 45°, this eddy breaks down into two eddies: one eddy is located at the corner between the cylinder head and the cylinder wall; the other is located at the cylinder head. The vortex breakdown is a function of the swirl angle, as the results previously shown in figure 16 indicate. Figure 20 shows that the lifetime and number of eddies in the engine cylinder depend on the amount of intake port swirl. It also indicates that complex flow patterns result as the swirl number is increased.

Fuel mass fraction isocontours are shown in figure 21 in order to illustrate the fuel vaporization and mixing as a function of the crankshaft angle and the swirl angle. The results presented in figure 21 correspond to pure n-dodecane. For a swirl angle of 0°, figure 21 shows the penetration of the vaporized fuel as a function of the crankshaft angle. The fuel mass fraction isocontours are related to the location and size of the droplets shown in figure 20. The vaporized fuel displaces the oxygen (no combustion is present in the calculations) and is diffused in the radial and axial directions. The highest concentrations of fuel vapor occur near the cylinder head because of the rapid vaporization rates, the dispersive action of the cross-flow velocity near the injector, and the large injection angle used in the calculations. At 70° ATDC, it is clearly seen that very little fuel vapor has reached the cylinder head and the piston.

Figure 21 also shows the effects of swirl on the fuel mass fraction profiles, for swirl angles of 11.25°, 22.5°, 30°, and 45°, respectively. As in figure 20, the fuel mass fraction contours are moderately insensitive to the amount of swirl present in the cylinder. (The main mechanisms responsible for vaporization, temperature and fuel mass fraction, are largely unaffected by increased levels of swirl, because the spray completely drives the flow near the injector.) Similar fuel mass fraction distributions are observed during injection between the case of low swirl (11.25°) and the case of no swirl. A moderate change in profiles can be observed between the no-swirl and the 22.5° swirl cases, but almost no change occurs with increasing levels of swirl. Although swirl increases the dispersion of the remaining droplets early in the expansion stroke, these droplets do not have appreciable mass to vaporize. Most of the vaporization that occurs does so early after injection in the regions where injection-induced flows dominate. Hence fuel penetration and vaporization are fairly insensitive to increased levels of swirl. It should be pointed out that this insensitivity may be due to the initial droplet diameters employed in the calculations. For initial larger droplet diameters, it is expected that swirl will have a profound effect on determining the fuel penetration and vaporization.

Figure 22 shows the Sauter mean diameter (SMD) distributions at selected crankshaft angles as a function of the intake port swirl angle. The Sauter mean diameters presented in figure 22 were calculated from the number of droplets located in the computational cells and were assigned to the nodes in each of these cells. The SMD distributions illustrate the fuel penetration and vaporization as a function of time. The results shown indicate that the droplets are entrained by the injection-generated eddy. Effective dispersion according to size occurs near the injector and at the spray tip because large droplets travel more closely along their original trajectories than do smaller droplets.

Figure 22 also indicates that medium and high swirl levels displace the droplets toward the cylinder wall, as previously shown in figure 20. A comparison of the results obtained with 0° and 22.5° swirl angles indicates that as the magnitude of swirl is increased, the axial spray penetration increases. This can be observed by comparing the results at 30° ATDC. In the absence of swirl, the droplets are entrained by the injection-generated vortex. However, as the swirl angle increases, the larger droplets are displaced toward the cylinder wall. Similar results are shown for swirl angles of 30° and 45°. Also evident are the effects of vaporization. The increased vaporization rates associated with swirl can be observed by comparing the no-swirl case with the 22.5° swirl case. These results indicate that the vaporization rate increases as the intake swirl angle is increased.

Figure 23 shows temperature isocontours through the injection and blowdown periods. The temperature distributions during the intake and exhaust strokes are not presented here. In the intake stroke, the temperature field is almost uniform through the engine cylinder except near the walls, where steep temperature gradients exist. The turbocharger discharges warm air (350 K) into the cylinder through the intake port. This air mixes with the residual mass, and the mixture reaches an almost uniform temperature in the intake stroke.

Figure 23 shows that for the no-swirl conditions, the highest temperature occurs in midcylinder, away from the cold solid walls. The injected fuel exchanges heat with the gas phase and yields regions of low temperatures near the injector. As the fuel penetrates into the cylinder and is vaporized, the gas-phase temperature decreases, and the hot air is displaced toward the cylinder wall, as shown at 10° ATDC. Localized regions of cold gas exist near the injector because of vaporization. In the expansion stroke, the cylinder temperature decreases, liquid droplets remain unvaporized, and the mixture temperature becomes more uniform.

As swirl angle is increased, the spray penetration also increases. This results in larger cold regions in midcylinder. Furthermore, as the swirl angle increases, a larger number of droplets are directed toward the cylinder wall.

Figures 22 and 23 clearly illustrate that there are at least two factors affecting the fuel vaporization: swirl and residence time. High swirl levels increase the momentum, mass, and heat exchanges between the droplets and the gas phase and increase the turbulent dispersion of droplets and diffusion of scalars. However, if the droplets do not spend a sufficient amount of time within the hot turbulent eddies, residing only in the regions that vaporizing droplets have cooled, very little vaporization occurs, and vapor accumulates near the cold cylinder wall, where the temperatures are low and where some droplets remain unvaporized.

In figure 24, the turbulence kinetic energy profiles are shown during the injection period and in the expansion stroke. These profiles indicate that turbulence is almost uniform throughout the engine cylinder at about 350° ATDC, with the exception that injection-generated turbulence is diffused rapidly and becomes uniform shortly after the end of injection. During blowdown (not shown here), turbulence is generated near the exhaust port because of the local acceleration that the flow experiences when exciting the engine cylinder. This local generation of turbulence diffuses throughout the chamber. Additional turbulence is generated when the piston uncovers the intake port and the turbocharger discharges air into the cylinder.

Figure 24 also shows that small levels of turbulence are generated at the piston face and at the cylinder walls. However, this turbulence generation is much smaller than the intake and injection-generated turbulence. Furthermore, the hydrodynamic and thermal boundary layers were not properly resolved in the calculations presented here. Therefore, this well-generated turbulence may be a direct consequence of the poor numerical resolution near the solid walls. It may also be a result of the specular reflection that the droplets experience as they rebound from the solid walls. Depending on the wall temperature, the droplets can collide with the wall, can attach to the wall, or can bounce off or shatter, or both. An accurate representation of these processes, which involve preferential shear, droplet velocity, surface tension, wall temperature, and boundary layer thickness, is not available at the present time. In the absence of better information and experimental data, the results presented in this report when the droplets strike solid walls must be considered with caution.

The heat transfer losses through the cylinder wall increase with the swirl angle; the difference in heat transfer losses through the cylinder wall is about 500 cal/sec between swirl angles 0° and 45°. Similar trends are observed in the heat transfer losses through the cylinder head and the piston. The instantaneous heat transfer losses through the cylinder head are smaller than those through the piston. The heat transfer losses through the cylinder wall peak before top-dead-center because of the cooling effect associated with droplet vaporization (ref. 26).

APPENDIX B. - DETAILED EFFECTS OF ENGINE SPEED

The effects of engine speed on the flow field are shown in detail in figures 25 to 30. The speeds chosen were 1500 and 2000 rpm. The case of 1000 rpm was investigated for different swirl levels and can be found in figure 30 and in appendix E. Figure 25 shows the u-v gas-phase velocity field and the droplet locations at 350°, 360°, 10°, 30°, 60°, and 108° ATDC. Figure 25 clearly illustrates the presence of a clockwise-rotating eddy located near the cylinder wall. This eddy was created during the intake process and persists during a large fraction of the compression stroke. For convenience, this eddy is named the "intake" eddy. The fuel injection creates two eddies: the first one rotates clockwise and is located between the fuel spray and the cylinder centerline; the other vortex rotates counterclockwise and is located between the cylinder head and the fuel spray. For convenience, these eddies are named the "clockwise" and "counterclockwise" injection eddies.

The clockwise injection eddy entrains liquid droplets. The amount of entrainment decreases with the engine speed, as shown in figure 25 at 360° ATDC (or TDC). By the end of injection (5° ATDC) the clockwise injection vortex is displaced radially towards the cylinder wall. The radial and axial penetrations of the spray decrease with the engine speed, as shown at 10° ATDC. Similar results can be observed at 30°, 60°, and 108° ATDC.

The results presented in figure 25 defy physical intuition in some respects. One would expect that, as the engine speed is increased, the turbulence kinetic energy and gas-phase velocity increase. Therefore, turbulent dispersion and droplet vaporization rate should increase. The results shown in figure 25, however, show that droplet dispersion decreases with the engine speed. One can conjecture that high levels of turbulence are normally associated with high levels of turbulence dissipation and that at high engine speed, the dissipation terms in the turbulence kinetic energy equation are larger than those at lower engine speed.

The results presented in figure 25 correspond to the same injection velocity. Also, the no-slip condition between the liquid and gas phases was used near the injector. As the engine speed is increased, the piston velocity and the axial velocity increase. Since the droplets are injected against the moving gas flow, they experience larger decelerations as the engine speed increases; this causes a decrease in the droplet vaporization rate at high engine speed as compared to what is observed at lower speed, where the gas-phase velocity is smaller.

Figure 26 shows the natural logarithm of the turbulence kinetic energy profiles at 350°, 360°, 10°, 30°, and 60° ATDC at 1500 and 2000 rpm. This figure clearly indicates that the turbulence kinetic energy is higher at 2000 rpm than at 1500 rpm. Figure 26 also indicates that turbulence is uniform throughout the engine cylinder except for steep gradients at the cylinder walls. Turbulence is generated by the fuel injection process but is diffused and convected radially and axially throughout the cylinder. After injection is completed, the turbulence levels in the cylinder decay, but some nonuniformities can still be observed near the injector and the cylinder wall at 60° ATDC. Figure 27 shows the natural logarithm of the dissipation rate of turbulence kinetic energy at

350°, 10°, and 60° ATDC at 1500 and 2000 rpm. The dissipation rate mimics the turbulence kinetic energy trends - larger levels of dissipation rate are observed at 2000 rpm than at 1500 rpm.

A clear indication of the fuel penetration and vaporization can be obtained by analyzing the Sauter mean diameter (SMD) distributions. The SMD was computed in each cell by accounting for the total number of droplets in each cell. The SMD profiles are shown in figure 28 at 350°, 360°, 10°, 30°, and 60° ATDC. Figure 28 clearly illustrates that the radial and axial penetration of the spray are higher at 1500 rpm than at 2000 rpm. In fact, the results shown in the figure indicate that droplets follow the clockwise injection vortex more closely at 1500 rpm than at 2000 rpm. Since the same injection velocity was used at 1500 rpm and at 2000 rpm and the no-slip condition between the gas and the liquid phases was imposed near the injector, one would expect that droplet vaporization and dispersion are initially controlled by the random turbulent velocity imposed on each droplet. As the droplets move farther into the cylinder, they should experience more drag at high engine speed than at low engine speed because the gas-phase velocity is higher at 2000 rpm than at 1500 rpm. Therefore, the droplets do not penetrate as much at 2000 rpm as at 1500 rpm. This justifies, in part, the results presented in figures 25 and 28. Furthermore, since the droplets are more decelerated at higher engine speed, they should come closer to each other, as the results presented in figure 25 indicate. If the droplet packing becomes very large, the thin spray approximation employed in this study may not be applicable, and droplet collisions and coalescence may become very important. In addition, several droplets may be present in a turbulent eddy and should, in principle, damp the turbulent fluctuations if the loading in an eddy becomes large. The effects of several droplets in a turbulent eddy need further investigation.

In figure 29, the fuel vapor mass fraction profiles are shown at 1500 and 2000 rpm at 350°, 360°, 10°, 30°, and 60° ATDC. Figure 29 clearly illustrates that more liquid fuel is vaporized and penetrates farther into the cylinder at 1500 rpm than at 2000 rpm. This is a direct consequence of the larger drag and deceleration that the droplets experience at high speed. Figure 29 also shows that fuel vapor is present closer to the cylinder wall and the piston at 1500 rpm than at 2000 rpm.

The temperature in the cylinder at 1500 and 2000 rpm is presented in figure 30. These results illustrate that vaporization cooling is more important at 1500 rpm than at 2000 rpm. These results are consistent with those shown in figures 25, 28, and 29, which illustrate that for the range of engine speed, droplet diameter, injection velocity, spray cone angle, and injection duration studied here, more fuel is vaporized at low speed than at high speed, and that the fuel penetrates farther into the cylinder at lower speed.

The effects of the intake swirl angle at 1500 and 2000 rpm are also presented in figures 25 to 30 in order to compare them with those obtained with a swirl angle of 0°.

Swirl creates complex flow patterns within the engine cylinder. The flow is driven toward the cylinder wall because of centrifugal effects and returns along the cylinder head and piston. However, fuel injection still creates a clockwise injection vortex located near the cylinder centerline.

Figure 25 clearly indicates that as the intake swirl angle is increased, the radial penetration of the spray increases, and fewer droplets are entrained by the clockwise injection eddy. Figure 25 also shows that the axial penetration of the spray decreases as the intake swirl angle is increased. For a swirl angle of 30° and at 30° ATDC, more droplets have vaporized than for no-swirl conditions. In the absence of swirl, the droplets seem to be entrained by the clockwise injection vortex. Figure 26 indicates that turbulence kinetic energy increases with the swirl angle. This increase contributes to droplet dispersion through the random velocity used in the droplet drag. However, turbulence effects seem to be of secondary importance compared with mean flow effects such as the azimuthal velocity.

Figure 28 clearly indicates that the droplets penetrate farther into the cylinder as the swirl angle is increased. For example, for a swirl angle of 30° and at 30° ATDC, most of the droplets are located near the midcylinder, whereas most of the droplets are entrained by the clockwise injection eddy for a swirl angle of 0°. Many droplets have reached the cylinder wall by 60° ATDC and for a swirl angle of 30°. However, the number of droplets which reaches the cylinder wall is small and contributes very little to the fuel vapor distribution. Figure 29 illustrates that fuel vaporization increases as the swirl angle is increased. It also shows that most droplets vaporize before reaching the cylinder wall for a swirl angle of 30°, whereas many droplets remain unvaporized near the cylinder wall for a swirl angle of 0°. Therefore, swirl is beneficial in enhancing fuel vaporization and fuel vapor penetration in the axial direction. However, for the droplet distribution function and the injection velocity used in the calculation presented here, most droplets vaporize before reaching midcylinder for a swirl angle of 30°. For a swirl angle of 0°, the radial penetration of the fuel vapor is larger and is concentrated near the cylinder head.

The temperature profiles presented in figure 30 indicate that vaporization cooling occurs between midcylinder and the cylinder centerline for a swirl angle of 30°, whereas vaporization cooling occurs near the cylinder head and along the clockwise injection vortex for a swirl angle of 0°.

The azimuthal velocity profiles at 1500 and 2000 rpm (not shown here) indicate that the swirl velocity is higher at 2000 rpm than at 1500 rpm. Fuel injection results in higher azimuthal velocities near the injector. The velocities decay as soon as injection stops and become nearly uniform throughout the engine cylinder in the expansion stroke.

APPENDIX C. - DETAILED EFFECTS OF INJECTION ANGLE

Figures 31 and 35 show in detail the effects of the injection angle at 1000 rpm for a spray cone angle of 156°. Fuel was injected into the cylinder at 45°, 30°, and 15° BTDC. In all three cases, injection was stopped at 5° ATDC.

Figure 31 shows the velocity vectors and droplet locations at selected crankshaft angles in order to illustrate the effects of the injection angle and swirl on the flow field and spray penetration. At 335° ATDC, the fuel tip is beyond midcylinder for an injection angle of 45° BTDC, whereas for an injection angle of 30° BTDC the spray is located near the cylinder centerline and is entrained by the clockwise injection vortex.

For an injection angle of 45° BTDC, the spray penetrates along a 78° line with the cylinder centerline and then is entrained by the clockwise injection eddy as the droplets vaporize. Droplet dispersion is clearly visible at 350° and 360° ATDC. After the end of injection, many droplets are entrained by the clockwise injection vortex but are unable to completely recirculate. The droplets move radially toward the cylinder wall and axially toward the piston. However, very few droplets reach the piston. By 60° ATDC most droplets are vaporized, and some droplets can still be observed near the cold cylinder head.

For an injection angle of 30° ATDC, the droplets are initially entrained by the clockwise injection eddy and are farther from the cylinder wall than for an injection angle of 45° BTDC at 350° and 360° ATDC. However, the larger droplets penetrate radially farther into the cylinder. This results in unvaporized droplets at almost the same location at 60° and 108° ATDC for injection angles of 45° and 30° ATDC. Furthermore, the vaporization rate seems to be larger for an injection angle of 45° ATDC. This can be easily understood, since most of the compression occurs near TDC. Early injection initially results in farther fuel penetration and little vaporization, whereas late injection implies little fuel penetration and large vaporization. Thus, for an injection angle of 45° BTDC the droplets are not vaporized very much and initially penetrate farther into the cylinder until they are decelerated. Of course, the amount of vaporization increases with time as the piston compresses the flow, and the temperature rises because of the compression. For an injection angle of 30° BTDC, droplet vaporization is initially larger because of the higher temperature in the cylinder and because the small droplets follow the clockwise-rotating eddy.

Figure 32 shows the turbulence kinetic energy profiles at selected crankshaft angles for the two injection angles considered in this report. The fuel injected into the cylinder creates through shear stresses high and localized levels of turbulence near the injector. This injection-created turbulence decays in the compression and expansion strokes and is diffused throughout the cylinder. Figure 32 shows that the cylinder turbulence is basically independent of the injection angle except for a small region located near the injector. The amount of injection-generated turbulence is, however, smaller than that produced by the intake process.

Figure 33 presents the Sauter mean diameter distributions throughout the engine cylinder for the two injection angles analyzed in this report. Figure 33 indicates that an injection angle of 45° BTDC yields farther radial spray penetration than an injection angle of 30° BTDC. It also shows that for the latter angle, the droplets are entrained by the clockwise injection vortex and are located between midcylinder and the cylinder centerline. The axial penetration of the spray is larger for an injection angle of 45° BTDC than for 30° BTDC. The SMD distributions presented at 30° and 60° ATDC clearly indicate that more droplets are vaporized and penetrate farther into the cylinder for an injection angle of 45° BTDC than for an injection angle of 30° BTDC.

The fuel vapor mass fractions are shown in figure 34. This figure illustrates that as the injection angle is increased, more fuel vapor is located near the cylinder wall and near the piston. For the injection characteristics used in figures 31 to 35, it can be concluded that early injection results in greater spray penetration and vaporization than late injection. Of course, early injection takes advantage of the low temperatures present in the cylinder and vaporization cooling. In late injection, the high temperatures present in the cylinder increase the vaporization rate, and this results in smaller droplets and smaller fuel vapor penetration.

The effects of vaporization cooling are present in figure 34, which illustrates the temperature profiles. Lower temperatures are observed at 330° ATDC near the injector for an injection angle of 45° BTDC than for an injection angle of 30° BTDC. Early injection results in lower cylinder temperatures than late injection because of vaporization cooling in loss temperature flows. Figures 31 to 35 also illustrate the effect of the intake swirl angle on the flow field, droplet locations, turbulence, Sauter mean diameter, and temperature for two different injection angles. Figure 31 shows the increase in the radial spray penetration as the intake swirl angle is increased, and the difference between the gas-phase velocity fields with and without swirl. Without swirl, the flow field is characterized by the intake eddy and the injection eddies, whereas, with swirl, the fluid is "thrown" against the cylinder wall and returns along the cylinder head. A stagnation region is created near the injector because of the inwardly directed flow along the cylinder head and the radial velocity induced by the process.

For an injection angle of 30° BTDC and a swirl angle of 30°, the droplets are entrained by the clockwise-rotating eddy, and the radial spray penetration is larger than in the absence of swirl. However, the axial spray penetration is smaller.

At 30° ATDC, for example, it is shown that in the absence of swirl, the droplets are located near the cylinder head and are entrained by the clockwise injection vortex, whereas, for a swirl angle of 30°, most droplets are located between midcylinder and the cylinder wall. Similar results shown at 60° and 108° ATDC indicate that the radial penetration of the spray and fuel vaporization increase with the swirl angle, whereas the axial penetration decreases.

Figure 32 indicates that turbulence levels in the cylinder increase with the swirl angle but decay at a faster rate because of the larger dissipation rate.

Figure 33 illustrates the axial and radial penetration of the spray in the Sauter mean diameter distributions and indicates that swirl increases the radial penetration of the spray. AT 60° ATDC, figure 33 shows that the unvaporized droplets are located near the cylinder wall for a swirl angle of 30°, whereas in the absence of swirl the unvaporized droplets occupy most of the cylinder and are located near the cold cylinder head.

The fuel vapor profiles shown in figure 34 indicate that in the presence of swirl most droplets vaporize before reaching midcylinder because of the large convection (slip) that the droplets experience. Therefore, the droplets that reach the cylinder wall contribute very little to the total fuel mass in the presence of swirl. In the absence of swirl, the largest fuel vapor concentration occurs near the cylinder head.

The temperature in the cylinder in the absence of swirl is higher than for a swirl angle of 30° because of the smaller vaporization of the droplets, as shown in figure 35.

The azimuthal velocity profiles (not shown here) show steep gradients at the cylinder centerline and at the cylinder wall, but are otherwise almost uniform throughout the cylinder. During injection, there is an exchange of azimuthal momentum between the droplets and gas near the injector; this exchange creates some azimuthal velocity nonuniformities at the injector, which disappear in the expansion stroke.

APPENDIX D. - DETAILED EFFECTS OF SPRAY CONE ANGLE

The effects of the spray cone angle on the flow field and fuel vaporization are analyzed in detail in this section. Spray cone angles of 20°, 60°, and 120° were studied with and without swirl at 1000 rpm. Figure 36 shows that for the spray characteristics employed in this study, with a cone angle of 20°, the spray strikes the piston before TDC. (Figure 36 may be misleading in scale because the cylinder radius is much larger than the clearance.) When the droplets strike the piston, they are reflected specularly (i.e., the angle of reflection is equal to the angle of incidence). A counterclockwise-rotating eddy is formed near the cylinder centerline and piston by the spray and gas entrainment. This eddy entrains droplets which are displaced radially along the piston toward the cylinder wall. The eddy created by the injection process disappears between 10° and 30° ATDC, and the piston drives the flow. This results in the complex flow patterns shown at 30° ATDC. Most droplets are vaporized by 60° ATDC; the ones that do not vaporize represent a small fraction of the total liquid fuel injected into the cylinder. These unvaporized droplets are located near the piston at 60° ATDC, but they do not follow the piston motion, as the velocity plots at 108° ATDC indicate.

For a spray cone angle of 60°, the results are similar to those of a cone angle of 20° until the spray strikes the piston. Afterward, the reflected droplets are entrained by the injection vortex, which is closer to the piston than for a spray cone angle of 156°. In contrast with the results presented for a spray cone angle of 20°, the results for a spray cone angle of 60° indicate that the injection-generated vortex entrains more droplets; some of those droplets are displaced toward the cylinder head, and others recirculate and vaporize. However, the radial spray penetration is small until the injection-generated vortex is destroyed by the piston-driven flow. At 30° ATDC, the negative axial velocities induced by the injection-generated vortex eddy become positive because the piston drives the flow; however, positive radial velocities are observed near the piston, and negative radial velocities are observed near the cylinder head. The positive velocities force the droplets to move toward the cylinder wall near the piston, and the negative velocities force the droplets to move toward the cylinder centerline near the cylinder head. When this occurs (at about 30° ATDC), the radial penetration of the spray increases. A comparison of the results for cone angles of 20° and 60° at 108° ATDC clearly indicates that for 20°, there are still unvaporized droplets in the cylinder, whereas, for 60°, most droplets vaporize in the injection-generated eddy. Large unvaporized droplets remain in the cylinder for a spray cone angle of 20° as a direct consequence of the spray angle. For a 20° cone angle, the droplets traverse the clearance in a very short time and strike the cool piston, where the absence of large velocities and the presence of low temperatures inhibit their further vaporization. As the cone angle is increased, the droplets bounce off from the piston and are trapped in the injection-generated eddy where they vaporize. For a cone angle of 0°, the droplets would strike the piston near the centerline and would remain trapped there because they were moving against the piston, where the temperature is low. For a cone angle of 60°, a small clockwise-rotating eddy is formed by the injected fuel near the cylinder centerline.

For a cone angle of 120°, two eddies are generated by the injection process. One clockwise eddy is formed between the spray and cylinder centerline, and the other counterclockwise-rotating eddy is located between the spray and the cylinder head. At 350° ATDC, these eddies are clearly visible, as are the large droplets. Eventually, the spray strikes the piston, and some droplets are entrained by the clockwise injection vortex near the piston. After injection, the clockwise injection vortex is elongated in the radial direction because of the piston motion. This enlongation results in droplets moving radially toward the cylinder wall near the cylinder head. However, as the droplets move toward the cylinder wall, the piston-driven flow entrains them in the direction of the piston, and the injection vortex decays. Many droplets vaporize in the injection vortex. Some droplets are accumulated near the piston, where the velocity and temperature are low; these droplets vaporize slowly but do not follow the gas-phase velocity field. Some droplets remain unvaporized between the midcylinder and the centerline; these droplets were originally trapped in the injection vortex and were the last to be injected into the cylinder.

Figure 37 shows the turbulence kinetic energy profiles for spray cone angles of 20°, 60°, and 120°. For a spray angle of 20°, large levels of turbulence are generated at the shear layers of the injected spray strikes. These levels of turbulence decay in the expansion stroke, and by 60° ATDC turbulence is almost uniform throughout the cylinder except for very steep gradients near the walls. Note that there is a large dissipation rate at the cylinder wall, where background levels of turbulence are smaller. Similar trends can be observed for a spray cone angle of 60°. However, for a cone angle of 120°, most turbulence is generated near the injector at the shear layers of the spray and in the injector-generated eddies. Again, this turbulence decays and becomes uniform in the expansion stroke.

The Sauter mean diameter distributions presented in figure 38 clearly indicate the spray penetration and vaporization. For a cone angle of 20°, the droplets first strike the piston (350° ATDC), bounce off, and move along the piston (360° ATDC). By 10° ATDC, the injection-generated eddy has almost been destroyed by the piston-driven flow, and the droplets concentrate near the piston (30° ATDC). Some droplets are still moving radially, driven by the remains of the injection eddy (60° ATDC), toward the cylinder wall along the piston. Note that by 60° ATDC, droplets remain unvaporized near the cylinder centerline and near the piston, where the temperature is low. (In the calculations reported here, the piston temperature was set equal to 500 K.)

For a spray cone angle of 60°, figure 38 illustrates that the injected droplets first strike the piston and then are entrained by the counterclockwise injection-generated vortex toward the cylinder head (350° and 360° ATDC). Some of the entrained droplets strike the cold cylinder head, where they remain unvaporized. The counterclockwise injection eddy forces some of the droplets to move radially toward the cylinder wall along the piston. However, there piston-driven flow prevents these droplets from reaching the cylinder wall. As a consequence, unvaporized droplets can be found near the piston and cylinder head. Some unvaporized droplets can also be found near the cylinder centerline, where they were trapped by the counterclockwise injection eddy.

For a spray cone angle of 120°, figure 38 shows that the spray first strikes the piston and that some droplets are entrained by the clockwise injection eddy (360° and 10° ATDC). However, as the piston drives the flow and the injection vortex is elongated in the radial direction, the droplets are replaced radially toward the cylinder wall. The piston-driven flow does not permit the droplets to reach the cylinder wall. As a consequence, unvaporized droplets remain between midcylinder and the cylinder centerline at 60° and 108° ATDC.

The distribution of fuel vapor in the cylinder for the three spray cone angles investigated is shown in figure 39 in order to illustrate the fuel vapor penetration. For a cone angle of 20°, this figure shows that the fuel vapor is concentrated along the spray envelope near the cylinder centerline. The largest fuel vapor concentration is located above the centerline near the piston (350° ATDC). As the droplets move radially along the piston, they vaporize, and fuel vapor concentration increases radially and axially. The increase in the axial direction is due to droplet dispersion and fuel vapor diffusion (360° and 10° ATDC). As the piston recedes from TDC, diffusion and axial convection contribute to the fuel vapor distribution near the piston. However, in the expansion stroke (by 60° ATDC) the effects of convective vaporization are small, and the fuel vapor diffuses radially and axially.

For a cone angle of 60°, the vaporization of the droplets entrained by the counterclockwise injection eddy contributes to the radial penetration of the fuel vapor toward the cylinder head (360° ATDC). However, once the piston drives the flow and the injection eddy is partially destroyed, the droplets moving radially toward the cylinder wall vaporize, and fuel vapor concentrates along the piston (30° and 60° ATDC). A comparison between the fuel distributions for cone angels of 20° and 60° shows that as the cone angle increases, the fuel penetrates farther (in both the radial and axial directions) into the cylinder. In fact, the case of a 60° cone angle yields more uniform fuel vapor distribution than the case of a 20° cone angle.

For a spray cone angle of 120°, the highest fuel vapor concentration is located along the spray trajectory and in the clockwise injection eddy (10° ATDC). Fuel vapor is displaced radially along the cylinder head by the remains of the injection eddy and by diffusion.

A comparison between the fuel distributions for the cone angles of 60° and 120° shows that for the 60° angle, the fuel vapor is concentrated near the piston, whereas for the 120° angle, the fuel vapor is concentrated between the midcylinder and the cylinder centerline. In both cases, fuel does not reach the corner between the cylinder head and the cylinder wall, and most fuel remains concentrated in very localized regions. A more uniform fuel distribution could be obtained by introducing a bowl in the piston so that squish motions contribute to the fuel vaporization and mixing.

The temperature distributions (not shown here) indicate that vaporization cooling occurs along the spray trajectory and near the piston where the spray strikes. Thus, for a cone angle of 20°, vaporization cooling occurs near the cylinder centerline and along the cylinder wall. However, the temperature profiles become nearly uniform in the expansion stroke at about 60° ATDC, indicating that the decrease in temperature associated with the expansion stroke prevents further droplet vaporization.

Figures 36 to 39 also illustrate the effects of swirl on the flow field and spray penetration and vaporization for the three spray cone angles investigated in this study.

For a spray cone angle of 20°, figure 36 indicates that the gas-phase velocity field is strongly affected by swirl; however, the fuel penetration is not affected very much at 350° ATDC because the droplets are located near the centerline, where the azimuthal velocity is nearly zero. At 360° ATDC, the radial motion of the droplets along the piston is inhibited by the air moving radially toward the centerline. This radial flow is due to swirl. Thus, at 360° ATDC, the droplets are entrained by the clockwise injection eddy for a swirl angle of 30°, whereas they move along the piston for the case of no swirl. For a swirl angle of 30° and a cone angle of 20°, centrifugal effects push the droplets toward the cylinder wall at 10° ATDC. Most of these droplets vaporize, and the ones which do not vaporize are located near midcylinder at 30° ATDC. At 60° and 108° ATDC, most of the unvaporized droplets are located between the cylinder wall and midcylinder. These unvaporized droplets are smaller than those observed in figure 36 for a swirl angle of 0° and a cone angle of 20°.

Figure 37 indicates that the levels of turbulence kinetic energy increase as the swirl angle is increased. Turbulence generation occurs at the shear layers of the injected spray and at the piston where the spray strikes. In general, high levels of turbulence are associated with high levels of dissipation rate. Thus, for example, at 60° ATDC, the turbulence levels for a cone angle of 20° with swirl are larger than for a spray with the same cone angle but without swirl. Also at 60° ATDC, the background levels of turbulence are smaller near the walls, where a Neumann condition was used to calculate the turbulence kinetic energy.

Figure 38 shows that for a cone angle of 20°, the initial spray penetration (350° ATDC) is not affected by the intake swirl. At 360° ATDC, figure 38 indicates that in the absence of swirl, the droplets move radially along the piston, whereas for a swirl angle of 30° the droplets are entrained by the counterclockwise injection eddy and move toward the cylinder head. At 10° ATDC, centrifugal effects push the droplets toward the cylinder wall, but in general, the droplets remain trapped in the injection vortex. The radial displacement of the droplets increases with the crankshaft angle, and by 60° ATDC, most unvaporized droplets are located between the cylinder wall and midcylinder. In the absence of swirl, unvaporized droplets are located along the cold cylinder centerline and piston.

The fuel vapor distributions for the three spray cone angles investigated in this report are shown in figure 39 for intake swirl angles equal to 0° (no swirl) and 30°. At 350° ATDC, the fuel vapor isocontours are similar for the cases with and without swirl for a cone angle of 20° because droplets are injected near the centerline with a small angle. At 360° ATDC, the effects of swirl are clearly seen. In the absence of swirl, the fuel vapor is concentrated at the corner between the cylinder centerline and the piston. In the presence of swirl, however, vaporization occurs in the counterclockwise injection eddy, which yields almost uniform fuel vapor concentration in the axial direction. Similar trends can be observed at 10°, 30°, and 60° ATDC: in the absence of swirl, the fuel vapor diffuses toward the cylinder head, whereas in the presence of swirl, the fuel vapor diffuses radially toward the cylinder wall. In either case, at least half of the cylinder contains negligible amounts of fuel vapor. For a cone angle of 20° in the absence of swirl, the fuel vapor is located near the piston, whereas in the presence of swirl, fuel vapor is mainly concentrated between midcylinder and the cylinder centerline.

Small amounts of fuel vapor are present near the cylinder wall because most of the droplets vaporize in the counterclockwise injection eddy before they reach midcylinder. Again, squish would probably help to distribute the fuel vapor uniformly.

The velocity profiles for a cone angle of 60° are presented in figure 36 for swirl angles of 0° and 30°. These profiles indicate that the gas-phase velocities are higher for a swirl angle of 30° than for 0°. Figure 36 also shows that there is a steady radial flow along the cylinder head toward the cylinder centerline for a swirl angle of 30° and that at 350° ATDC, the fuel penetration is almost insensitive to the intake swirl angle. At 360° ATDC, droplets remain trapped in the counterclockwise injection eddy, which moves them closer to the cylinder head for the larger swirl angle analyzed. In the absence of swirl, the droplets move radially along the piston toward the cylinder wall more radially than for a swirl angle of 30°. This is because in the presence of swirl, there is a radial air flow toward the centerline along the piston. This flow is opposed to the droplet motion. Without swirl, fuel droplets remain in the injection eddy near the piston, whereas for a swirl angle of 30°, droplets are located between the cylinder head and the piston at 10° ATDC. At 30° ADTC, the piston drives the flow and destroys the counterclockwise injection eddy. For a swirl angle of 0° most droplets are located near the piston, whereas for a swirl angle of 30°, unvaporized droplets can be seen near the cylinder head. Similar results can be observed at 60° ATDC. At 108° ATDC, most droplets have vaporized and are located near the piston for a swirl angle of 0°, whereas they are located near the cold cylinder head and wall for a swirl angle of 30°. Note that in the presence of swirl the droplets are first moved toward the cylinder head by the counterclockwise injection eddy and are then pushed by the centrifugal effects toward the cylinder wall. Since both the cylinder head and the walls are cold, some droplets remain unvaporized in the vicinity of those walls, as the results presented in figure 36 indicate for a swirl angle of 30°.

Figure 37 clearly illustrates that in the absence of swirl, turbulence generation occurs at the shear layers of the injected spray and at the piston where the droplets strike. However, in the presence of swirl, turbulence is mainly generated at the shear layers of the injected spray and in the counterclockwise injection eddy. Figure 37 also shows that the levels of turbulence in the cylinder increase with the swirl angle.

Figure 38 shows that the initial spray penetration is almost independent of the swirl angle (350° ATDC). The Sauter mean diameter distributions at 360° ATDC (TDC) indicate that for a swirl angle of 0°, the droplets are entrained by the counterclockwise injection eddy away from the cylinder centerline. These droplets are dispersed in the radial direction near the piston (10° ATDC) and move along it (60° and 108° ATDC). However, in the presence of swirl, the droplets move radially toward the cylinder wall and penetrate radially farther than in the absence of swirl. At 108° ATDC and for a swirl angle of 30° most unvaporized droplets are located near the corner between the cylinder head and the cylinder walls. However, at the same crankshaft angle without swirl, the unvaporized droplets are located near the cold piston and near the centerline.

Figure 39 illustrates that at 350° ATDC, the fuel droplet distribution is almost independent of the intake swirl angle. At 360° ATDC, the fuel vapor is present near the piston for the no-swirl case, whereas it is almost distributed from the piston to the cylinder head by the counterclockwise injection eddy for a swirl angle of 30°. Droplets still vaporize at the beginning of the expansion stroke (10° ATDC), and fuel vapor is diffused in the radial and axial directions; fuel vapor convection is mainly axial because of the piston motion, although some effects of the injection eddies still persist at 10° ATDC. At 30° and 60° ATDC, the fuel vapor is concentrated near the piston for a swirl angle of 0° and between the midcylinder and the centerline for a swirl angle of 30°.

Again, more uniform fuel vapor distributions could be obtained by employing a bowled piston, because the squish (radial motion) induced during compression would create large-scale motions and recirculation zones which would tend to distribute the fuel vapor uniformly. In addition, these recirculation zones would contribute to the vaporization of the unvaporized droplets.

For a spray cone angle of 120°, the results presented in figure 36 indicate that the fuel penetration is initially independent of the swirl angle (350° ATDC) and that fuel injection creates stronger eddies for a swirl angle of 0° than for a swirl angle of 30°. The effects of swirl can be seen at 360° ATDC near the piston, where swirl results in larger radial spray penetrations. Centrifugal effects move the droplets radially along the piston, as the velocity profiles at 10°, 30°, and 60° ATDC indicate. In the absence of swirl, the droplets remain near the piston because the clockwise injection eddy moves them axially toward the piston (at 10° ATDC). The droplet locations at 30°, 60°, and 108° ATDC indicate that the spray penetration increases with the swirl angle; in the absence of swirl, unvaporized droplets remain near the piston in the clockwise injection eddy.

The turbulence kinetic energy profiles shown in figure 37 clearly indicate that the turbulence levels increase with the swirl angle. Turbulence is generated by the spray injected into the cylinder but decays in the expansion stroke, where the piston drives the flow.

The Sauter mean diameter distributions shown in figure 38 indicate that the initial spray penetration is almost independent of the intake swirl number (350° ATDC). However, as the swirl angle is increased, so is the spray penetration, particularly near the piston, as the results presented at 360°, 10°, and 30° ATDC indicate. At about 60° ATDC, most unvaporized droplets are located near the cylinder wall for a swirl angle of 30°, whereas, under no-swirl conditions, unvaporized droplets can be seen between midcylinder and the centerline, in the region occupied by the counterclockwise injection vortex.

The fuel vapor distributions are shown in figure 39 for a cone angle of 120° with and without swirl. This figure indicates that the initial fuel distribution (at 360° ATDC, i.e., 5° after the beginning of injection) is almost independent of the swirl angle. More fuel is present in the radial and axial directions at 360° ATDC for a swirl angle of 30° than for no-swirl conditions. The larger penetration of the fuel vapor in the presence of swirl can be observed at 10°, 330°, 60°, and 108° ATDC.

The results shown in this section indicate that the fuel spray penetration and vaporization are strong functions of the swirl angle and spray cone angle. More uniform fuel vapor distributions can be obtained by using a swirl angle of about 30° and a spray cone angle of about 120°; otherwise, fuel vapor remains near the piston or near the cylinder centerline. However, the results presented in this section clearly indicate that even for a cone angle at 120° and an intake swirl angle of 30°, most droplets vaporize before midcylinder and the cylinder centerline, and in an oxygen-rich region between midcylinder and the cylinder wall. These regions are a consequence of the droplet distribution function and injection velocities used in the calculations presented here. One expects that as the injection velocity and the droplet diameter are increased, larger spray penetrations can be obtained. If more uniform fuel vapor distributions are desirable for the injection characteristics used in this section, one should consider a bowled piston, where squish can be used to enhance the liquid droplet vaporization rate and the spray penetration by creating large-scale convective motions and recirculation zones within the bowl.

APPENDIX E. - DETAILED EFFECTS OF DROPLET DISTRIBUTION FUNCTION

In figures 40 to 43 the flow field, droplet locations, turbulence kinetic energy, Sauter mean diameter, and fuel vapor distributions are shown for the two droplet distribution functions presented in table II. The results presented in figures 40 to 43 correspond to 1000 rpm, a spray cone angle of 156°, and two different swirl levels: 0° swirl angle and 30° swirl angle. The droplet distribution functions are of the Rosin-Rammler type, with maximum located at 30.8 and 60 μm, whereas maximum droplet diameters are 50 and 100 μm, respectively.

The objective of using two droplet distribution functions is to determine the spray penetration and vaporization as a function of the droplet diameter for an injection angle of 15° BTDC.

The results presented in figures 40 to 43 complement those presented in previous appendixes in that for a distribution function characterized by d_{peak} = 30.8 μm and d_{max} = 50 μm, the effects of engine speed (here 1000 rpm), injection angle (here 15° ATDC), and spray cone angle (here 156°) can be compared. It should be pointed out that the calculations at 1000 rpm, spray cone angle of 156°, injection angle of 15° ATDC, d_{peak} = 30.8 μm, and d_{max} = 50 μm are presented in appendix A, in which the effects of the intake swirl angle on the flow field and spray penetration and vaporization are investigated. The results of these calculations at 1000 rpm are repeated here in order to clearly indicate the effects of the droplet distribution function on spray penetration and vaporization.

Figures 40 to 43 show gas-phase velocities, droplet locations, Sauter mean diameters, turbulence, and fuel vapor mass fractions at selected crankshaft angles for the two distribution functions analyzed in this report (see table II) and for intake swirl angles 0° and 30°.

Figure 40 clearly indicates that for the bigger droplet distribution, the droplets essentially move along a trajectory which forms 78° with the cylinder centerline, except for some amount of lateral dispersion. Figure 40 also shows that very droplets are entrained by the injection-generated eddies. Only by about 30° ATDC does the clockwise injection eddy entrain some small droplets. In contrast, for the smaller distribution function, the droplets move along the cylinder head and are entrained by the clockwise-rotating injection eddy, which is stretched in both axial and radial directions (30° ATDC). By about 60° ATDC few unvaporized droplets remained in the cylinder, whereas at the same crankshaft angle many unvaporized droplets can be observed in the cylinder for the larger distribution function. This is a consequence of the vaporization cooling and the diameter of the droplets (small surface-area-to-volume ratio).

The turbulence levels shown in figure 41 indicate that turbulence kinetic energy is generated by the spray near the injector. Turbulence is also generated at the edge of the spray as it penetrates into the cylinder. However, this generation is smaller than the background levels and is quickly convected, diffused, and dissipated.

Figure 42 clearly indicates that the larger distribution function results in larger Sauter mean diameters throughout the engine cylinder and in larger spray penetration (350° ADTC). At 360° ATDC for the larger distribution function, the droplets are traveling along a straight line, whereas for the smaller distribution function, the droplets are entrained by the clockwise injection vortex. Similar results can be observed at 10°, 30°, and 60° ATDC. Note that at 60° ATDC, most unvaporized droplets are located near the cold cylinder wall. These droplets represent a small fraction of the total amount of the fuel injected into the cylinder.

The fuel vapor distributions for the two droplet functions analyzed in this study are presented in figure 43. Note that the smaller distribution function results in faster vaporization than that corresponding to d_{peak} = 60 μm because the smaller droplets have a high surface-area-to-volume ratio and vaporize faster (350° ATDC). At 360° ATDC, similar trends are shown, indicating that the smaller droplets are quickly vaporized near the injector, whereas the larger droplets penetrate farther into the cylinder. Similar trends are shown at 30° and 60° ATDC. Note, however, that the larger droplet distribution results in a more uniform fuel vapor distribution throughout the cylinder, whereas for the smaller distribution, most vapor is concentrated near the centerline and the cylinder head. Thus, in order to achieve more uniform fuel vapor distributions, larger droplets should be used. There is, however, a limit. If the droplets are too big, they will remain unvaporized near the cold cylinder wall. Note that large droplets preserve their linear momentum farther and are not vaporized as quickly as small droplets.

The effects of swirl and droplet distribution function on the flow field and spray penetration and vaporization are also shown in figures 40 to 43.

Figure 40 shows the complex flow patterns induced by swirl. They spray penetration is essentially not affected by swirl at the beginning of the injection process (350° ATDC). At 360° ATDC, the spray tip has already been deflected radially toward the cylinder wall by centrifugal effects. The deflection and fuel vaporization increase with the crankshaft angle, as the results shown at 10° and 30° ATDC indicate. Note that in the presence of swirl, many large droplets have already reached the piston at 30° ATDC, whereas in the absence of swirl, unvaporized droplets are located in midcylinder. Most unvaporized droplets for a swirl angle of 30° are located at the cold cylinder wall, where they vaporize slowly if at all. At 108° ATDC, unvaporized droplets can be seen at the cylinder wall and midcylinder for intake swirl angles of 0° and 30°, respectively.

Figure 41 clearly indicates that swirl results in more turbulence kinetic energy and that the spray injection generates turbulence near the injector. This turbulence is rapidly diffused and decays in the expansion stroke. Figure 42 shows that the initial penetration of the spray and the Sauter mean diameter distributions are almost insensitive to the intake swirl angle (350° ATDC). At TDC (360° ATDC), the radial deflection of the spray tip toward the cylinder centerline is clearly shown. It seems that swirl "throws" the larger droplets toward the cylinder wall, where they still continue moving along a 78° line with respect to the cylinder centerline (156° spray cone angle). This is illustrated in figure 42 at 10° and 30° ATDC. At 60° ATDC, the smaller droplet distribution results in unvaporized droplets between midcylinder and the cylinder wall, whereas for the larger distribution, unvaporized droplets are located in a localized zone at the cold cylinder wall.

The results shown in figure 42 clearly indicate that spray penetration and vaporization are strong functions of intake swirl and droplet size.

The fuel vapor distributions shown in figure 42 indicate that the initial fuel vaporization is almost independent of the intake swirl angle because the droplets are injected near the cylinder centerline, where the azimuthal velocity is zero (350° ATDC). Some differences in the fuel vapor distributions at 360° ATDC are shown in figure 42. (Note the change in scale at 360° and 10° ATDC.) The radial penetration of the fuel vapor can be observed at 10° and at 30° ATDC. At the latter angle and for the larger droplet distribution, fuel vapor is already present at the cylinder wall in the presence of swirl; however, for a swirl angle of 0°, little (if any) fuel vapor has reached the wall. Similar results are shown at 60° ATDC, where some vaporization can be observed near the cold cylinder wall.

The fuel penetration results presented in figure 42 clearly indicate that a distribution function with d_{max} = 100 μm and a swirl angle of 30° yields reasonably good and uniform fuel vapor distributions throughout the cylinder. Further fuel vapor uniformity can be achieved by using a bowled piston, which creates squish and recirculation zones. These zones contribute to fuel vaporization and mixing.

REFERENCES

1. Hiroyasu, H.; and Kadota, T.: Fuel Droplet Size Distribution in Diesel Combustion Chamber. SAE Paper 740715, 1974.

2. Dukowicz, J.K.: A Particle-Fluid Numerical Model for Liquid Sprays. J. Comput. Phys., vol. 35, no. 2, Apr. 1980, pp. 229-253.

3. O'Rourke, P.J.; and Bracco, F.V.: Modeling of Drop Interactions in Thick Sprays and a Comparison with Experiments. Stratified Charge Automotive Engines, Mechanical Engineering Publications, London, 1980, pp. 101-116.

4. Wu, K.-J.; Reitz, R.D.; and Bracco, F.V.: Measurements of Drop Size at the Spray Edge Near the Nozzle in Atomizing Liquid Jets. Phys. Fluids, vol. 29, no. 4, Apr. 1986, pp. 941-951.

5. Wu, K.-J., et al.: Measurements of the Spray Angle of Atomizing Jets. J. Fluids Eng., vol. 105, no. 4, Dec. 1983, pp. 406-413.

6. Kuo, T.-W.; and Bracco, F.V.: Computations of Drop Sizes in Pulsating Sprays and of Liquid-Core Length in Vaporizing Sprays. SAE Paper 820133, 1982.

7. Kuo, T.-W.; and Bracco, F.V.: On the Scaling of Transient Laminar, Turbulent, and Spray Jets. SAE Paper 820038, 1982.

8. Kuo, T.-W.; and Yu, R.C.: Modeling of Transient Evaporating Spray Mixing Processes - Effect of Injection Characteristics. SAE Paper 840226, 1984.

9. Amsden, A.A., et al.: KIVA: A comprehensive Model for 2-D and 3-D Engine Simulations. SAE Paper 850554, 1985.

10. Duggal, V.K., et al.: Three-Dimensional Modeling of In-Cylinder Processes in DI Diesel Engines. SAE Paper 840227, 1984.

11. Reitz, R.D.; and Diwakar, R.: Effect of Drop Breakup on Sprays. SAE Paper 660469, 1986.

12. Awn, A.G.; and Spalding, D.B.: Fluid Flow Within Reciprocating Engine Cylinder. Numerical Methods in Thermal Problems, Vol.2, R.W. Lewis, K. Morgan and B.A. Schreffler, eds., Pineridge Press, Swanstea, UK, 1981, pp. 1189-1203.

13. Sher, E.: A New Practical Model for the Scavenging Process in a Two-Stroke Cycle Engine. SAE Paper 850085, 1985.

14. Sher, E.: Prediction of the Gas Exchange Performance in a Two-Stroke Cycle Engine. SAE Paper 850086, 1985.

15. Sher, E.: Investigating the Gas Exchange Process of a 2-Stroke Cycle Engine with a Flow Visualization Rig. Inr. J. Technol., vol. 20, no. 3, 1982, pp. 127-136.

16. Adachi, T.; Kato, S.; and Tsujimura, H.: Numerical-Analysis of Scavenging Flow in 2-Cycle Internal-Combustion Engines. Flows in Internal Combustion Engines, T. Uzkan, ed., ASME, 1982, pp. 29-34.

17. Diwakar, R.: Multi-dimensional Modeling of the Gas Exchange Processes in a Uniflow-Scavenged Two-Stroke Diesel Engine. International Symposium on Flows in Internal Combustion Engines - III, ASME FED Vol 28, T. Uzkan, W.G. Tiederman and J.M. Novak, eds., ASME, 1985, pp. 125-134.

18. Carpenter, M.H.; and Ramos, J.I.: The Numerical Solution of the Flowfield in an Internal Combustion Engine. Advances in Computer Methods for Partial Differential Equations - V.R. Vichnevetsky and R.S. Stepleman, eds., IMACS, New Brunswick, NJ, 1984, pp. 24-31.

19. Carpenter, M.H.; and Ramos, J.I.: Modelling of a Gasoline-Injected Two-Stroke Cycle Engine. SAE Paper 860167, 1986.

20. Uzkan, T.; and Hazelton, J.R.: The Influence of Swirl on the Fresh Charge Stratification in an IC Engine Combustion Chamber. SAE Paper 860466, 1986.

21. Kuo, T.-W.; and Yu, R.C.: Modeling of Transient Evaporating Spray Mixing Processes - Effect of Injection Characteristics. SAE Paper 840226, 1984.

22. Gosman, A.D.; and Johns, R.J.R.: Computer Analysis of Fuel-Air Mixing in Direct-Injection Engines. Diesel Combustion and Emissions, SAE P-86, SAE, 1980, pp. 75-90.

23. Gosman, A.D.; and Harvey, P.S.: Computer Analysis of Fuel-Air Mixing and Combustion in an Axisymmetric D.I. Diesel. SAE Paper 820036, 1982.

24. Carpenter, M.H.; and Ramos, J.I.: Modeling of a Gasoline-Injected Two-Stroke Cycle Engine. SAE Paper 860167, 1986.

25. Ramos, J.I.; Humphrey, J.A.C.; and Sirignano, W.A.: Numerical Prediction of Axisymmetric, Laminary and Turbulent Flows in Motored, Reciprocating Internal Combustion Engines. SAE Transactions, Vol. 88, 1980, pp. 1217-1242.

26. Carpenter, M.H.: A Numerical Study of the Direct Injection Diesel Engine Under Motored and Firing Conditions. Ph.D. Thesis, Carnegie-Mellon University, Pittsburgh, PA, 1986.

27. Bracco, F.V.: Modelling of Engine Sprays. SAE Paper 850394, 1985.

28. Reitz, R.D.; and Bracco, F.V.: Mechanism of Atomization of a Liquid Jet. Phys. Fluids, vol. 25, no. 10, Oct. 1982, pp. 1730-1742.

29. Wu, K.-J.; Reitz, R.D.; and Bracco, F.V.: Measurements of Drop Size at the Spray Edge Near the Nozzle in Atomizing Liquid Jets. Phys. Fluids, vol. 29, no. 4, Apr. 1986, pp. 941-951.

30. Ramos, J.I.; and Sirignano, W.A.: Axisymmetric Flow Model in a Piston-Cylinder Arrangement with Detailed Analysis of the Valve Region. SAE Paper 800286, 1980.

31. Body, D.B.: Drop Formation in a Circular Liquid Jet. Annual Review of Fluid Mechanics, Vol. 11, Annual Reviews Inc., 1979, pp. 207-228.

32. McCarthy, M.J.; and Molloy, N.A.: Review of Stability of Liquid Jets and the Influence of Nozzle Design. Chem. Eng. J., vol. 7, no. 1, Feb. 1974, pp. 1-20.

33. Shimizu, I., et al.: A Light Scattering and Holographic Technique for Determining Droplet Size and Volume Density Distribution in Diesel Fuel Sprays. Diesel Engine Combustion, Emissions, and Particulates, SAE P-107, SAE, 1982, pp. 155-164.

34. Hiroyasu, H.; Shimizu, M.; and Arai, M.: The Breakup of High Speed Jet in a High Pressure Gaseous Atmosphere. Reports and Proceedings of the Second International Conference on Liquid Atomization and Spray Systems. (ICLASS-82), University of Wisconsin, Madison, WI, 1982.

35. Chehroudi, B., et al.: On the Intact Core of Full-Cone Sprays. SAE Paper 850126, 1985.

TABLE I. - GEOMETRY OF THE TWO-STROKE DIESEL ENGINE

[All dimensions in centimeters.]

Bore	7.67
Cylinder radius	3.835
Crankshaft radius	7.50
Clearance	0.50
Connecting rod length	20.0
Exhaust valve diameter	1.57
Exhaust valve opening distance	0.733
Intake port opening	7.58
Intake port closing	7.95

TABLE II. - ENGINE VARIABLES INVESTIGATED IN THIS STUDY

Speed, rpm	Swirl angle, deg	Spray angle, deg	Injection angle, deg ATDC	Peak of distribution function, d_{peak}, mm	Maximum droplet diameter, d_{max}, mm
1000	0	10	345	30.8	50
	↓	30	345	↓	↓
	↓	60	345	↓	↓
	↓	78	315	↓	↓
	↓	↓	330	↓	↓
	↓	↓	345	↓	↓
	↓	↓	↓		
		↓	↓	60	100
	11.25	↓	↓	30.8	50
	22.5		↓	↓	↓
	30	10	↓	↓	↓
	↓	30	↓	↓	↓
	↓	60		↓	↓
	↓	78	315	↓	↓
	↓	↓	330	↓	↓
	↓	↓	345		
		↓	345	60	100
	45	↓	345	30.8	50
1500	0	78	345	30.8	50
	30	78	345	30.8	50
2000	0	78	345	30.8	50
	30	78	345	30.8	50

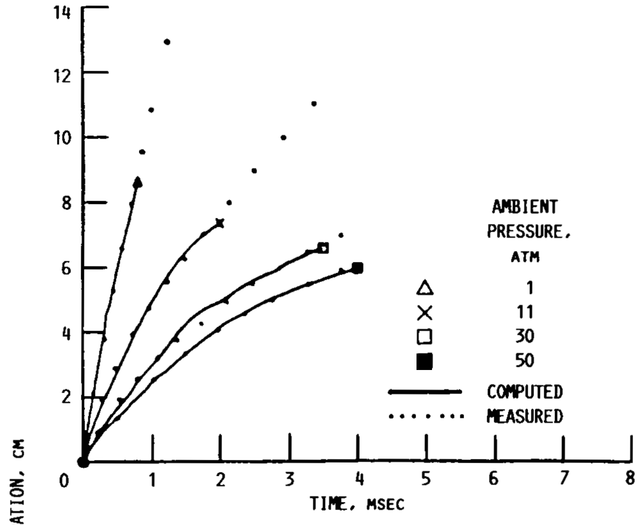

(A) COMPARISONS BETWEEN COMPUTED SPRAY PENETRATION AND THAT MEASURED BY HIROYASU AND KADOTA (REF. 1).

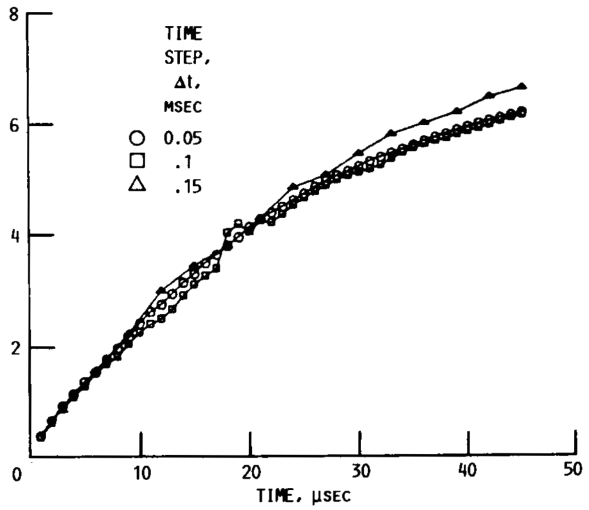

(B) EFFECT OF TIME STEP ON SPRAY PENETRATION AT 50 ATM.

FIGURE 1. - SPRAY PENETRATION RESULTS.

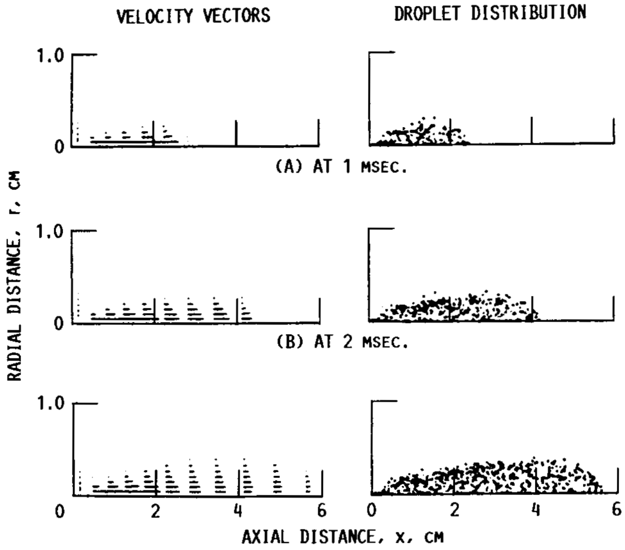

(A) AT 1 MSEC.

(B) AT 2 MSEC.

(C) AT 3.5 MSEC.

FIGURE 2. - GAS-PHASE VELOCITY VECTORS AND SPRAY LOCATION AT DIFFERENT TIMES FOR AMBIENT PRESSURE OF 50 ATM.

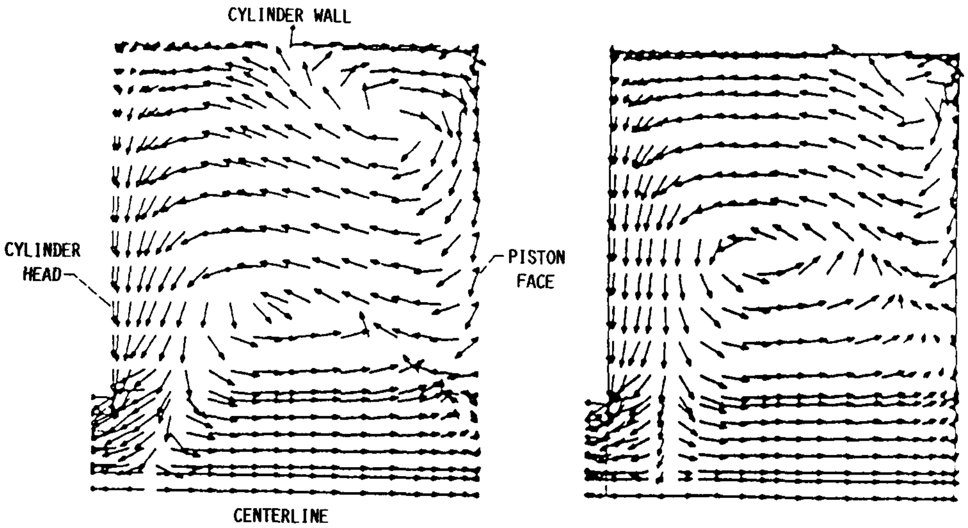

(A) SWIRL ANGLE, 0°.

(B) SWIRL ANGLE, 22.5°.

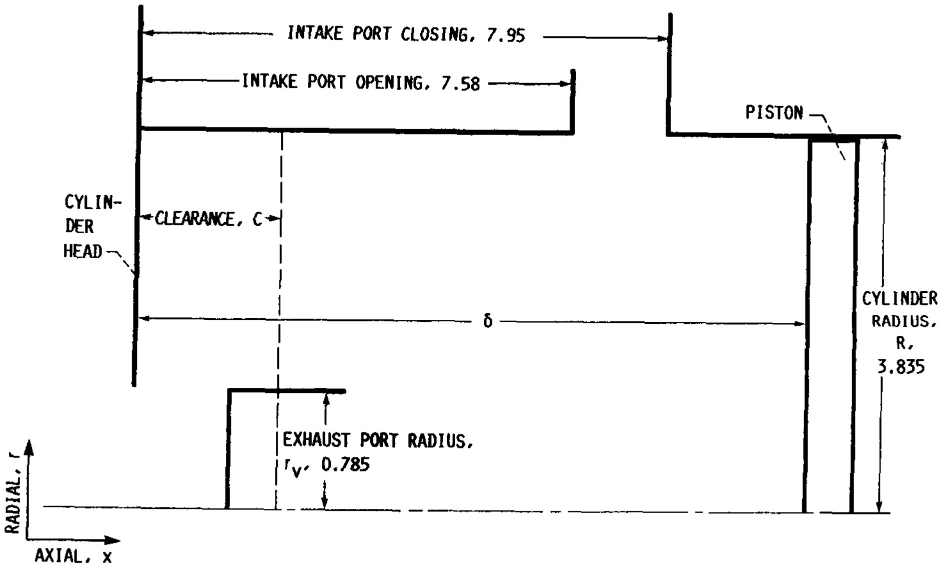

(C) GEOMETRY OF DIESEL ENGINE CHAMBER WITH TWO-DIMENSIONAL COORDINATE SYSTEM (ALL DIMENSIONS IN CENTIMETERS).

FIGURE 3. - GAS-PHASE VELOCITY VECTOR PROFILES FOR SWIRL ANGLES OF 0° AND 22.5° AT 200° ATDC, AND GEOMETRY OF DIESEL ENGINE CHAMBER.

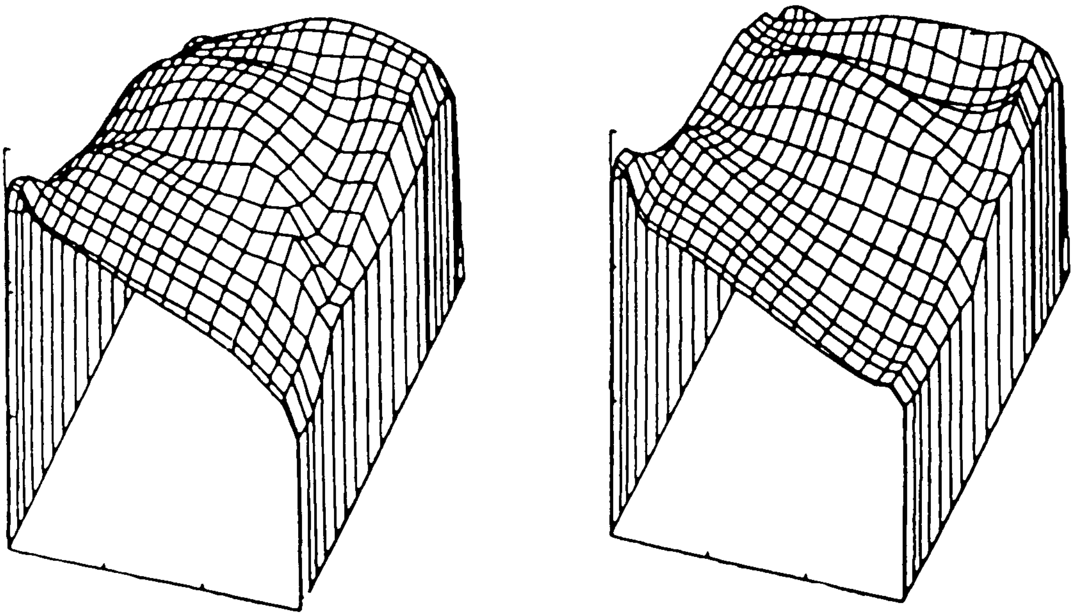

(A) SWIRL ANGLE, 0°.

(B) SWIRL ANGLE, 22.5°.

FIGURE 4. - NATURAL LOGARITHM OF TURBULENCE KINETIC ENERGY FOR SWIRL ANGLES OF 0° AND 22.5°.

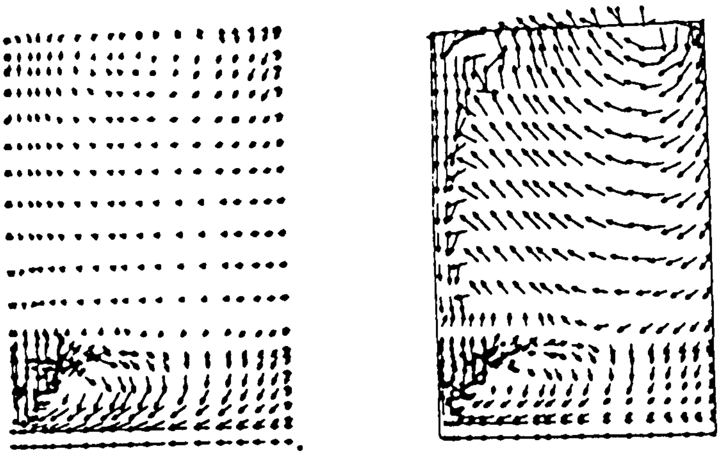

(A) SWIRL ANGLE, 0°.

(B) SWIRL ANGLE, 22.5°.

FIGURE 5. - GAS-PHASE VELOCITY VECTOR PROFILES AND DROPLET LOCATIONS FOR SWIRL ANGLES OF 0° AND 22.5° AT 350° ATDC.

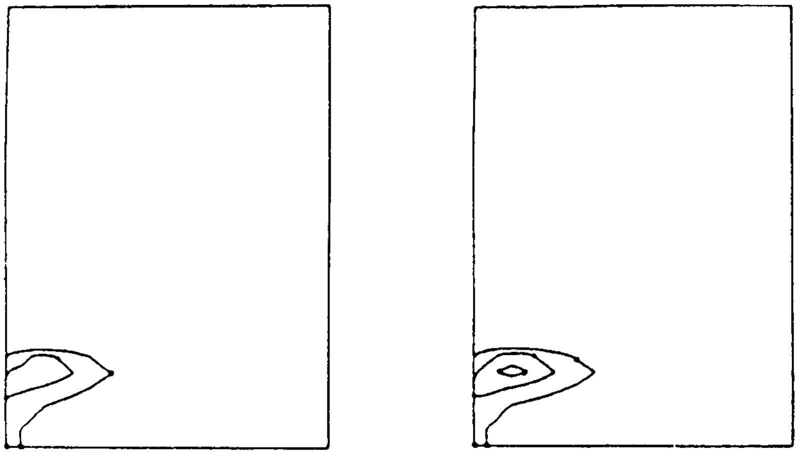

(A) SWIRL ANGLE, 0^0.

(B) SWIRL ANGLE, 22.5^0.

FIGURE 6. - FUEL MASS FRACTION DISTRIBUTIONS FOR SWIRL ANGLES OF 0^0 AND 22.5^0 AT 350^0 ATDC.

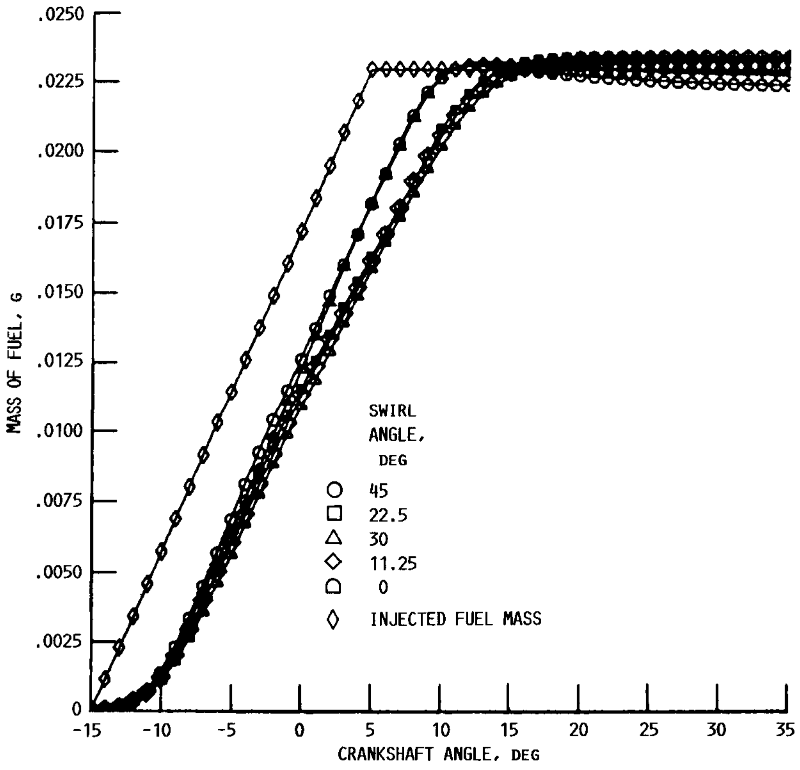

FIGURE 7. - MASS OF FUEL VAPOR AS FUNCTION OF CRANKSHAFT ANGLE FOR DIFFERENT SWIRL ANGLES.

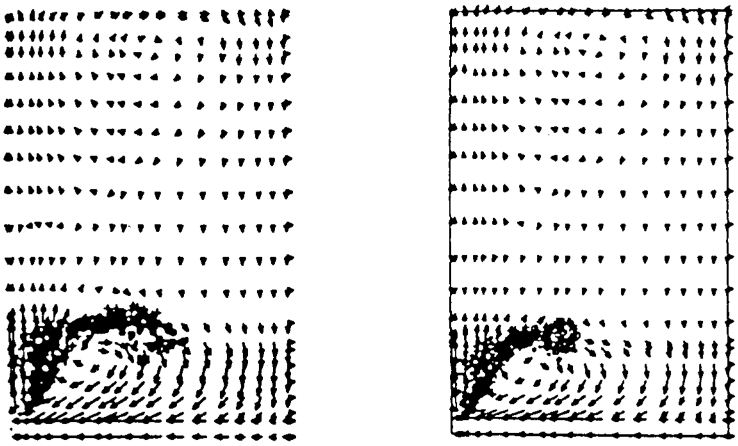

(A) ENGINE SPEED, 1500 RPM.

(B) ENGINE SPEED, 2000 RPM.

FIGURE 8. - GAS-PHASE VELOCITY VECTOR PROFILES AND DROPLET LOCATIONS FOR ENGINE SPEEDS OF 1500 AND 2000 RPM AT 360° ATDC FOR 0° SWIRL ANGLE.

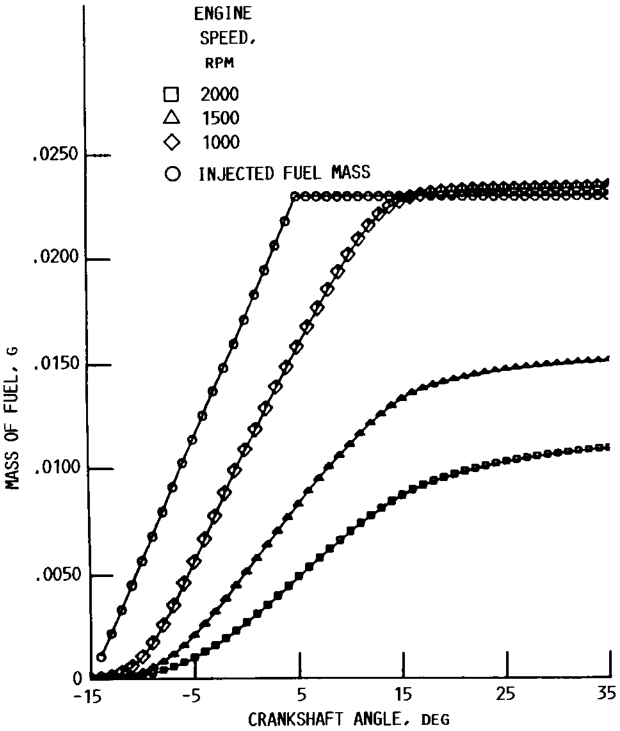

FIGURE 9. - VAPORIZATION RATE AS FUNCTION OF ENGINE SPEED AND CRANKSHAFT ANGLE.

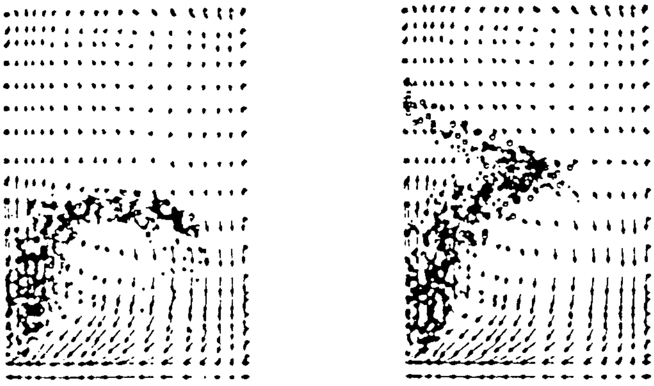

(A) INJECTION ANGLE, 45° BTDC.

(B) INJECTION ANGLE, 30° BTDC.

FIGURE 10. - GAS-PHASE VELOCITY VECTOR PROFILES AND DROPLET LOCATIONS FOR INJECTION ANGLES OF 45° AND 30° BTDC AT 360° ATDC FOR 0° SWIRL ANGLE.

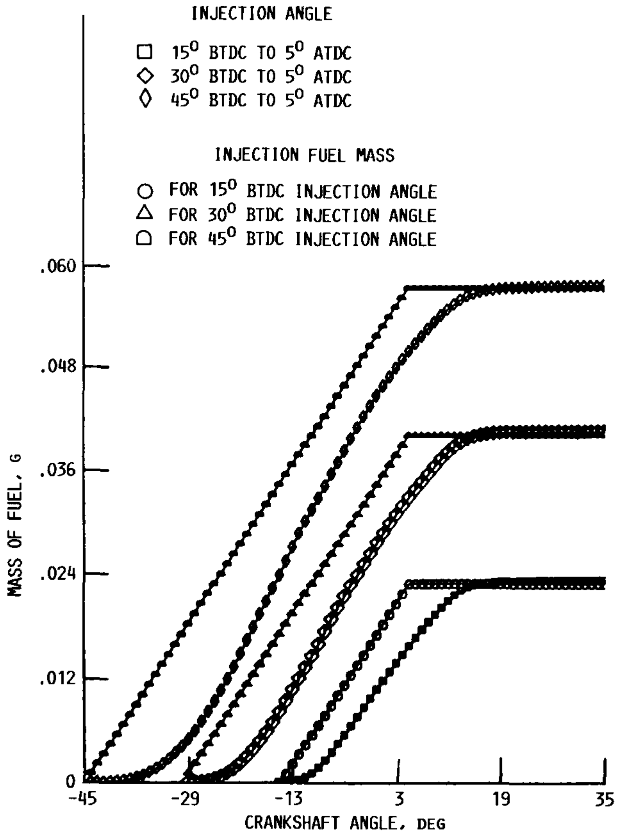

FIGURE 11. - VAPORIZATION RATE AS FUNCTION OF INJECTION ANGLE AND CRANKSHAFT ANGLE.

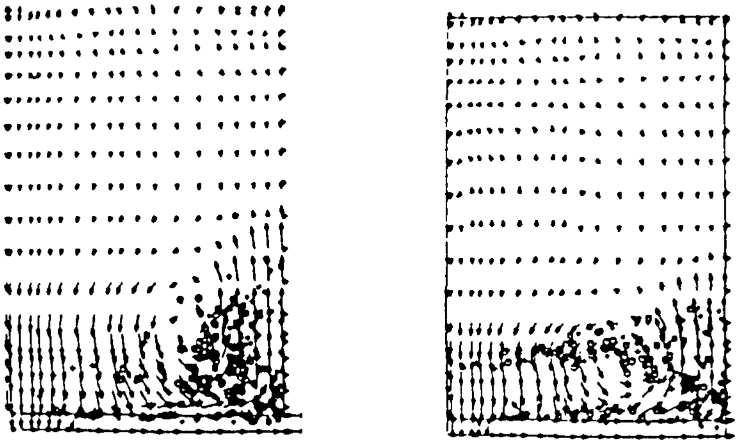

(A) SPRAY CONE ANGLE, 20°.

(B) SPRAY CONE ANGLE, 60°.

FIGURE 12. - GAS-PHASE VELOCITY VECTOR PROFILES AND DROPLET LOCATIONS FOR SPRAY CONE ANGLES OF 20° AND 60° AT 360° ATDC FOR 0° SWIRL ANGLE.

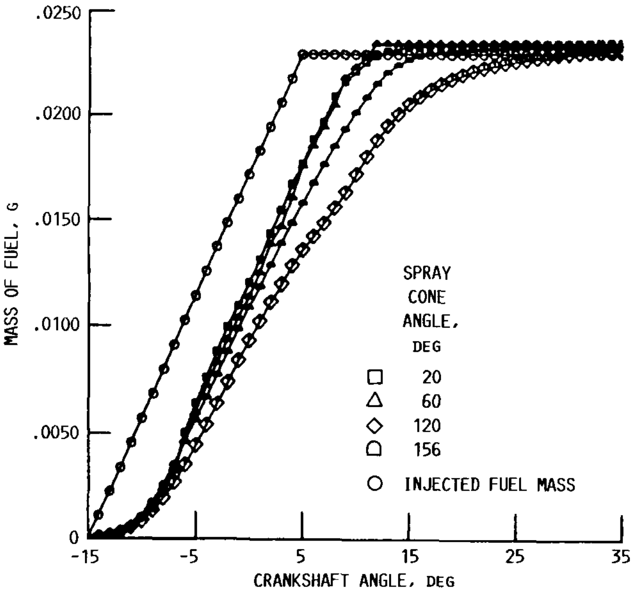

FIGURE 13. - VAPORIZATION RATE AS FUNCTION OF SPRAY CONE ANGLE AND CRANKSHAFT ANGLE.

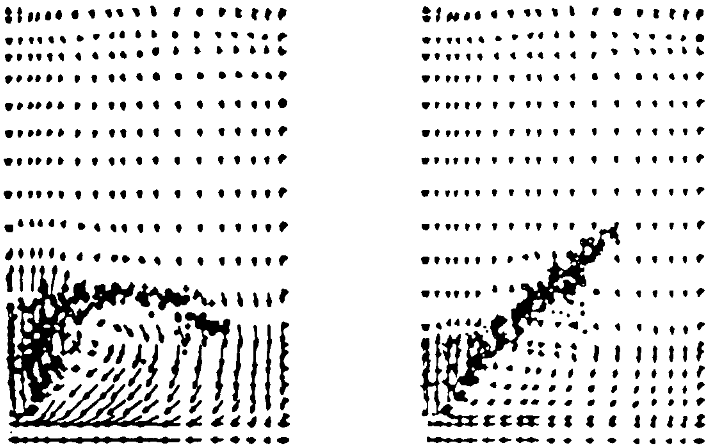

(A) PEAK OF DISTRIBUTION FUNCTION d_{peak}, 30.8 μM AND MAXIMUM DROPLET DIAMETER d_{max}, 50 μM.

(B) PEAK OF DISTRIBUTION FUNCTION d_{peak}, 60 μM AND MAXIMUM DROPLET DIAMETER d_{max}, 100 μM.

FIGURE 14. - GAS-PHASE VELOCITY VECTOR PROFILES AND DROPLET LOCATIONS FOR THE TWO DROPLET DISTRIBUTION FUNCTIONS SHOWN IN TABLE II AT 360° ATDC FOR 0° SWIRL ANGLE.

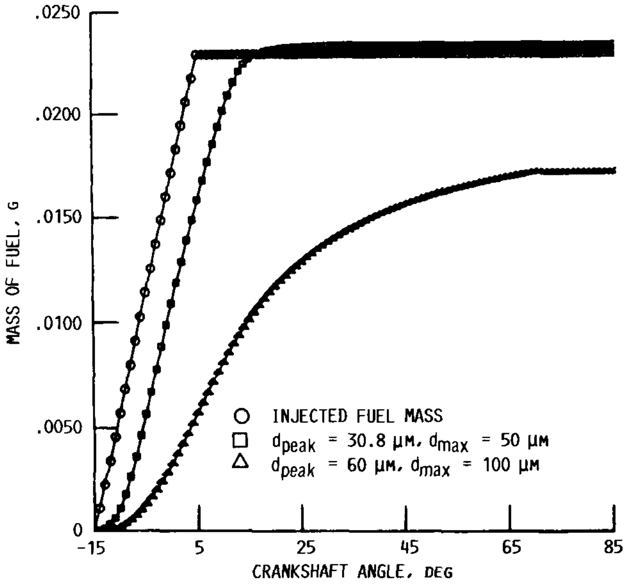

FIGURE 15. - VAPORIZATION RATE AS FUNCTION OF DROPLET DISTRIBUTION FUNCTION AND CRANKSHAFT ANGLE.

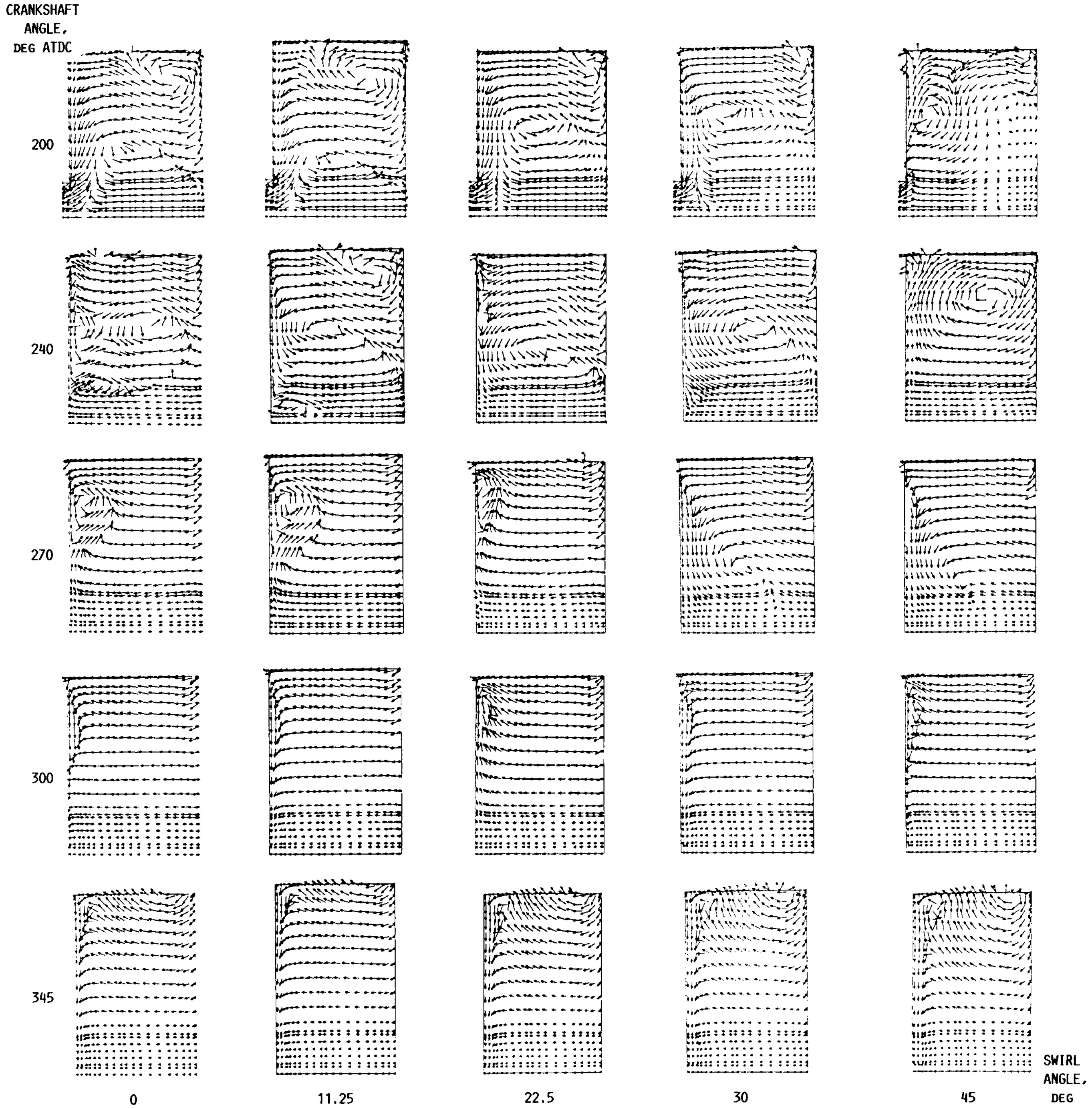

FIGURE 16. - GAS-PHASE VECTORS AS FUNCTION OF SWIRL ANGLE.

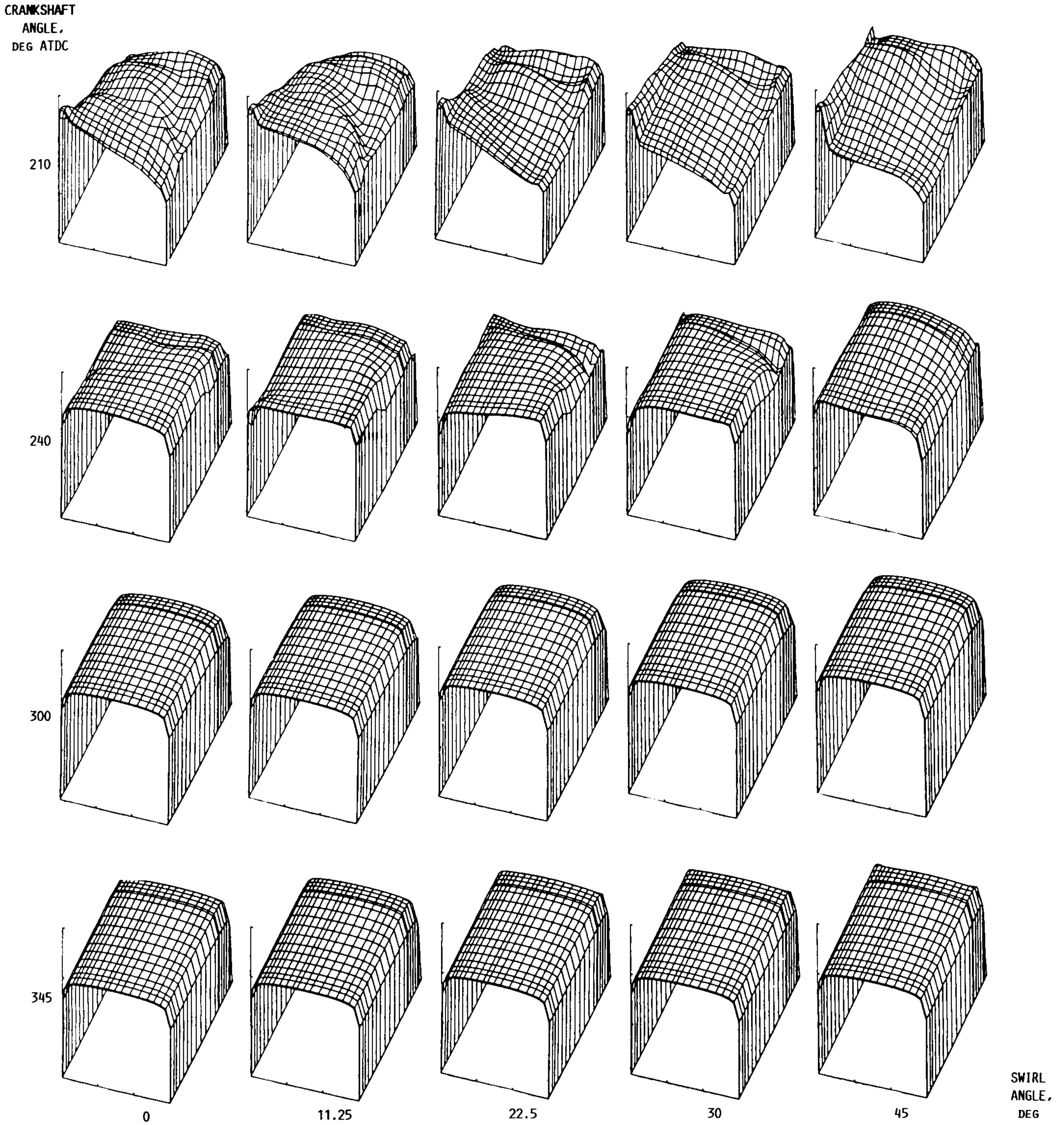

FIGURE 17. - NATURAL LOGARITHM OF TURBULENCE KINETIC ENERGY PROFILES AS FUNCTION OF SWIRL ANGLE.

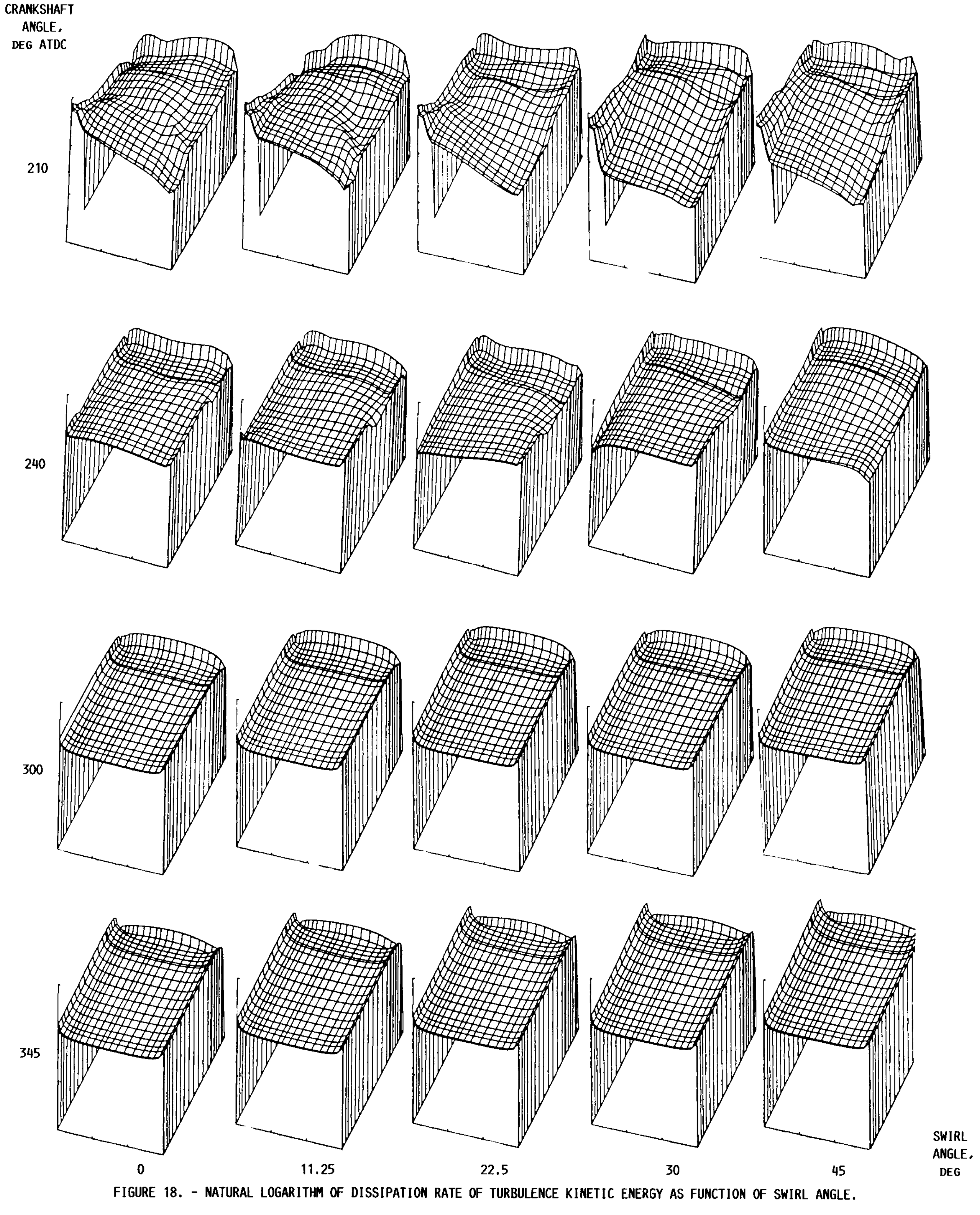

FIGURE 18. - NATURAL LOGARITHM OF DISSIPATION RATE OF TURBULENCE KINETIC ENERGY AS FUNCTION OF SWIRL ANGLE.

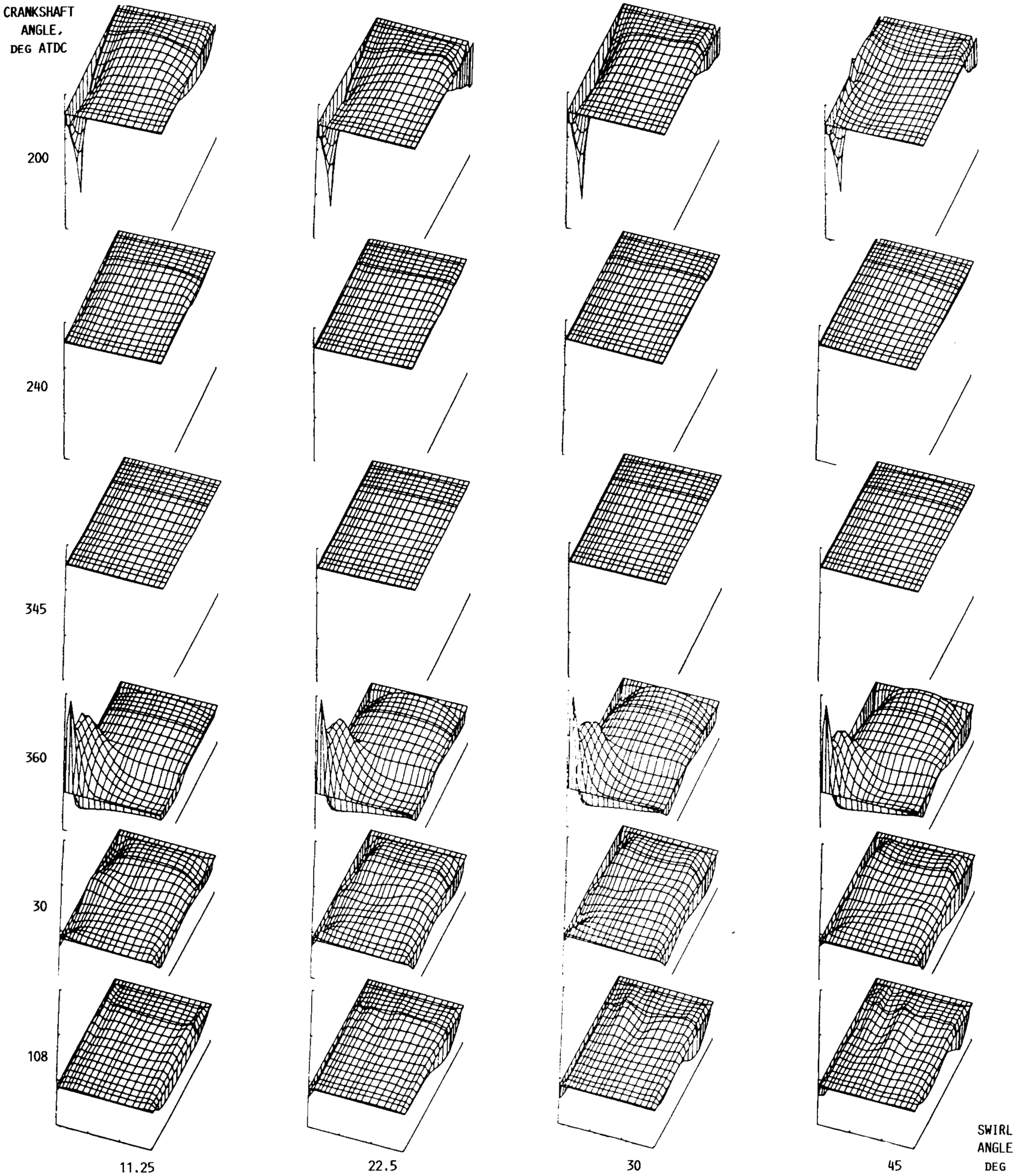

FIGURE 19. - AZIMUTHAL VELOCITY PROFILES FOR DIFFERENT SWIRL ANGLES. (THE SCALE FOR THE AZIMUTHAL VELOCITY AT 200°, 240°, AND 345° IS FROM -20 000 TO 3999 CM/SEC, AND AT 360°, 30°, AND 108° IS FROM -700 TO 1800 CM/SEC.)

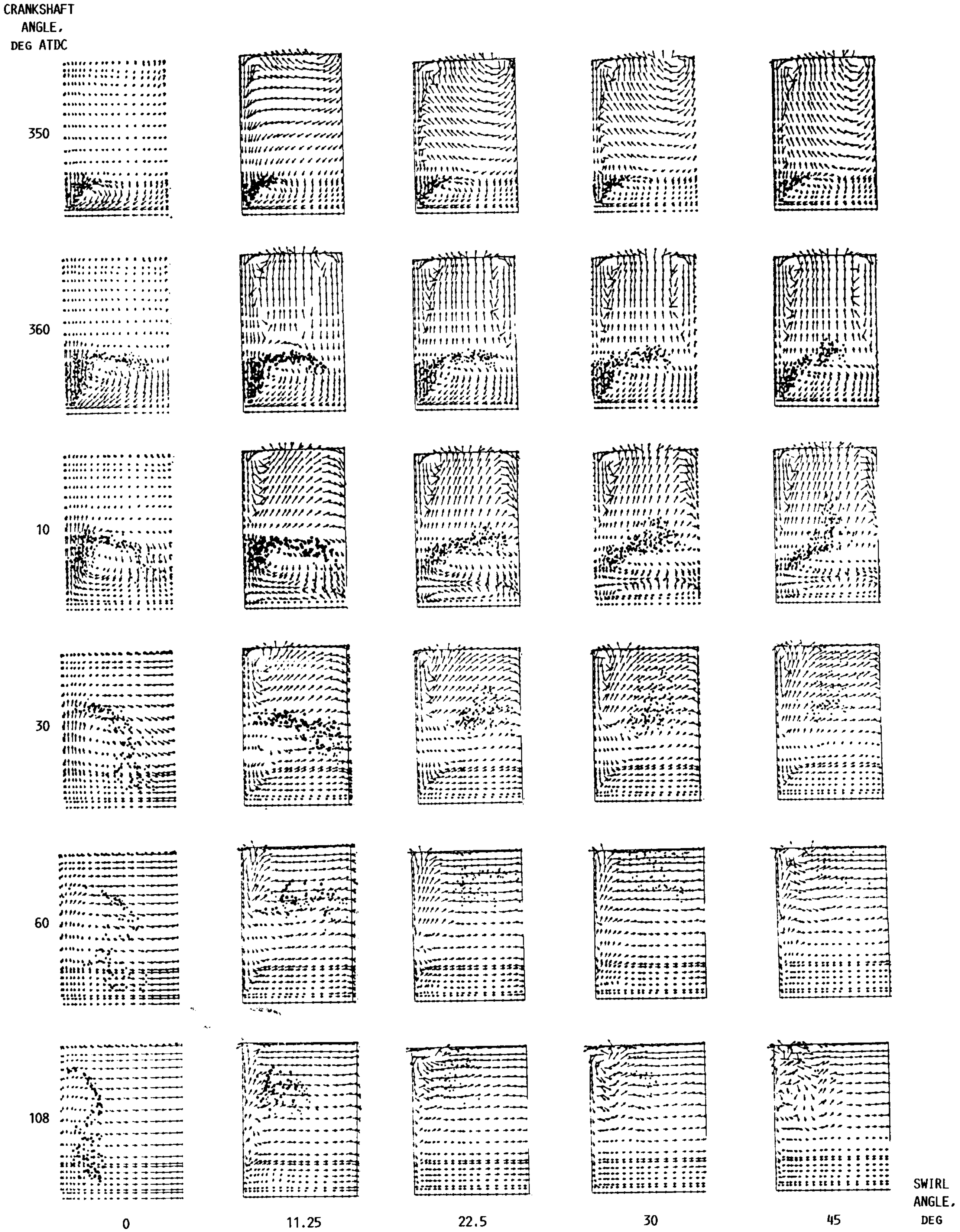

FIGURE 20. - GAS-PHASE VELOCITY VECTORS AND DROPLET LOCATIONS AS FUNCTION OF SWIRL ANGLE.

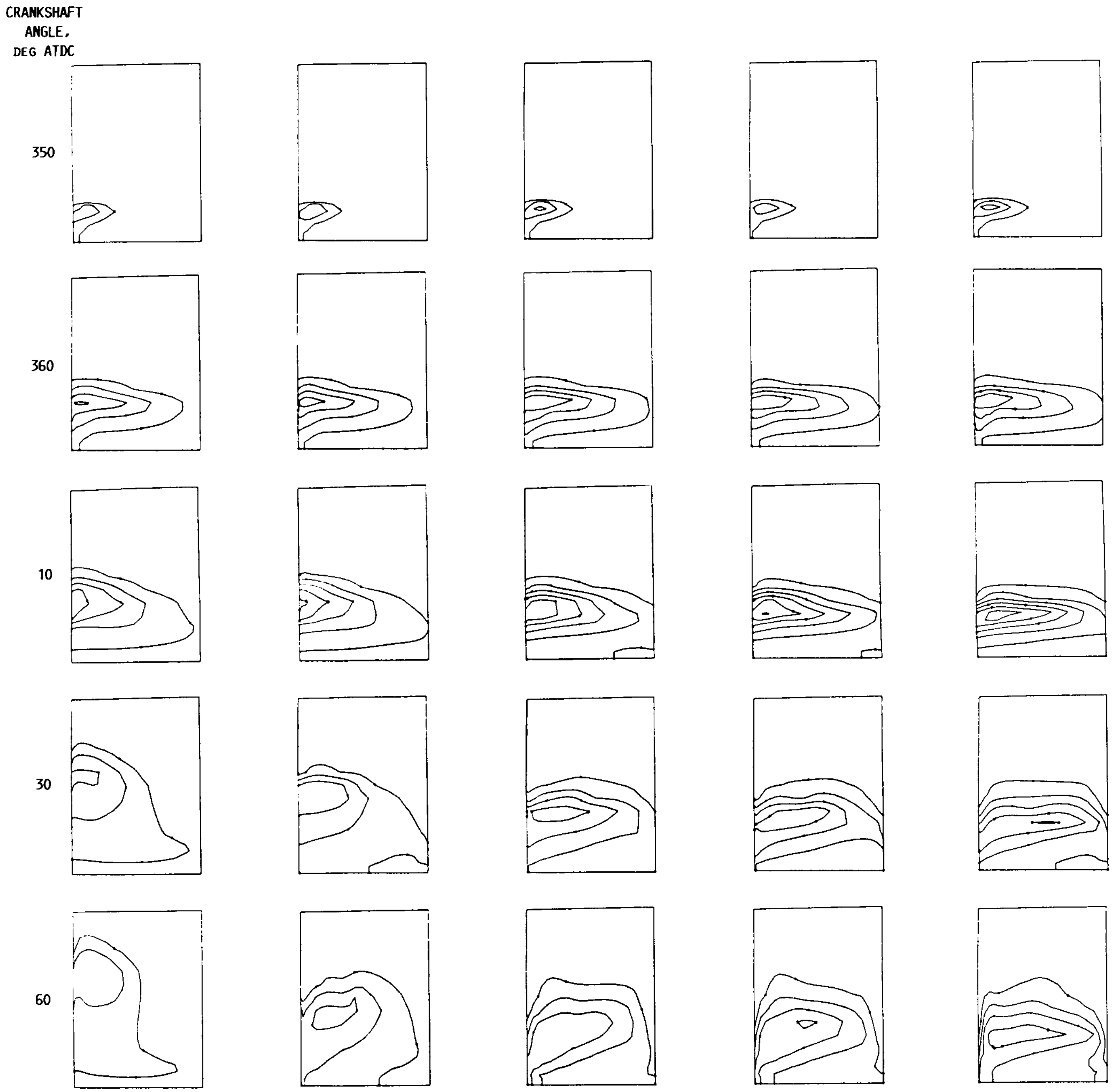

(A) FUEL MASS FRACTION DISTRIBUTION.

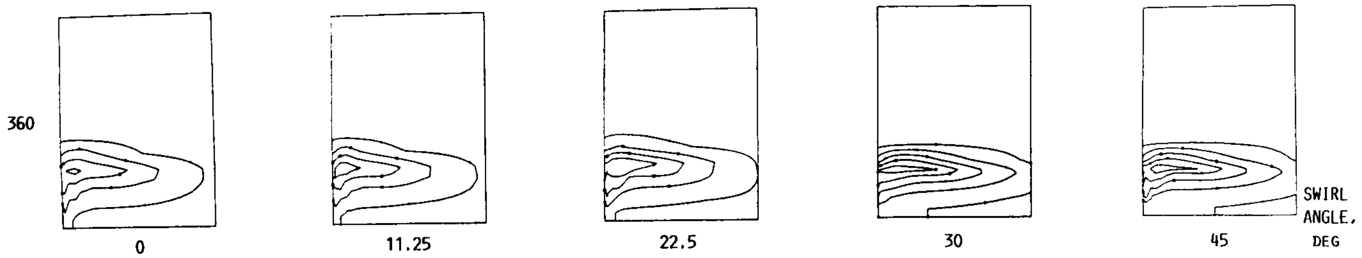

(B) OXYGEN MASS FRACTION DISTRIBUTION.

FIGURE 21. - FUEL MASS FRACTION DISTRIBUTIONS AT 350°, 360°, 10°, 30°, AND 60° ATDC, AND OXYGEN MASS FRACTION DISTRIBUTION AT 360° ATDC AS FUNCTION OF SWIRL ANGLE.

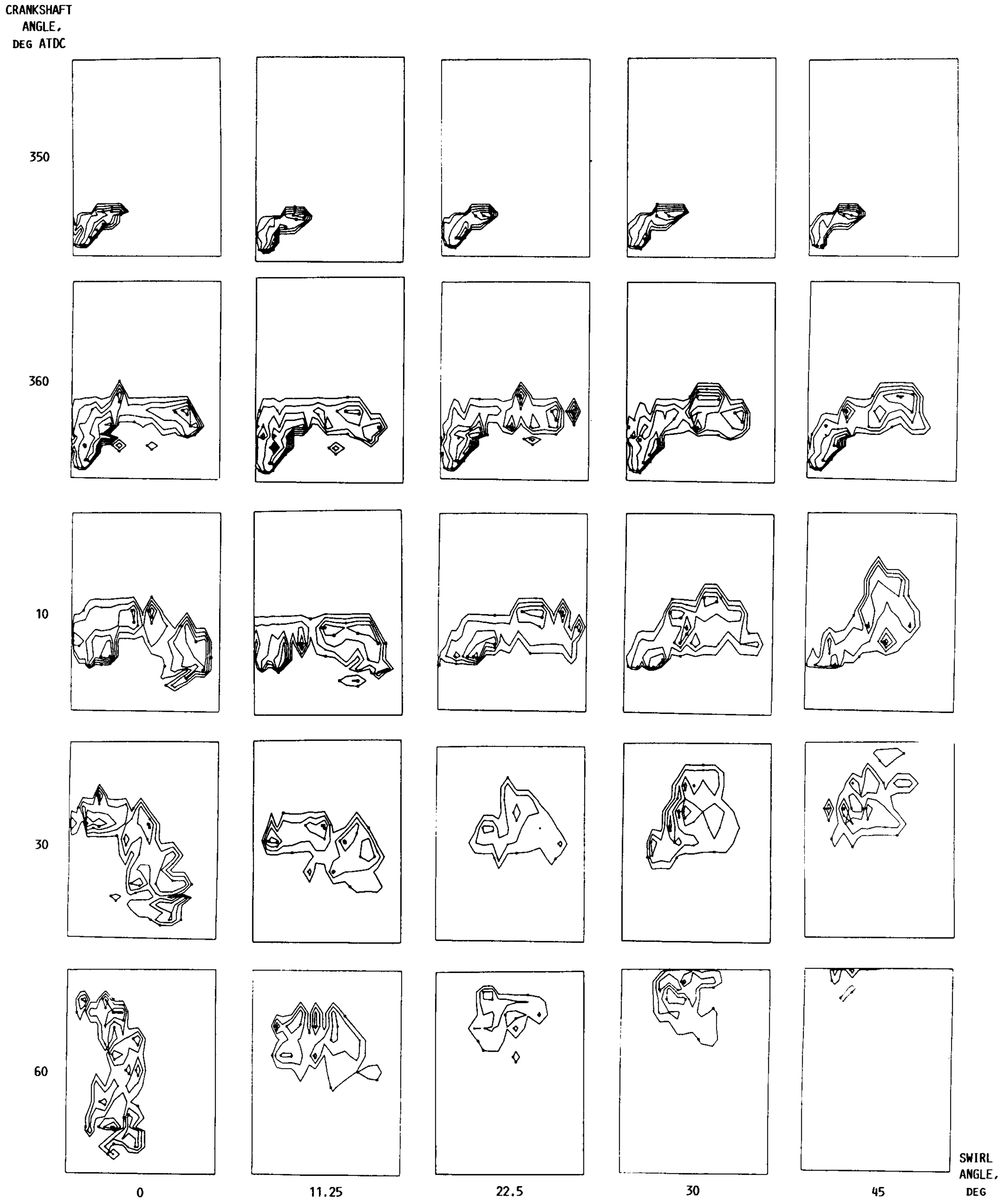

FIGURE 22. - SAUTER MEAN DIAMETER DISTRIBUTIONS AS FUNCTION OF SWIRL ANGLE.

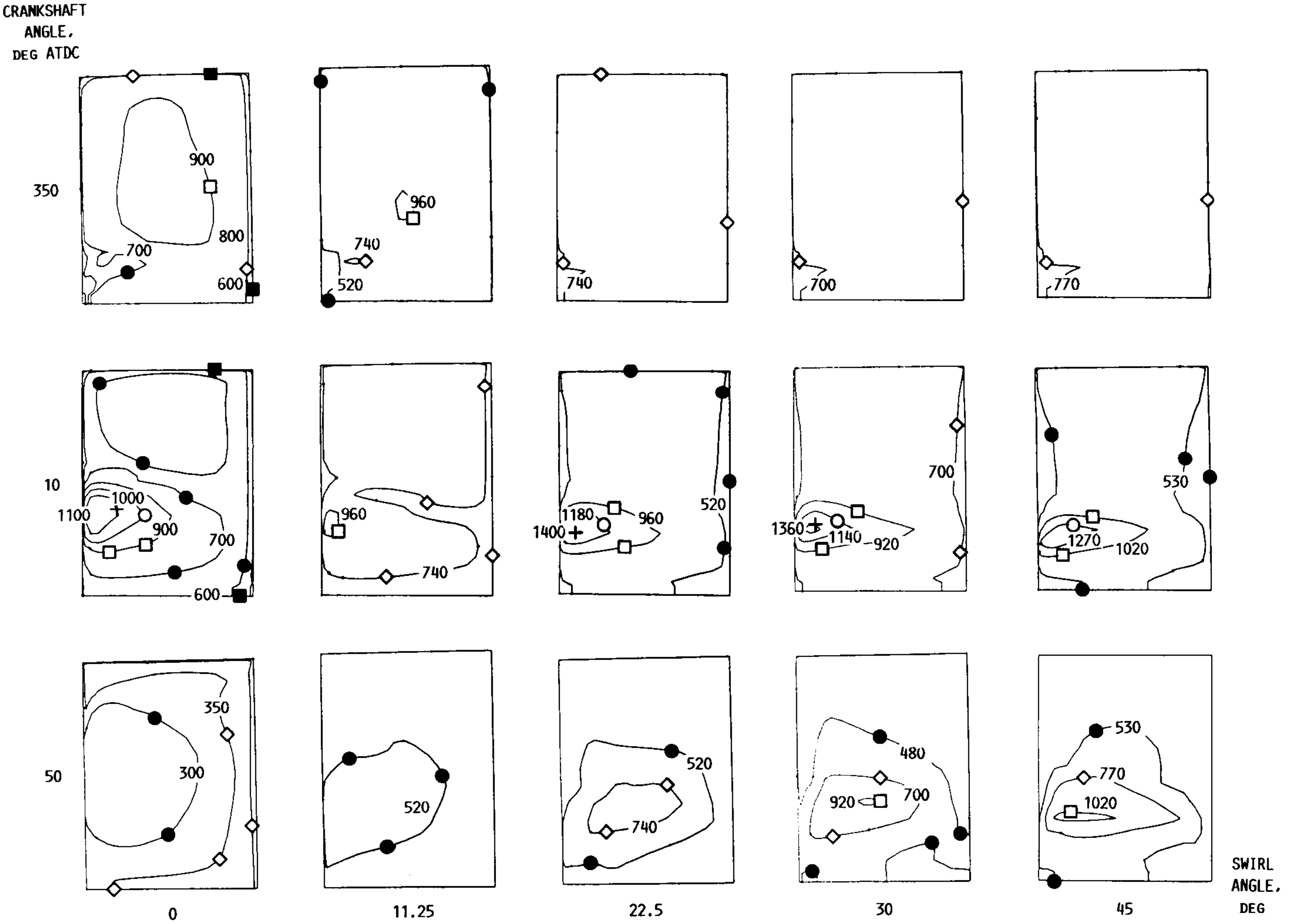

FIGURE 23. - TEMPERATURE ISOCONTOURS FOR DIFFERENT SWIRL ANGLES (TEMPERATURE MEASURED IN DEGREES KELVIN).

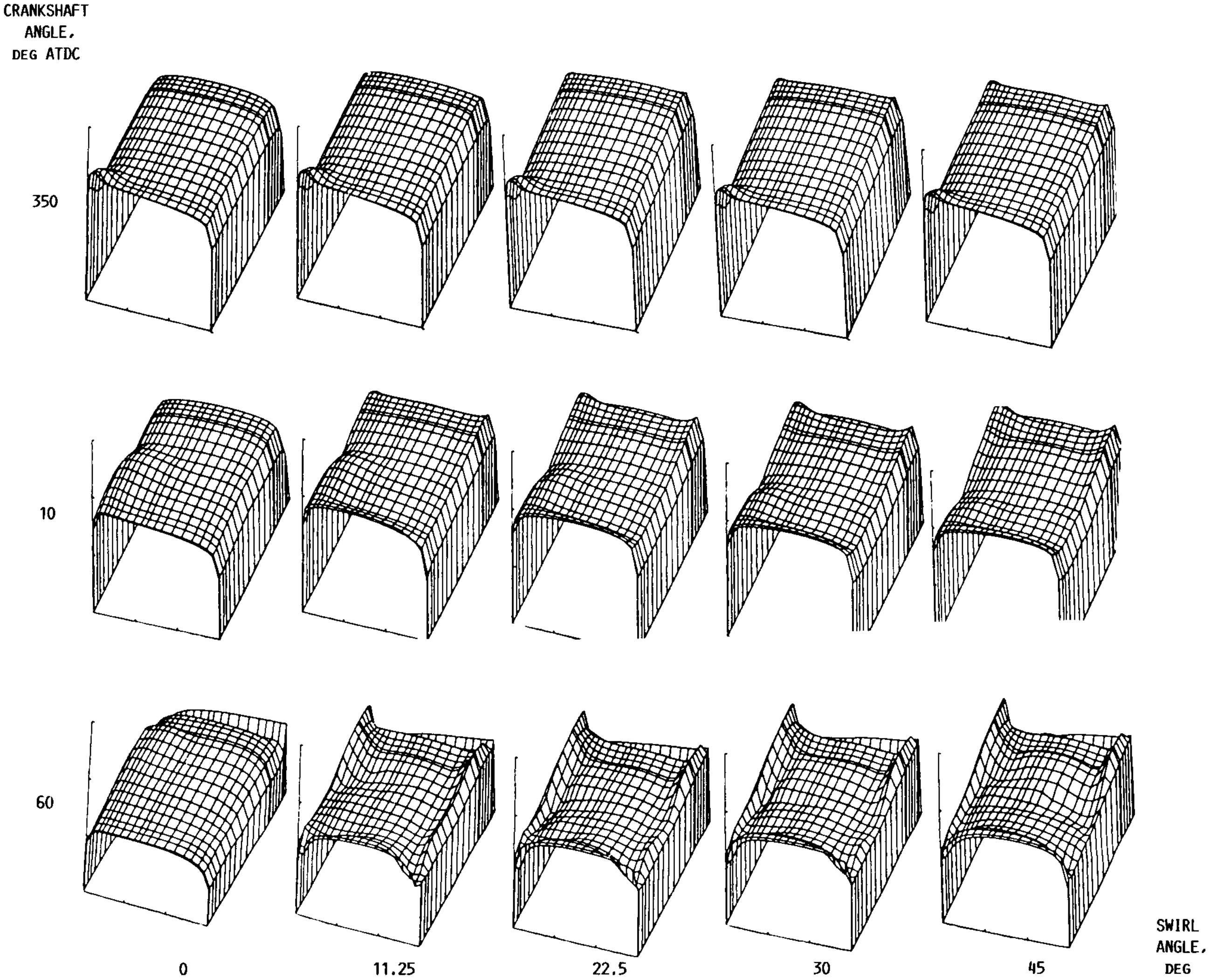

FIGURE 24. - NATURAL LOGARITHM OF TURBULENCE KINETIC ENERGY PROFILES FOR DIFFERENT SWIRL ANGLES.

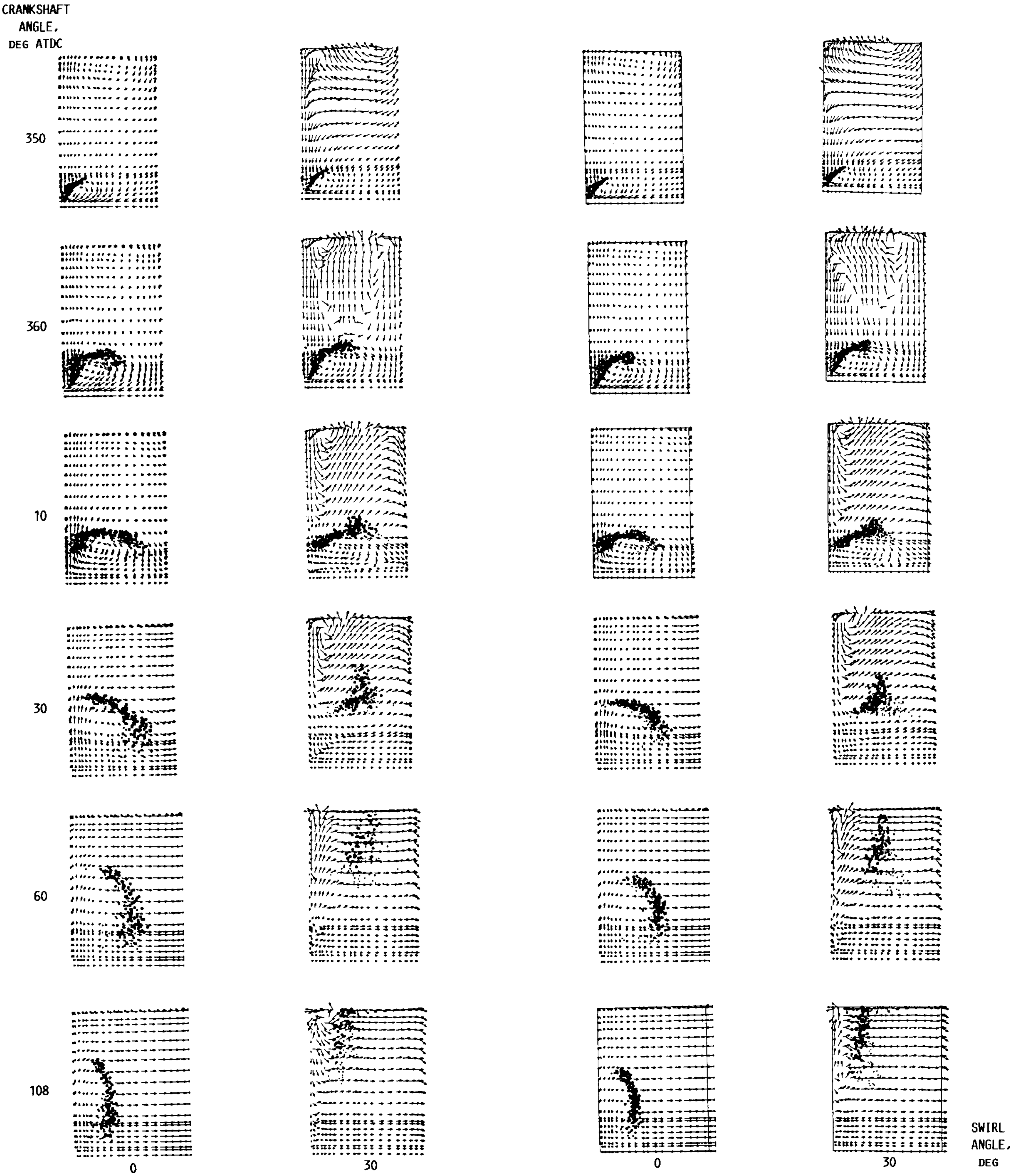

(A) ENGINE SPEED, 1500 RPM.

(B) ENGINE SPEED, 2000 RPM.

FIGURE 25. - GAS-PHASE VELOCITY VECTORS AND DROPLET LOCATIONS AT 1500 AND 2000 RPM FOR SWIRL ANGLES OF 0^0 AND 30^0.

ORIGINAL PAGE IS
OF POOR QUALITY

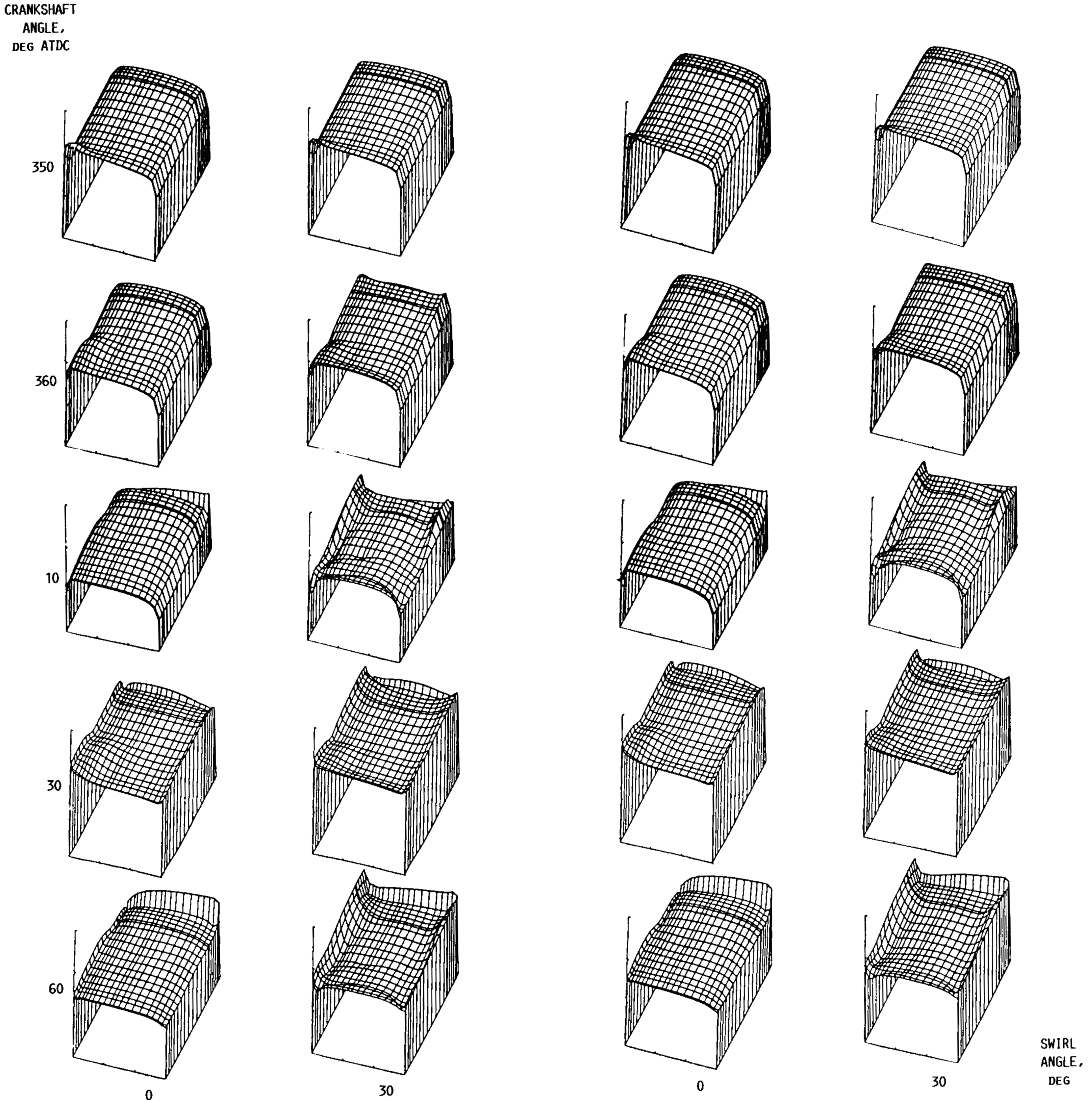

(A) ENGINE SPEED, 1500 RPM.

(B) ENGINE SPEED, 2000 RPM.

FIGURE 26. - NATURAL LOGARITHM OF TURBULENCE KINETIC ENERGY PROFILES AT 1500 AND 2000 RPM FOR SWIRL ANGLES OF 0° AND 30°.

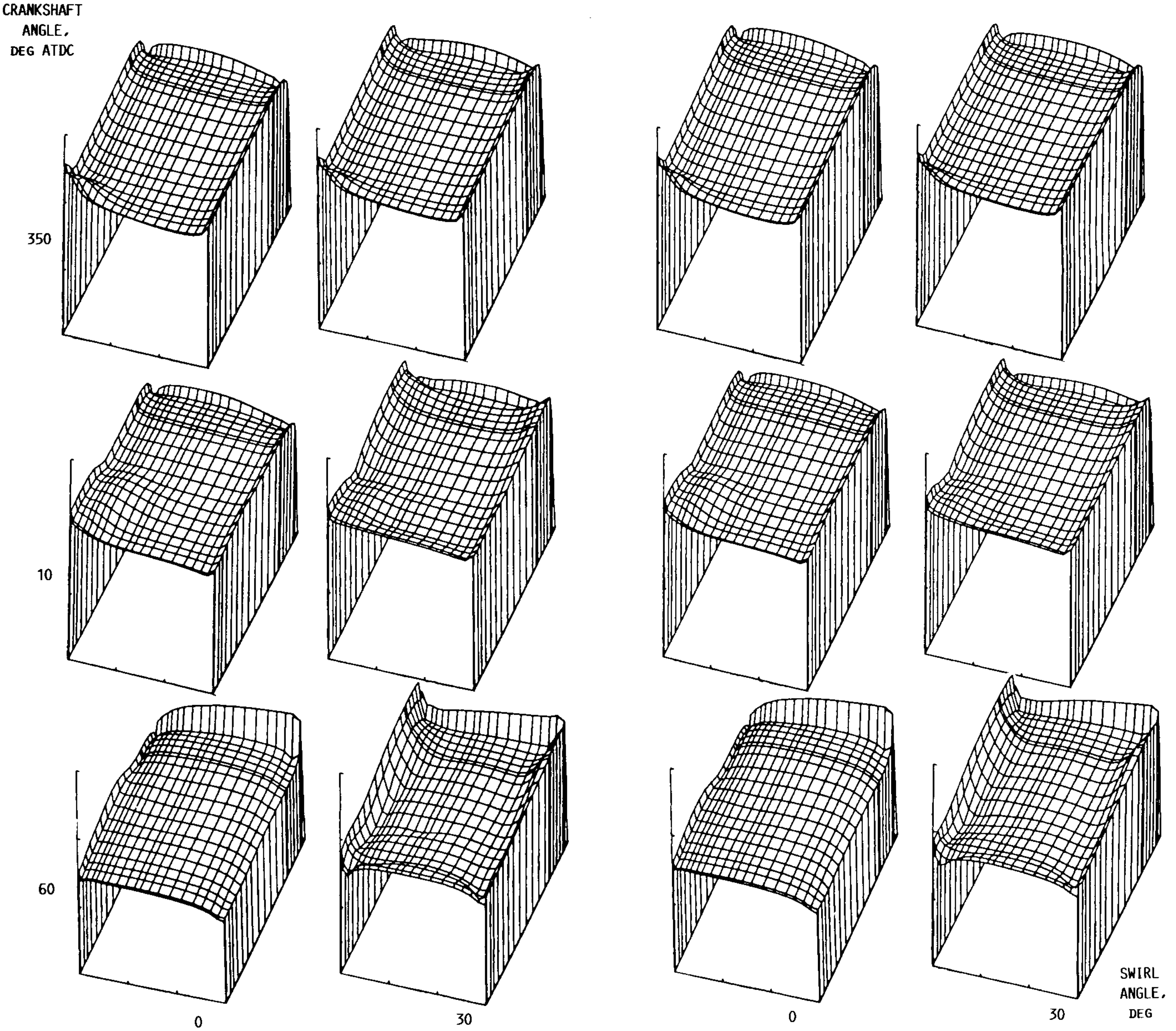

(A) ENGINE SPEED, 1500 RPM.

(B) ENGINE SPEED, 2000 RPM.

FIGURE 27. - NATURAL LOGARITHM OF DISSIPATION RATE OF TURBULENCE KINETIC ENERGY AT 1500 AND 2000 RPM FOR SWIRL ANGLES OF 0^0 AND 30^0.

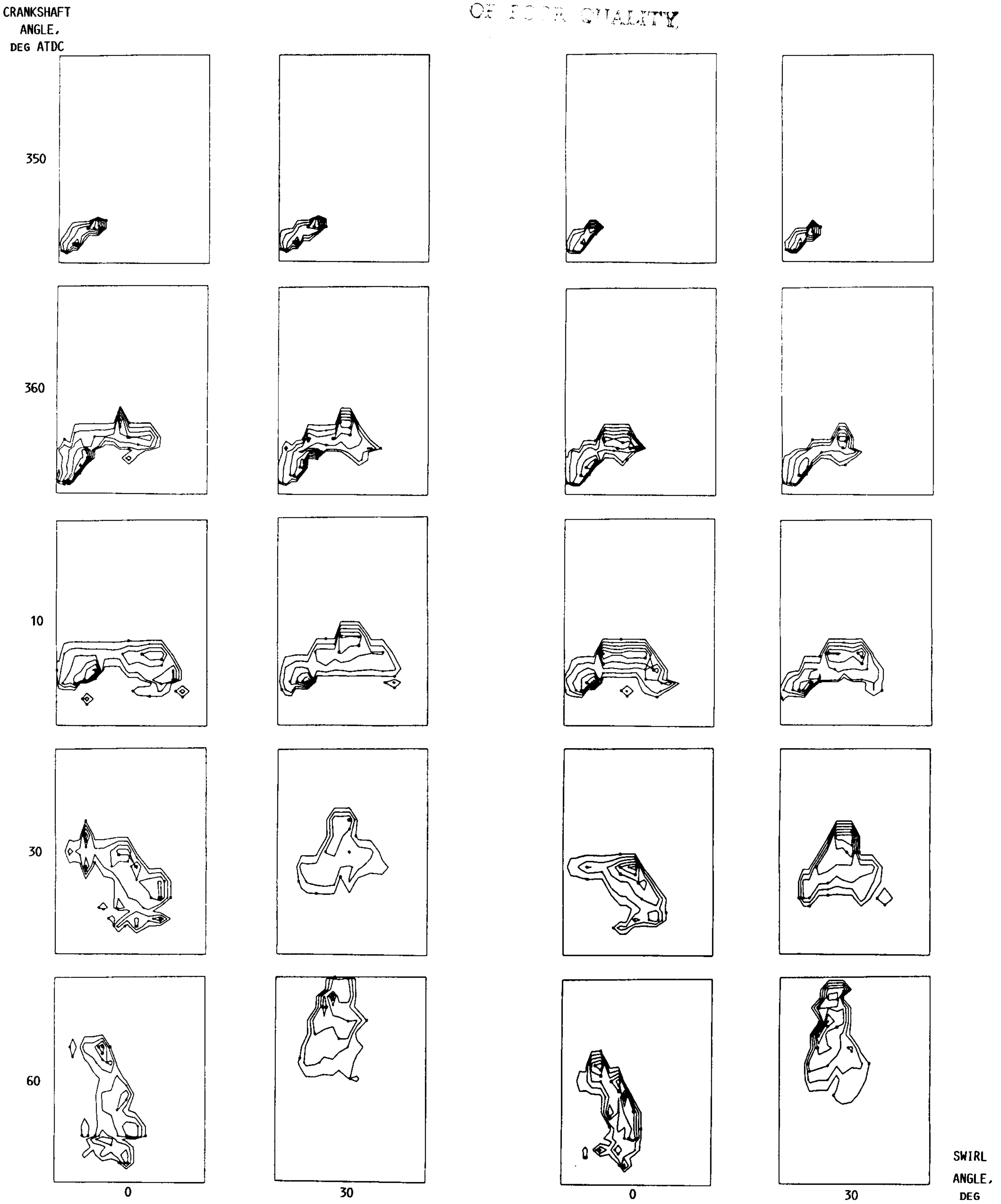

(A) ENGINE SPEED, 1500 RPM.

(B) ENGINE SPEED, 2000 RPM.

FIGURE 28. - SAUTER MEAN DIAMETER DISTRIBUTIONS AT 1500 AND 2000 RPM FOR SWIRL ANGLES OF 0° AND 30°.

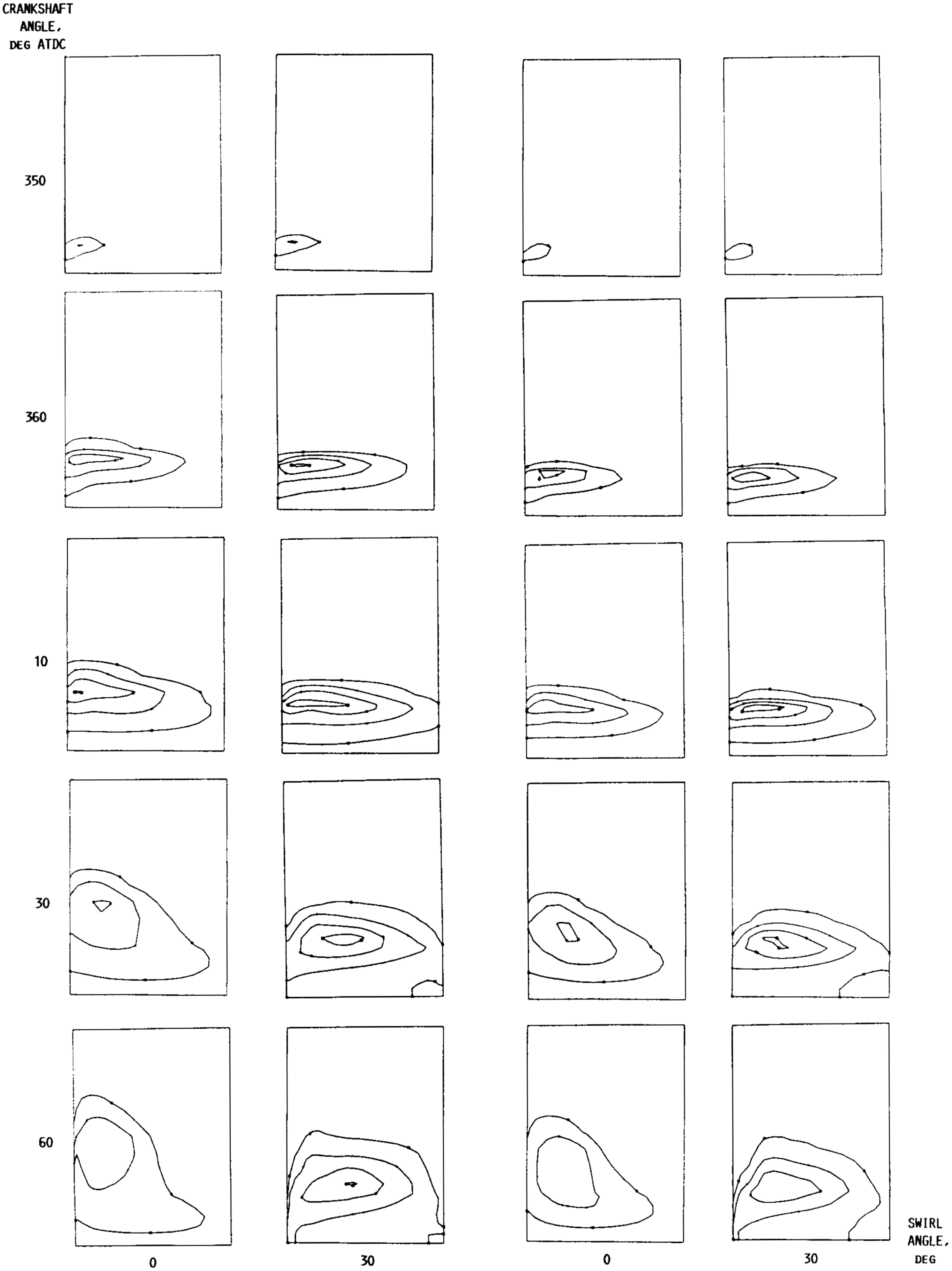

(A) ENGINE SPEED, 1500 RPM.

(B) ENGINE SPEED, 2000 RPM.

FIGURE 29. - FUEL VAPOR DISTRIBUTIONS AT 1500 AND 2000 RPM FOR SWIRL ANGLES OF 0° AND 30°.

ORIGINAL PAGE IS OF POOR QUALITY

ORIGINAL PAGE IS
OF POOR QUALITY

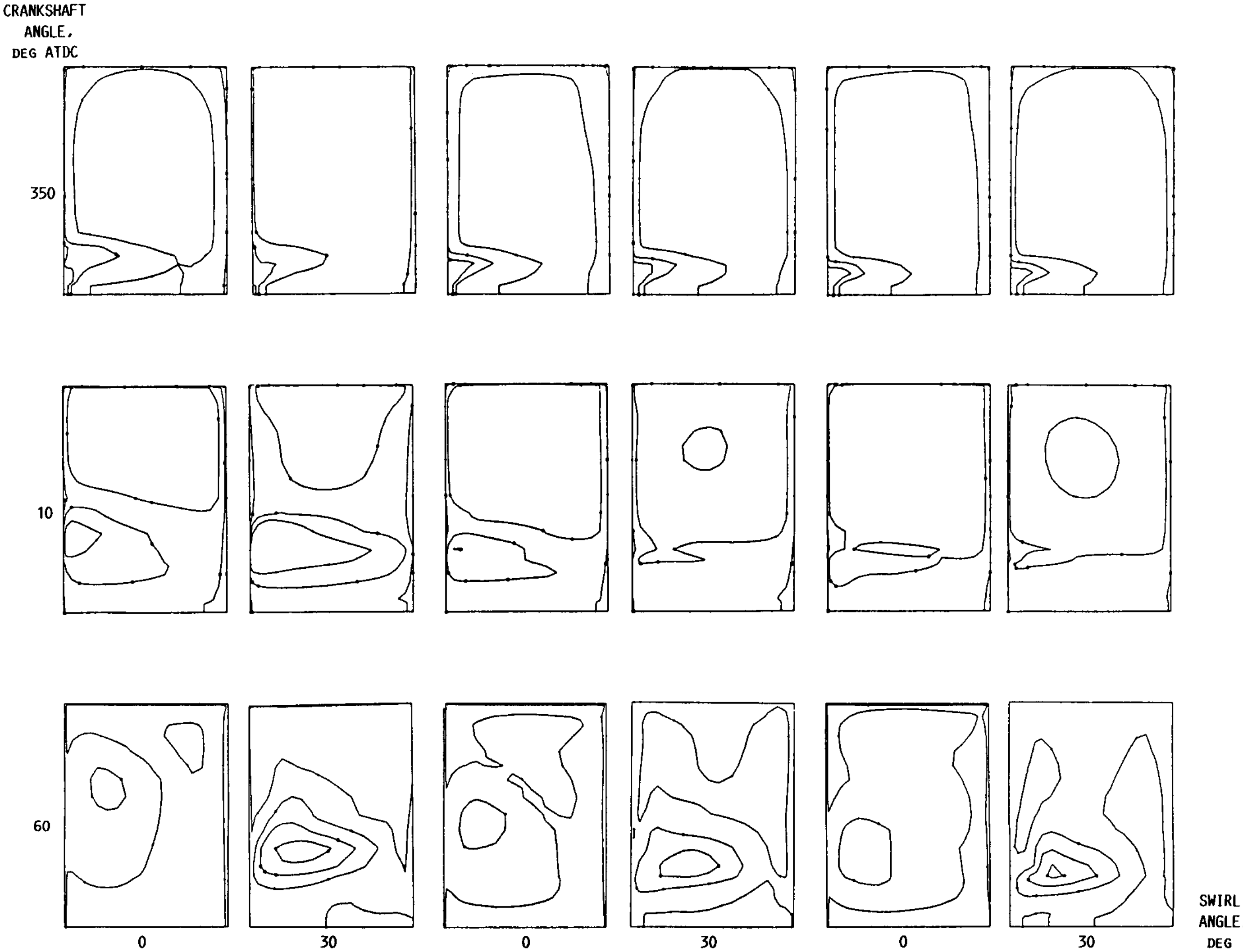

(A) ENGINE SPEED, 1000 RPM. (B) ENGINE SPEED, 1500 RPM. (C) ENGINE SPEED, 2000 RPM.

FIGURE 30. - TEMPERATURE DISTRIBUTIONS AT 1000, 1500, AND 2000 RPM FOR SWIRL ANGLES OF 0° AND 30°.

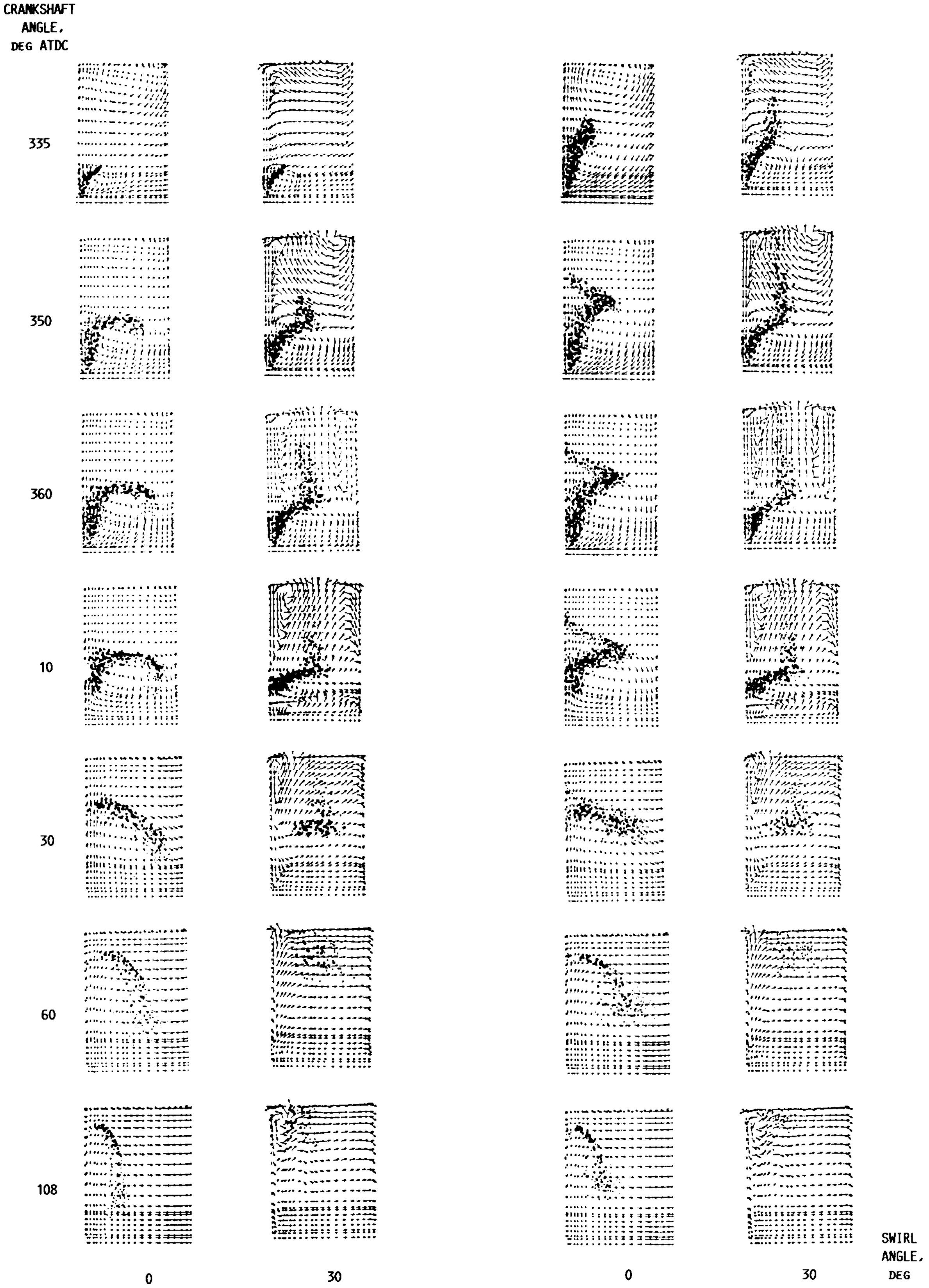

(A) INJECTION ANGLE, 30° BTDC.

(B) INJECTION ANGLE, 45° BTDC.

FIGURE 31. - GAS-PHASE VELOCITY VECTORS AND DROPLET LOCATIONS FOR INJECTION ANGLES OF 30° AND 45° BTDC, WITH SWIRL ANGLES OF 0° AND 30°.

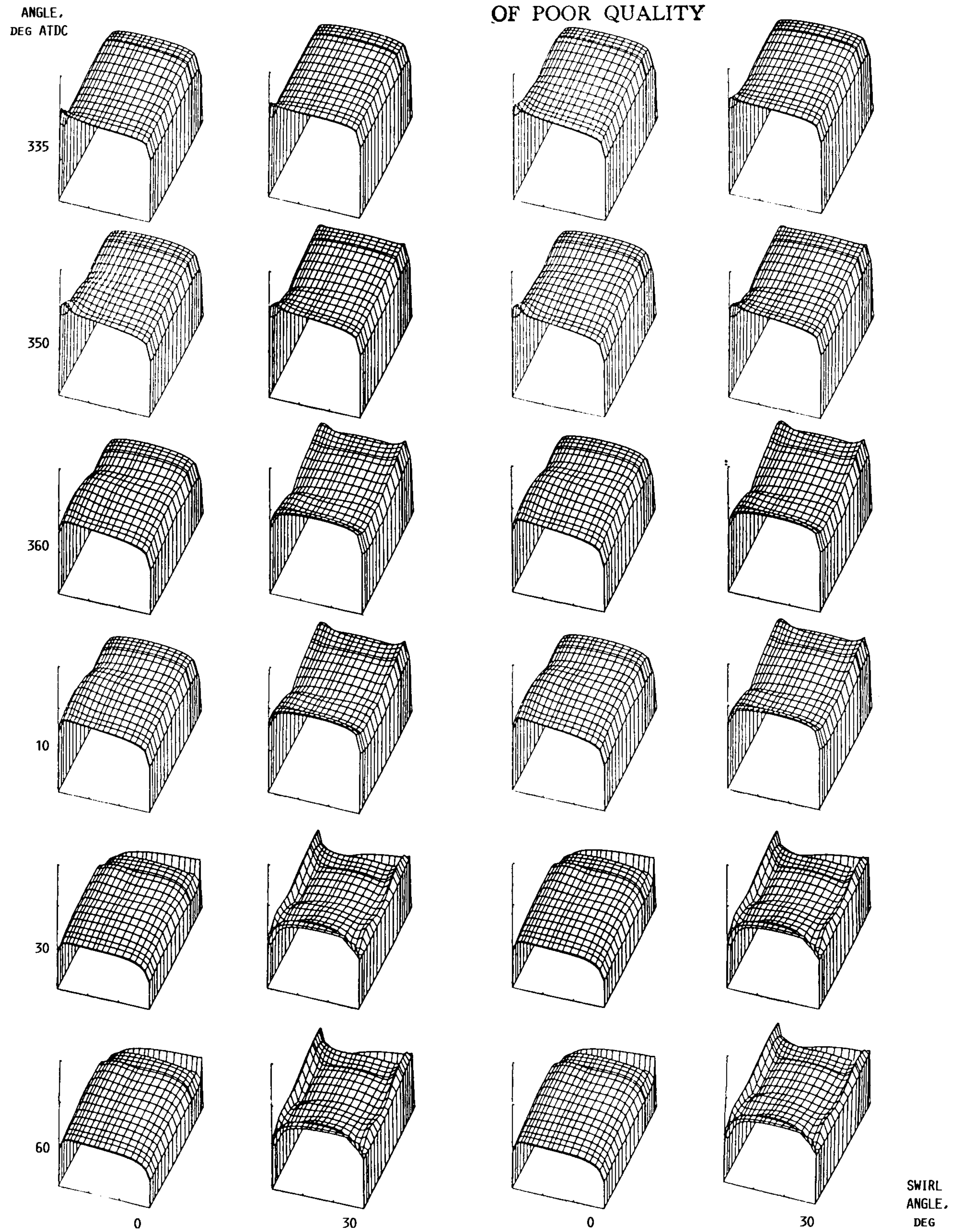

(A) INJECTION ANGLE, 30° BTDC.

(B) INJECTION ANGLE, 45° BTDC.

FIGURE 32. - NATURAL LOGARITHM OF TURBULENCE KINETIC ENERGY PROFILES FOR INJECTION ANGLES OF 30° AND 45° BTDC, WITH SWIRL ANGLES OF 0° AND 30°.

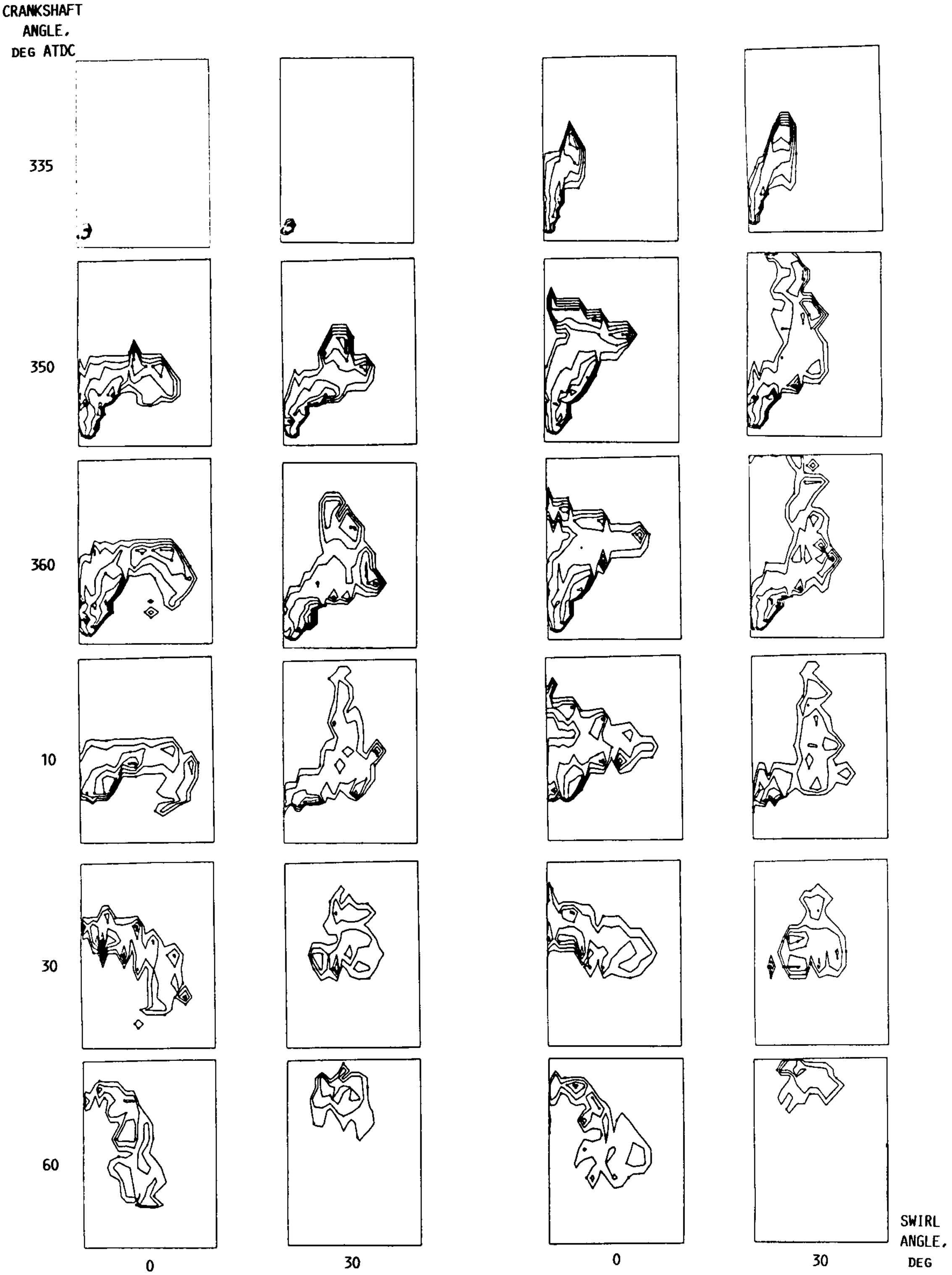

(A) INJECTION ANGLE, 30° BTDC.

(B) INJECTION ANGLE, 45° BTDC.

FIGURE 33. - SAUTER MEAN DIAMETER DISTRIBUTIONS FOR INJECTION ANGLES OF 30° AND 45° BTDC, WITH SWIRL ANGLES OF 0° AND 30°.

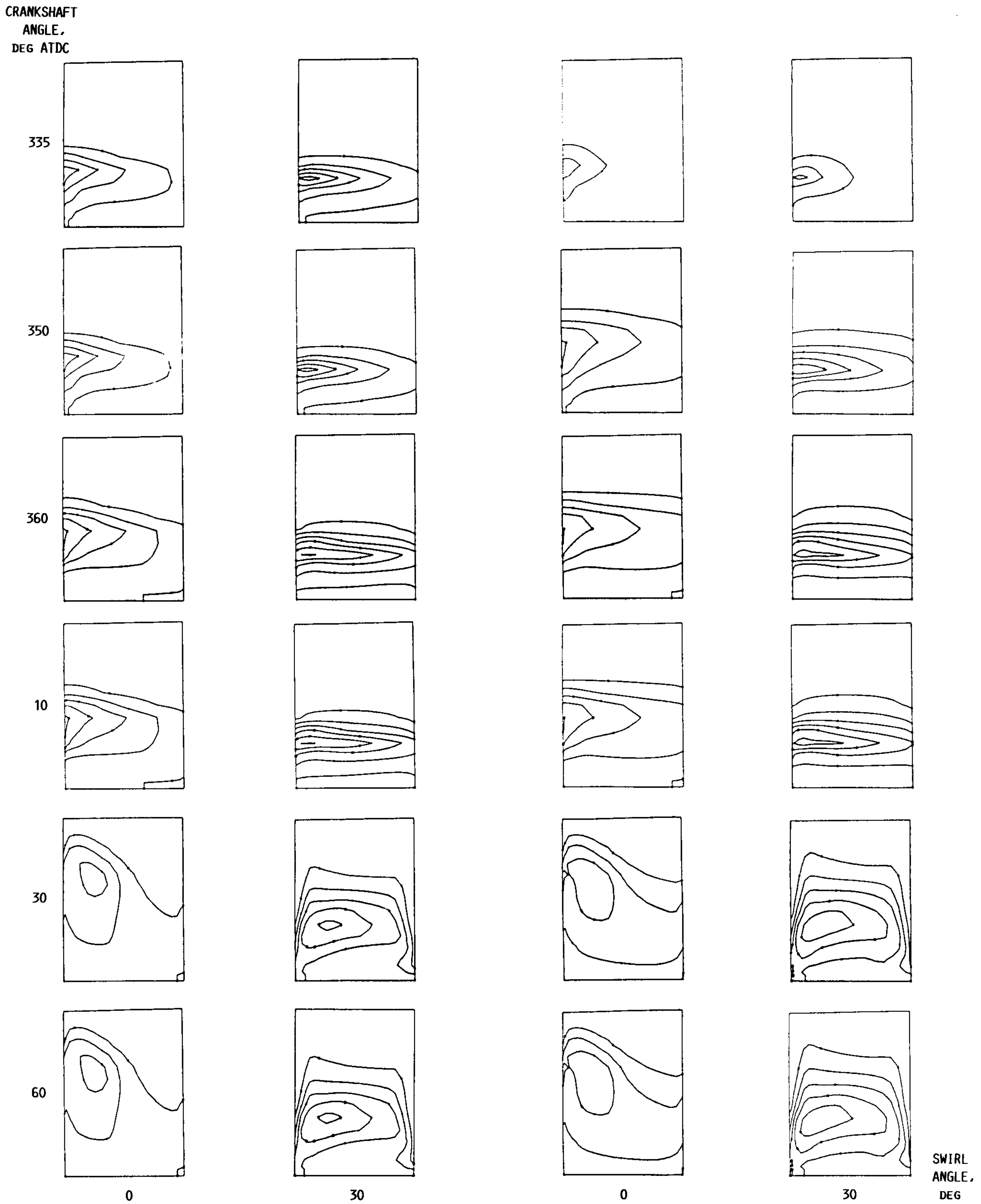

(A) INJECTION ANGLE, 30° BTDC.

(B) INJECTION ANGLE, 45° BTDC.

FIGURE 34. - FUEL VAPOR DISTRIBUTIONS FOR INJECTION ANGLES OF 30° AND 45° BTDC, WITH SWIRL ANGLES OF 0° AND 30°.

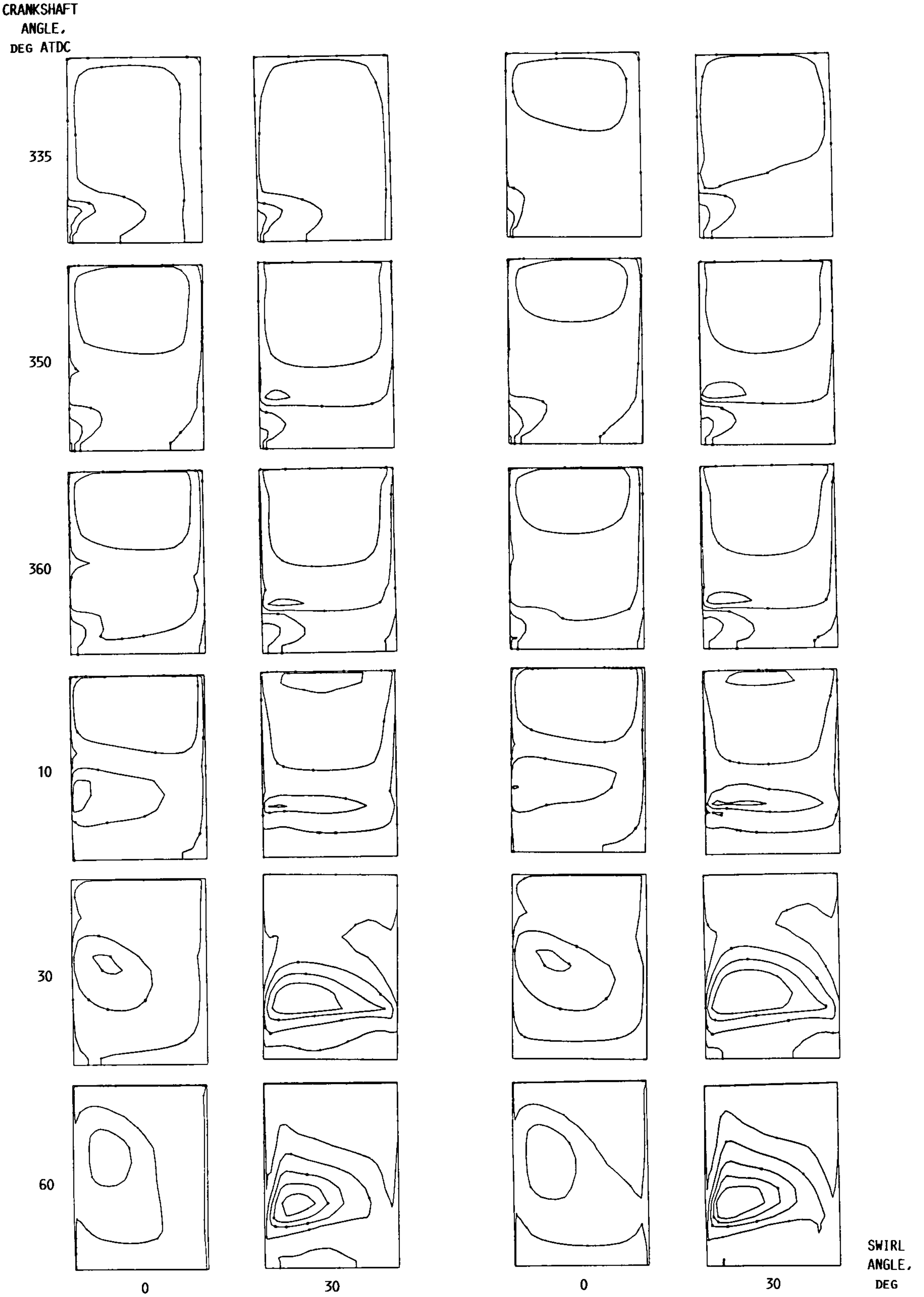

(A) INJECTION ANGLE, 30° BTDC.

(B) INJECTION ANGLE, 45° BTDC.

FIGURE 35. - TEMPERATURE DISTRIBUTIONS FOR INJECTION ANGLES OF 30° AND 45° BTDC, WITH SWIRL ANGLES OF 0° AND 30°.

ORIGINAL PAGE IS
OF POOR QUALITY

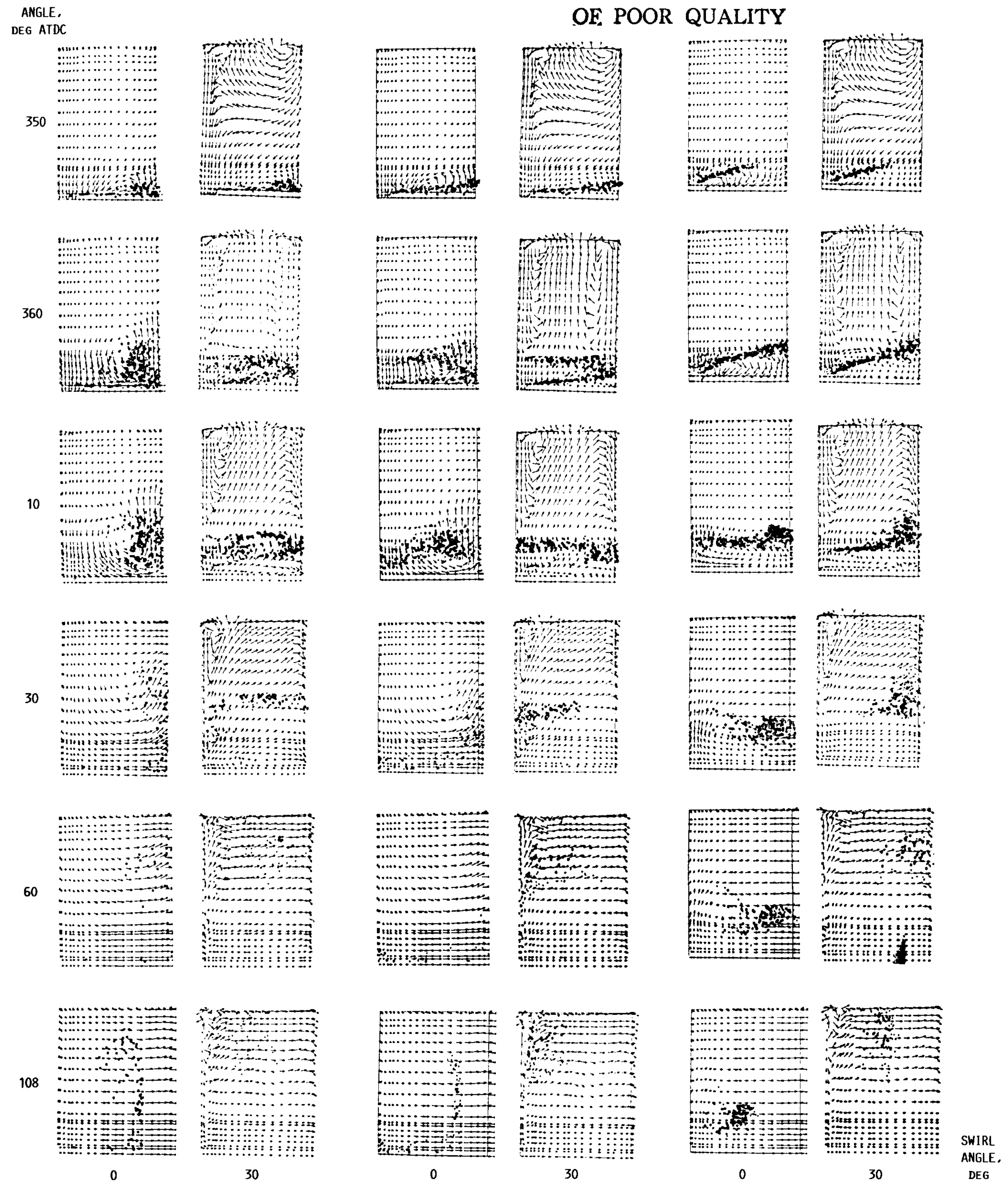

(A) SPRAY CONE ANGLE, 20°. (B) SPRAY CONE ANGLE, 60°. (C) SPRAY CONE ANGLE, 120°.

FIGURE 36. - GAS-PHASE VELOCITY VECTORS AND DROPLET LOCATIONS FOR SPRAY CONE ANGLES OF 20°, 60°, AND 120°, WITH SWIRL ANGLES OF 0° AND 30°.

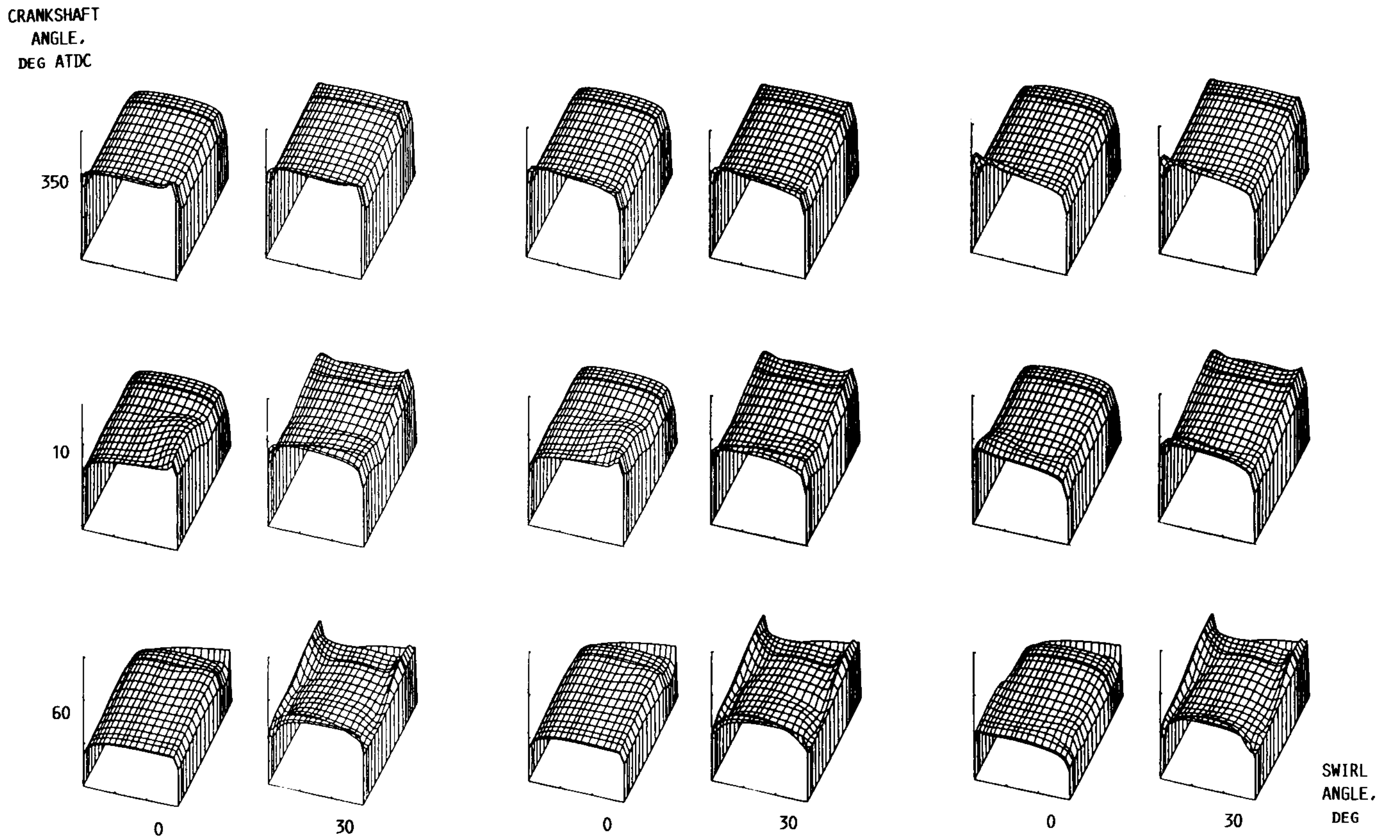

(A) SPRAY CONE ANGLE, 20^{0}.

(B) SPRAY CONE ANGLE, 60^{0}.

(C) SPRAY CONE ANGLE, 120^{0}.

FIGURE 37. - NATURAL LOGARITHM OF TURBULENCE KINETIC ENERGY PROFILES FOR SPRAY CONE ANGLES OF 20^{0}, 60^{0}, AND 120^{0}, WITH SWIRL ANGLES OF 0^{0} AND 30^{0}.

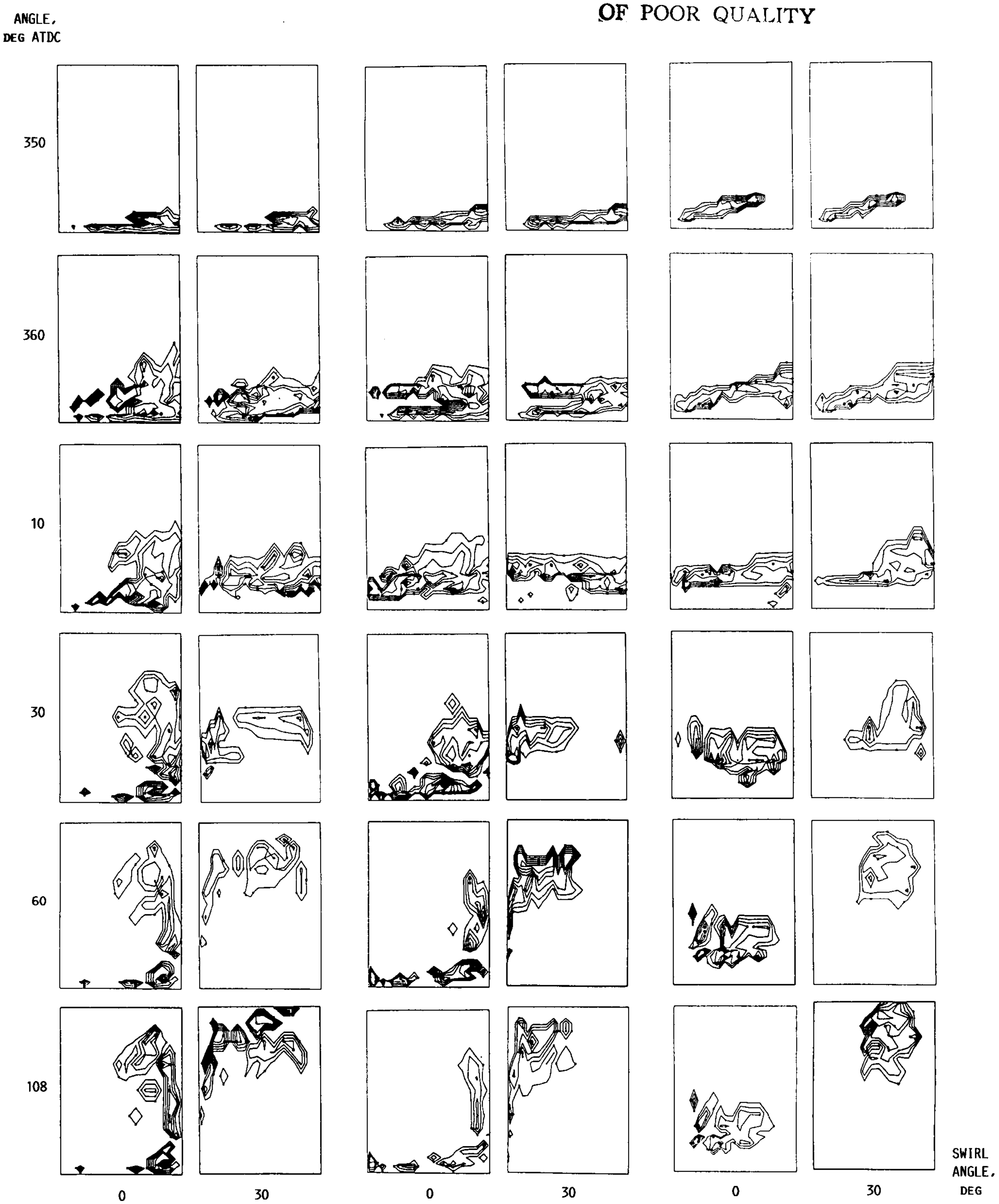

(A) SPRAY CONE ANGLE, 20°.

(B) SPRAY CONE ANGLE, 60°.

(C) SPRAY CONE ANGLE, 120°.

FIGURE 38. - SAUTER MEAN DIAMETER DISTRIBUTIONS FOR SPRAY CONE ANGLES OF 20°, 60°, AND 120°, WITH SWIRL ANGLES OF 0° AND 30°.

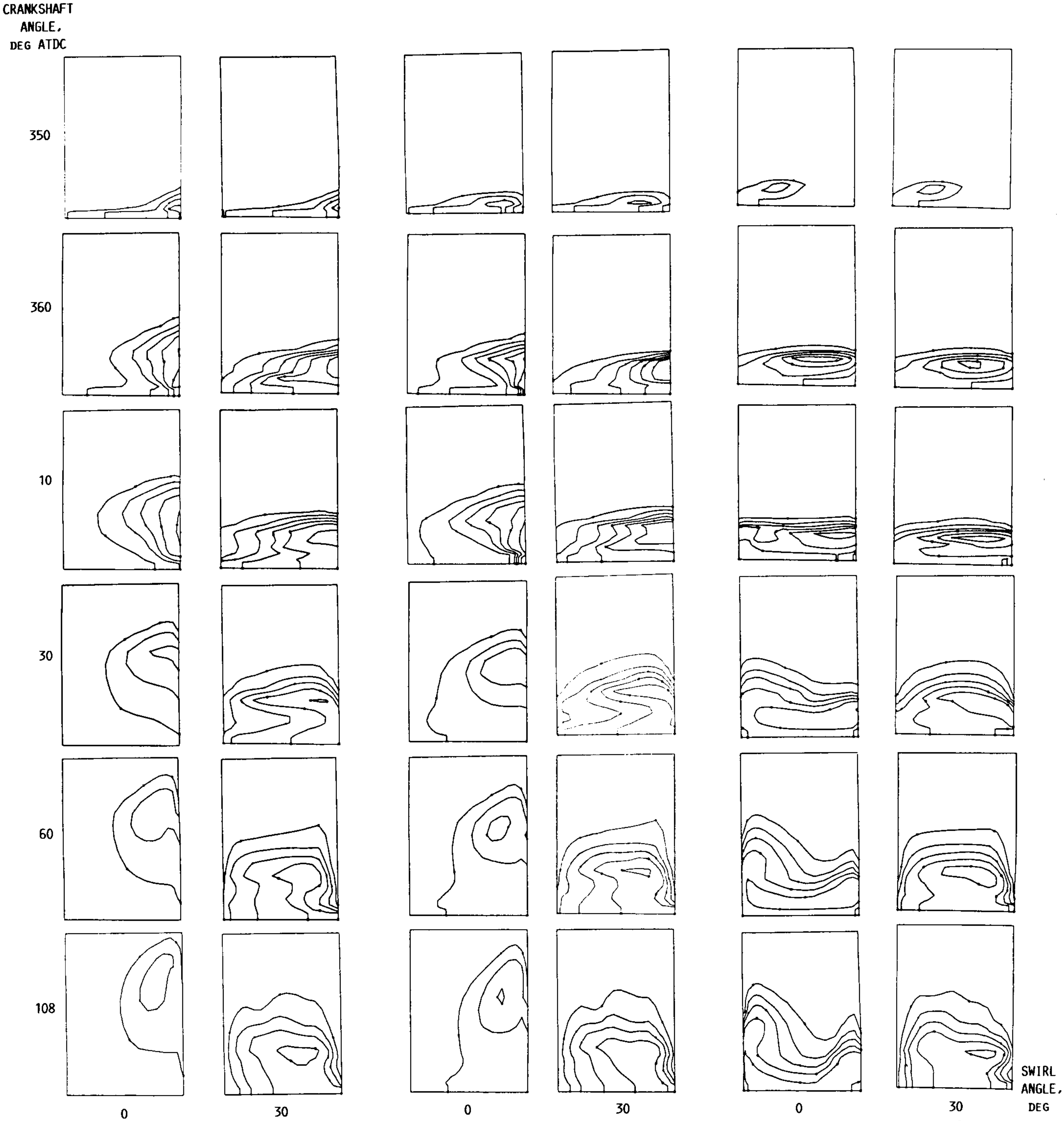

(A) SPRAY CONE ANGLE, 20°. (B) SPRAY CONE ANGLE, 60°. (C) SPRAY CONE ANGLE, 120°.

FIGURE 39. - FUEL VAPOR DISTRIBUTIONS FOR SPRAY CONE ANGLES OF 20°, 60°, AND 120°, WITH SWIRL ANGLES OF 0° AND 30°.

ORIGINAL PAGE IS
OF POOR QUALITY

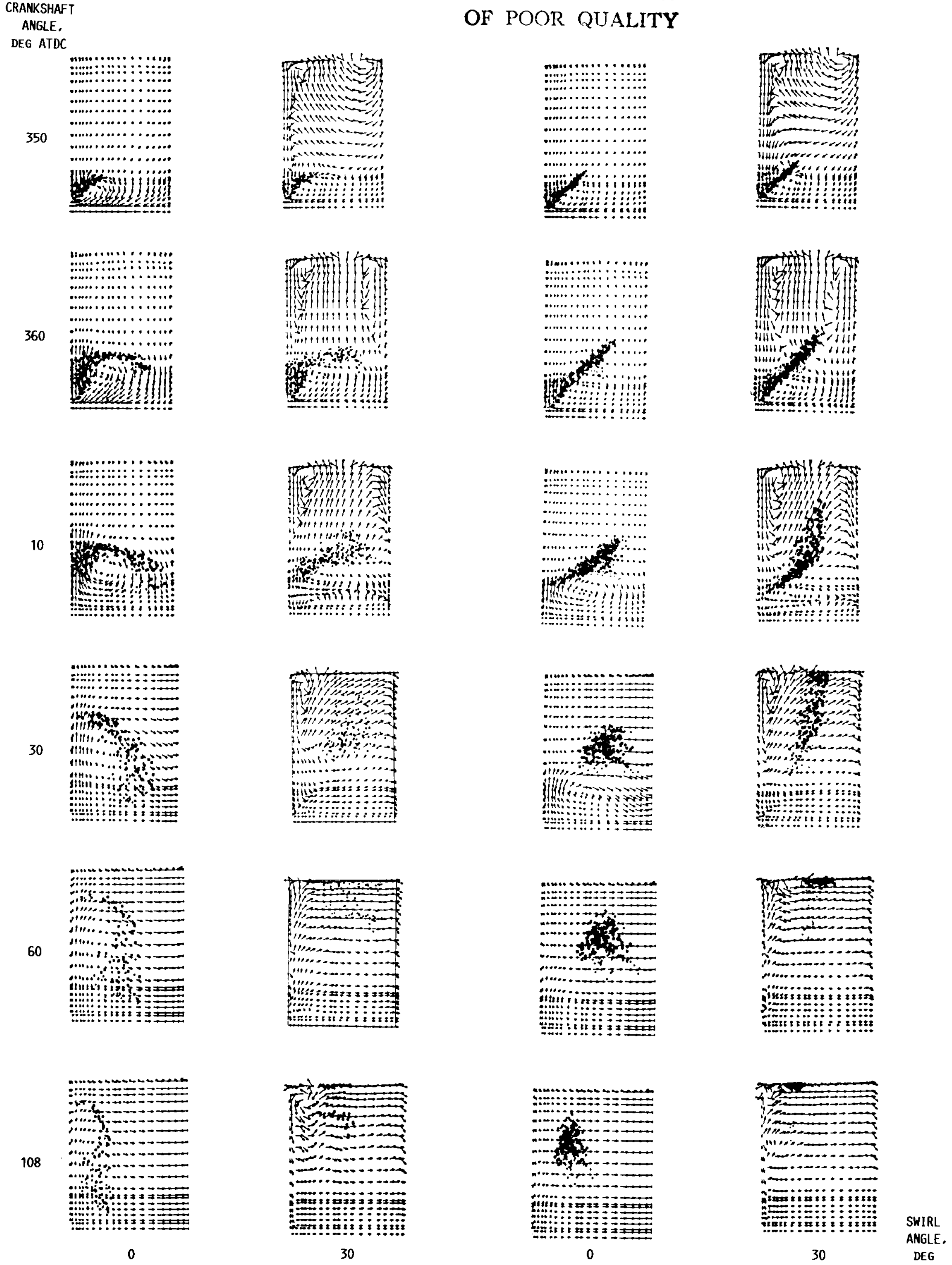

(A) PEAK OF DISTRIBUTION FUNCTION d_{peak}, 30.8 μM AND MAXIMUM DROPLET DIAMETER d_{max}, 50 μM.

(B) PEAK OF DISTRIBUTION FUNCTION d_{peak}, 60 μM AND MAXIMUM DROPLET DIAMETER d_{max}, 100 μM.

FIGURE 40. - GAS-PHASE VELOCITY VECTORS AND DROPLET LOCATIONS FOR THE TWO DROPLET DISTRIBUTION FUNCTIONS SHOWN IN TABLE II, WITH SWIRL ANGLES OF 0° AND 30°.

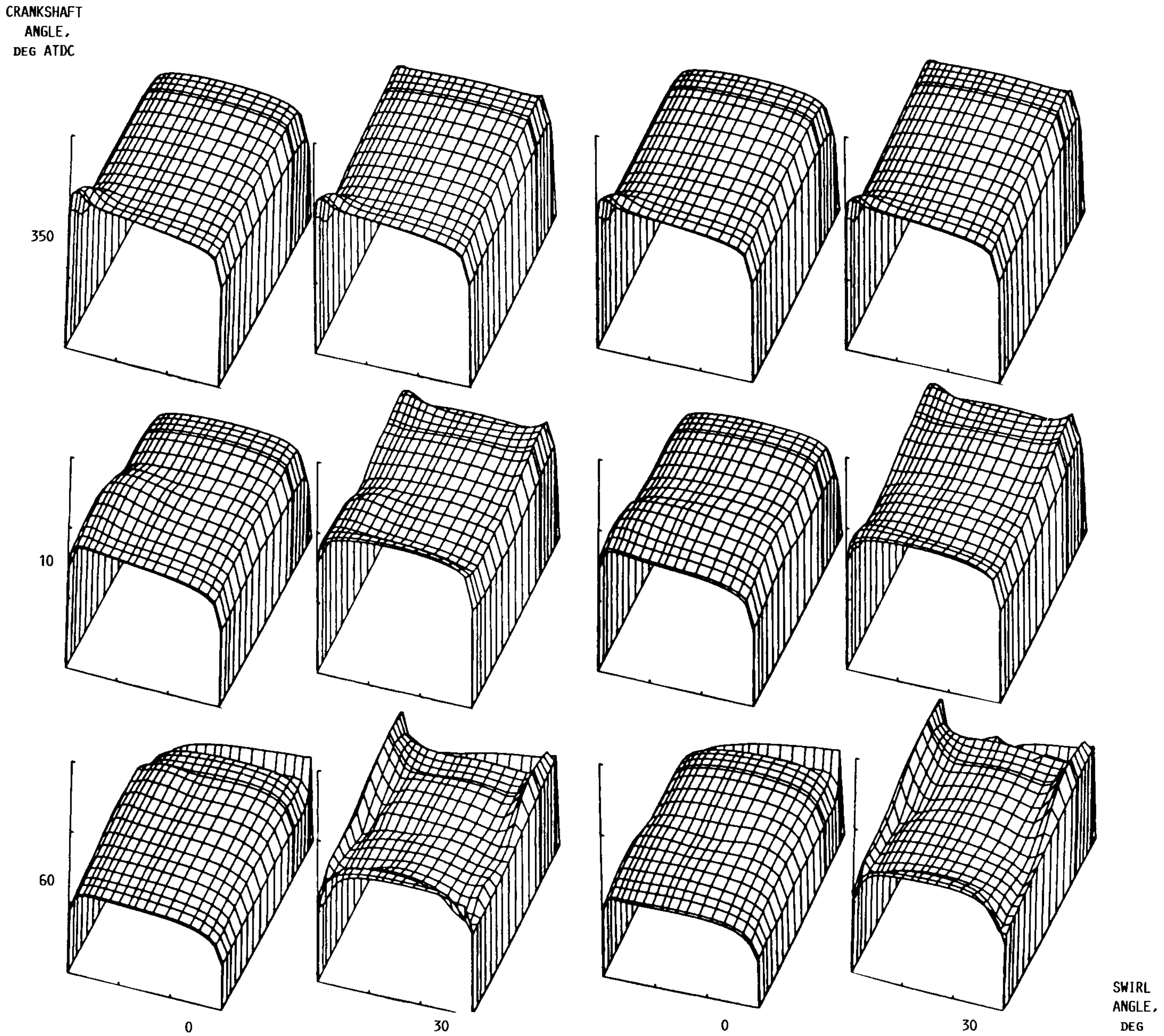

(A) PEAK OF DISTRIBUTION FUNCTION d_{peak}, 30.8 μm AND MAXIMUM DROPLET DIAMETER d_{max}, 50 μm.

(B) PEAK OF DISTRIBUTION FUNCTION d_{peak}, 60 μm AND MAXIMUM DROPLET DIAMETER d_{max}, 100 μm.

FIGURE 41. - NATURAL LOGARITHM OF TURBULENCE KINETIC ENERGY PROFILES FOR THE TWO DROPLET DISTRIBUTION FUNCTIONS SHOWN IN TABLE II, WITH SWIRL ANGLES OF 0° AND 30°.

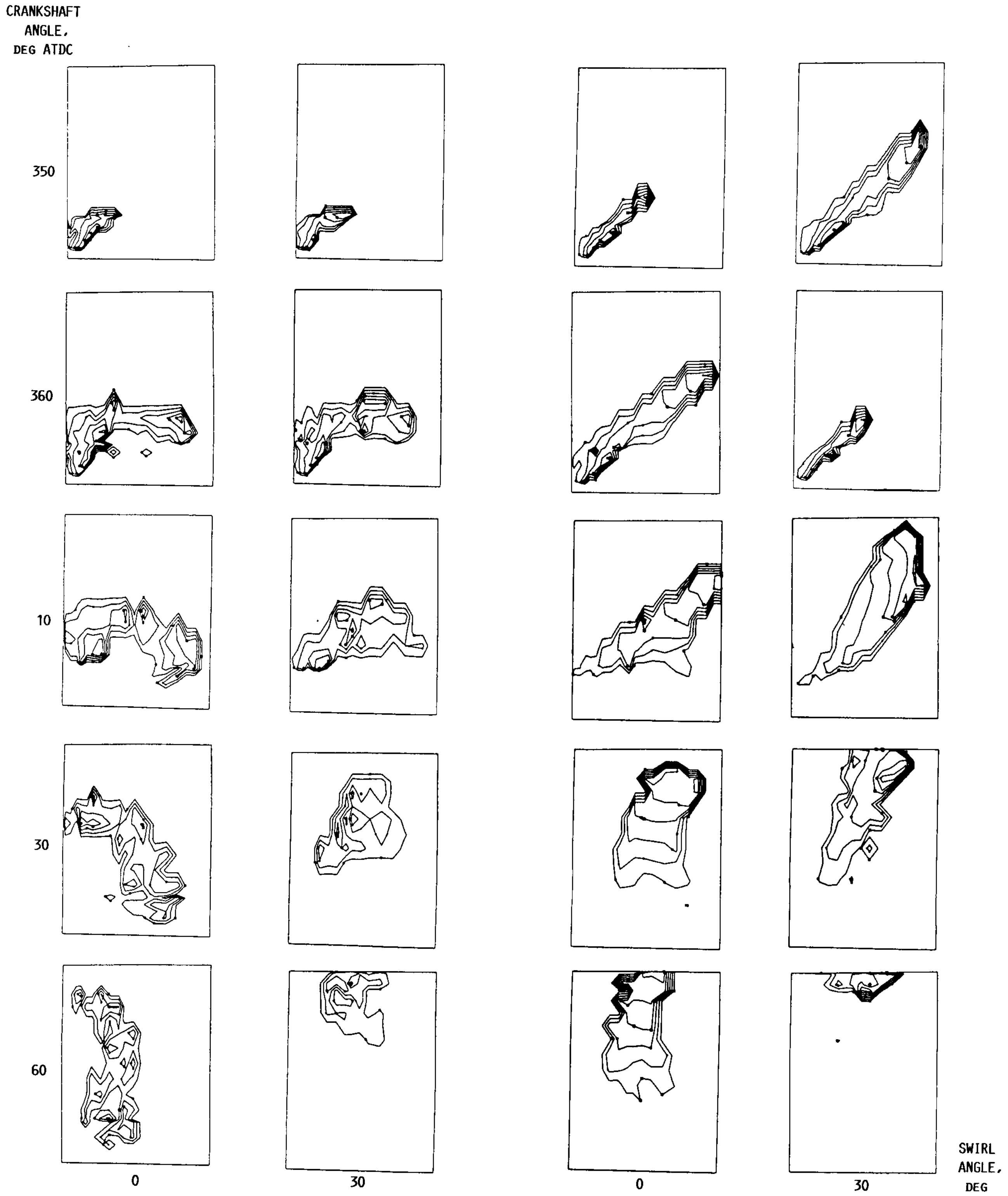

(A) PEAK OF DISTRIBUTION FUNCTION d_{peak}, 30.8 μM AND MAXIMUM DROPLET DIAMETER d_{max}, 50 μM.

(B) PEAK OF DISTRIBUTION FUNCTION d_{peak}, 60 μM AND MAXIMUM DROPLET DIAMETER d_{max}, 100 μM.

FIGURE 42. - SAUTER MEAN DIAMETER DISTRIBUTIONS FOR THE TWO DROPLET DISTRIBUTION FUNCTIONS SHOWN IN TABLE II, WITH SWIRL ANGLES OF 0^o AND 30^o.

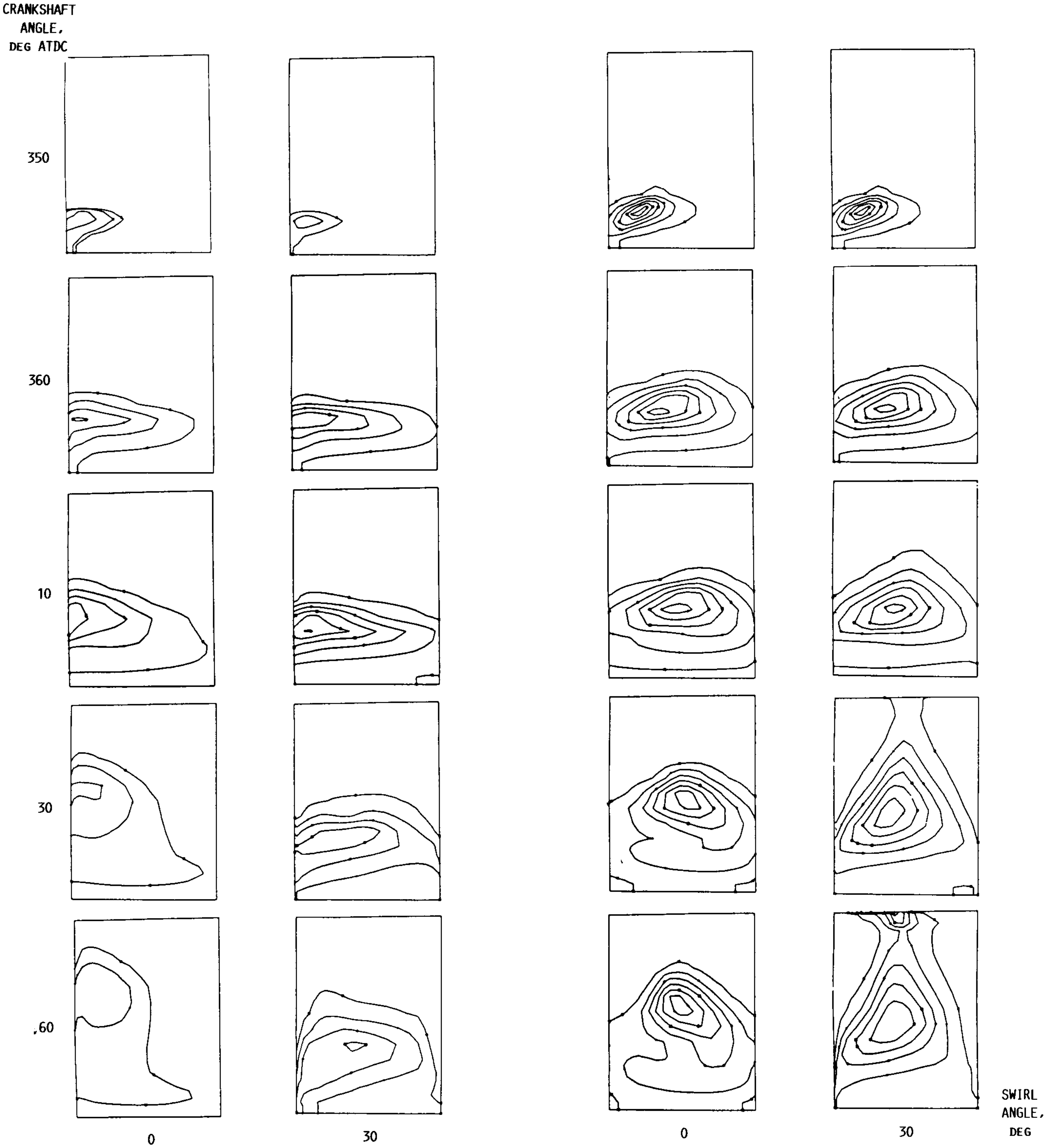

(A) PEAK OF DISTRIBUTION FUNCTION d_{peak}, 30.8 μM AND MAXIMUM DROPLET DIAMETER d_{max}, 50 μM.

(B) PEAK OF DISTRIBUTION FUNCTION d_{peak}, 60 μM AND MAXIMUM DROPLET DIAMETER d_{max}, 100 μM.

FIGURE 43. - FUEL VAPOR DISTRIBUTIONS FOR THE TWO DROPLET DISTRIBUTION FUNCTIONS SHOWN IN TABLE II, WITH SWIRL ANGLES OF 0° AND 30°.

NASA
National Aeronautics and
Space Administration

Report Documentation Page

1. Report No. NASA TM-100135	2. Government Accession No.	3. Recipient's Catalog No.
4. Title and Subtitle Liquid Sprays and Flow Studies in the Direct-Injection Diesel Engine Under Motored Conditions		5. Report Date March 1988
		6. Performing Organization Code
7. Author(s) Hung Lee Nguyen, Mark H. Carpenter, Juan I. Ramos, Harold J. Schock, and James D. Stegeman		8. Performing Organization Report No. E-3685
		10. Work Unit No. 505-62-11
9. Performing Organization Name and Address National Aeronautics and Space Administration Lewis Research Center Cleveland, Ohio 44135-3191		11. Contract or Grant No.
		13. Type of Report and Period Covered Technical Memorandum
12. Sponsoring Agency Name and Address National Aeronautics and Space Administration Washington, D.C. 20546-0001		14. Sponsoring Agency Code

15. Supplementary Notes

Hung Lee Nguyen, Harold J. Schock, and James D. Stegeman, NASA Lewis Research Center; Mark H. Carpenter, NASA Langley Research Center, Hampton, Virginia 23665-5225; Juan I. Ramos, Carnegie-Mellon University, Pittsburgh, Pennsylvania 15213.

16. Abstract

A two-dimensional, implicit finite-difference method of the control-volume variety, a two-equation model of turbulence, and a discrete droplet model have been used to study the flow field, turbulence levels, fuel penetration, vaporization, and mixing in diesel engine environments. The model has also been used to study the effects of engine speed, injection angle, spray cone angle, droplet distribution, and intake swirl angle on the flow field, spray penetration and vaporization, and turbulence in motored two-stroke diesel engines. It is shown that there are optimum conditions for injection, which depend on droplet distribution, swirl, spray cone angle, and injection angle. The optimum conditions result in good spray penetration and vaporization and in good fuel mixing. The calculation presented in this report clearly indicates that internal combustion engine models can be used to assess, at least qualitatively, the effects of injection characteristics and engine operating conditions on the flow field and on the spray penetration and vaporization in diesel engines.

17. Key Words (Suggested by Author(s)) Liquid fuel injection Direct-injection diesel engines	18. Distribution Statement Unclassified - Unlimited Subject Category 07

19. Security Classif. (of this report) Unclassified	20. Security Classif. (of this page) Unclassified	21. No of pages 80	22. Price* A05

NASA FORM 1626 OCT 86

*For sale by the National Technical Information Service, Springfield, Virginia 22161